Numerical Investigation of Ultrasound-Triggered Microbubble Contrast Agent Dynamics

Hossein (Sohrab) Yusefi

A Thesis

In the Department

of

Physics

Presented in Partial Fulfillment of the Requirements

for the Degree of Doctor of Philosophy at

Concordia University

Montréal, Québec, Canada

August-2024

CONCORDIA UNIVERSITY

School of Graduate Studies

This is to certify that the thesis prepared

By: Hossein (Sohrab) Yusefi

Entitled: Numerical Investigation of Ultrasound-Triggered Microbubble Contrast Agent Dynamics

and submitted in partial fulfillment of the requirements for the degree of

Doctor of Philosophy (Physics)

complies with the regulations of the University and meets the accepted standards with respect to originality and quality.

Signed by the final examining committee:

_____ Chair
Dr. Steve Shih

_____ External Examiner
Dr. Michael C. Kolios

_____ Arm's Length Examiner
Dr. Christophe Grova

_____ Examiner
Dr. Claudine Gauthier

_____ Examiner
Dr. Hassan Rivaz

_____ Supervisor
Dr. Brandon Helfield

Approved by _____
Dr. Pablo Bianucci, Graduate Program Director

date _____
Dr. Pascale Sicotte, Dean, Faculty of Arts and Science

ABSTRACT

Numerical Investigation of Ultrasound-Triggered Microbubble Contrast Agent Dynamics

Hossein (Sohrab) Yusefi, Ph. D.

Concordia University, 2024

Biomedical ultrasound is widely employed as an imaging modality for anatomical assessment and to provide information on blood flow characteristics. There is increasing interest in employing microbubble contrast agents for diagnostic and therapeutic ultrasound. Unlike MR and CT agents, ultrasound contrast agents are comparable in size to a red blood cell, providing a purely intravascular agent for clinical radiology. Microbubbles are currently clinically employed in echocardiography and liver applications, as well as pre-clinically, for the tumors' characterization and quantifying perfusion. Critical to the effectiveness of contrast agent microbubbles is an understanding of their nonlinear vibrations and scattering within the vasculature, specifically within the microvasculature where standard ultrasound flow estimation suffers from slow blood velocity and low red blood cell concentration.

Using mainly a finite element computational approach, this thesis aims to investigate the nonlinear physics of ultrasound-stimulated microbubbles within small capillaries to shed some light on the vibration dynamic and behavior of microbubble contrast agents. Over three chapters of results, this thesis analyses the complex vibration dynamics of microbubbles in proximity to each other and confined in a viscoelastic vessel. The results provided in this thesis explain how the resonance behavior of a microbubble is dampened and shifted by its neighboring bubbles and how smaller bubbles show off-resonance activities corresponding to the resonance behavior of the bigger, neighboring bubbles. The results also explain how initial phospholipid packing and bubble

proximity affect subharmonic response and how a viscoelastic vessel dampens resonance behavior and amplifies off-resonance behavior.

This thesis conducts a robust study on ultrasound-stimulated microbubble-compliant vessel interactions. It will contribute to optimal contrast agent design for both imaging and therapy, image quantification, and the development of new ultrasound pulse sequences.

ACKNOWLEDGEMENTS

I would like to express my heartfelt gratitude to my supervisor, Dr. Brandon Helfield, for his constant support, his availability to discuss my project, and his efforts in creating a positive and productive lab environment.

I thank my committee members, Dr. Hassan Rivaz and Dr. Claudine Gauthier, for their valuable guidance throughout my work.

Thanks to my amazing lab mates for their support, creating a happy and positive environment in Helfield lab, and creating lasting happy memories.

I would especially like to thank my amazing wife, Mahshid, for her unwavering support and being my greatest motivation. And finally, thanks to my parents, Kian and Hourieh, for fighting to give me a quality education and a chance for a better future.

This project was enabled through funds from Concordia University Faculty of Art and Science Graduate Fellowship, the Concordia International Tuition Award of Excellence, and a research bursary from my supervisor paid from funds provided by the Natural Sciences and Engineering Research Council of Canada (NSERC).

CONTRIBUTION TO ORIGINAL KNOWLEDGE

This manuscript-based thesis contains four manuscripts as below:

Chapter 1.1, titled "Ultrasound Contrast Imaging: Fundamentals and Emerging Technology," is my first publication. In it, I explain the history and background of ultrasound contrast imaging and review current and future applications.

Chapter 2, titled: "The Influence of Inter-Bubble Spacing on The Resonance Response of Ultrasound Contrast Agent" is my second publication in which I study the effect of boundary on microbubble vibration in a system of two bubbles vibrating in close proximity of each other.

Chapter 3, titled: "Subharmonic Resonance of Phospholipid Coated Ultrasound Contrast Agent Microbubbles" is my third publication. After studying the resonance response of microbubbles in a two-bubble system scenario, we further studied their subharmonic behavior under the boundary effect. Furthermore, in this study, we studied the effect of initial phospholipid packing on the microbubbles' vibration dynamic and subharmonic response.

Chapter 4, titled: "The Effect of Micro-Vessel Viscosity on The Resonance Response of a Two-Microbubble System," is my last publication. In this work, built upon our two previous chapters, I added a viscoelastic vessel to our system. I studied the vibration dynamic of a two-bubble system in proximity to the vessel wall, studying their effect on each other.

Dr. Brandon Helfield and I wrote all four mentioned manuscripts. The original work and drafts were done by myself under the supervision and guidance of Dr.Helfield, and we both did in-depth revisions, edits, and final reviews.

Table of Contents

List of figures

List of tables

Chapter 1. Introduction

Ultrasound, by nature, is considered safe and non-ionizing. Ultrasound imaging is a real-time imaging modality that is very customizable and can be highly computerized. Thanks to recent technological advancements, it is compact, portable, and cost-effective. Due to its many advantages, ultrasound is commonly used in many medical clinics and is considered the most widely used cross-sectional medical imaging modality [1].

The most common medical ultrasound application is as an imaging modality, but it is not limited to that. It has been known for a long time that ultrasound waves can interact with tissue and produce biological effects, making medical ultrasound a promising therapeutic modality. Under specific settings and power, ultrasound waves can produce oscillating cavities and radiation force, which can change the cell environment or concentration gradient near the cell membrane, affecting the diffusion of ions. Furthermore, ultrasound energy is capable of inducing in its focal point which can effectively increases drug uptake and can be used in physiotherapy to treat bone or soft tissue injuries. Moreover, a high-intensity ultrasound wave is powerful enough to destroy cells or tissue in a small area, and it has applications in cancer therapy or the breaking of kidney stones [2].

The 1960s marked a significant milestone in the field of medical ultrasound with the discovery of tiny gaseous bubbles during echocardiography. This groundbreaking observation led to the development of the first ultrasound contrast agents. Since their introduction, the field of medical ultrasound has experienced a rapid expansion, ushering in a new era of diagnostics and applications [3,4].

Modern ultrasound contrast agents are characterized by their unique properties. These agents, which consist of microbubbles with a diameter of 1-8 μm, are typically polydisperse as a suspension. The microbubbles are coated with a biologically compatible shell, usually a phospholipid monolayer, and due to their size, they remain intervascular and function as red blood cell tracers. The viscoelastic shell and the gas core of these bubbles enable them to respond to the ultrasound field, vibrating with the wave in the form of contraction and expansion. This vibration generates a powerful ultrasound response and pressure, leading to numerous approved applications in medical ultrasound and many more potential applications in studies or clinical trials.

The microbubble-ultrasound interaction and contrast agents' applications in medical ultrasound imaging are covered in chapter 1.1 of the introduction, my published review manuscript on contrast-enhanced ultrasound imaging. Furthermore, the overview of therapeutic applications of microbubbles is presented in chapter 1.2 of the introduction.

Microbubbles are non-linear oscillators, and their non-linear behavior is key to their applications. They scatter ultrasound energy at harmonic and subharmonic frequencies of the transmit pulse, and their vibration's physics is rather complex. The effectiveness of microbubbles in different applications depends on many intrinsic (bubble properties such as size, gas type, shell type, etc.) and extrinsic (such as bubble-bubble or bubble-vessel interactions) variables. Understanding the physics of microbubbles and how these variables change bubble behavior is critical to designing optimal bubble agents and pulse-sequences towards many applications to maximize their effectiveness and outcome. Due to their small size and the many variables affecting their vibrations, using numerical analysis and simulations to study microbubbles is a very attractive approach. Many numerical studies have aimed to understand and explain microbubble dynamics, which are reviewed in chapter 1.3 of the introduction.

Many of the mentioned numerical studies are in simplified formats, using analytical equations that omit certain environmental effects or are only valid under certain conditions. This motivated me to create a simulation environment where we can study microbubbles in more realistic confinements. The model presented in his work allows bubbles to be free; they can deform and interact with each other, the wall around them, and their environment. We implement finite element modeling using COMSOL [5], introduced in chapter 1.3.

Three consecutive steps are present in this work throughout chapters 2-4, which are all either published peer-review articles or manuscripts in preparation. We started with our simulation environment, studying the effect of proximity between two bubbles, and we made it more realistic and complex in finally chapter by adding a vessel wall to study the interaction of bubble-bubble-vessel in their environment. Mathematical methods and simulation factors for each work are explained in the same chapter.

1.1. Ultrasound Contrast Imaging: Fundamentals and Emerging Technology (Manuscript)

This manuscript was published in the Journal of "**Frontiers in Physics**" in February 2022

Authors: Hossein (Sohrab) Yusefi[1], Brandon Helfield[1, 2]

[1]Department of Physics, Concordia University, Montreal, Quebec, Canada
[2]Department of Biology, Concordia University, Montreal, Quebec, Canada

1.1.1. Abstract

The development of microbubble contrast agents has broadened the scope of medical ultrasound imaging. Along with dedicated imaging techniques, these agents provide enhanced echoes from the blood pool and have enabled diagnostic ultrasound to assess and quantify microvascular blood flow. Contrast-enhanced ultrasound is currently used worldwide with clinical indications in cardiology and radiology, and it continues to evolve and develop through innovative technological advancements. In this review article, we present an overview of the basic microbubble physics and bubble-specific imaging techniques that enable this modality, and follow this with a discussion on new and emerging applications.

1.1.2. Introduction

Ultrasound imaging is a well-established clinical tool for the morphological assessment of soft tissues, employed frequently in obstetrics, cardiology, and radiology [6]. As an ultrasonic wave (which is a longitudinal wave) is transmitted into the body, reflections are generated from tissue interfaces that are characterized by different acoustic properties, *i.e.* speed of sound and density. These scattered signals are recorded by the same transmitting transducer and used to generate an image. At typical diagnostic frequencies (≈1-10 MHz), the intrinsic scattering from the blood pool, however, is typically several orders of magnitude lower than tissue due to the size and properties of red blood cells [7]. Consequently, blood appears dark on conventional ultrasound images and

blood flow characteristics cannot be readily assessed. For larger vessels, the relative motion of red blood cells compared to the surrounding tissue can be exploited to assess blood velocity using Doppler techniques [8], a strategy employed in many clinical applications (*e.g.* obstetrics [9], assessment of peripheral artery disease [10], cardiology [11]). This technique has limitations however when dealing with regions of slow blood flow, large tissue motion and/or low hematocrit percentage [6,12].

Ultrasound contrast agents comprise of a suspension of small spheres of gas with a low solubility in blood (*e.g.* perfluorocarbon), typically ranging in size from below 1 μm to 8 μm in diameter. Unlike contrast agents used in other modalities, such as MRI and CT, the relatively large size of ultrasound contrast agents ensures that they remain strictly intravascular and act as red blood cell tracers [13]. Due to the compressibility of their gas cores, microbubbles vibrate about their equilibrium radius in an ultrasound field and possess scattering cross-sections several orders of magnitude higher than a solid particle of the same size [14]. The bubbles are stabilized by a thin bio-compatible encapsulation layer - typically a phospholipid monolayer, to offer a sufficient compromise between bubble vibration flexibility and resistance to dissolution *in-vivo* over timescales relevant for imaging, *e.g.* half-lives of minutes [15,16].

Microbubble suspensions, typically on the order of 10^9 bubbles/ml, are injected intravenously into a peripheral vein in the arm [13], with a whole-body dose ranging from 0.2 – 2 ml. There have been millions of diagnostic injections of contrast agent microbubbles worldwide [17], and they are accompanied by an excellent safety profile. Recent meta-analysis surveying microbubble tolerance indicates that the dominant cause of severe adverse effects is pseudoanaphylaxis (CARPA), with an estimated rate on the order of 0.004%-0.009% [18]. This rate is comparable to most analgesics and antibodies (0.005%-0.015% [19]), and similar if not lower than for other contrast imaging

agents, *e.g.* CT with a rate of 0.04% [20], MR with a rate of 0.002%- 0.005% [21,22]. Table 1.1 lists the clinical contrast agents, along with details on their salient characteristics and clinically approved applications. Microbubbles are approved in over 70 countries, predominately for cardiac applications, whereby their strong echo signal in the heart chambers improves left ventricular opacification (LVO). Recently, Lumason^{TM} was approved for liver imaging and in various pediatric applications [23]. Aside from the clinical uses listed here, microbubbles are currently in use worldwide in many off label clinical imaging applications, including assessment of microvascular perfusion (*e.g.* myocardial [24], angiogenesis imaging [25]), imaging of the carotid to assess vascular stenosis [26] and plaque stability [27], lesion and flow characteristics in the abdominal region [28,29], breast lesion detection [30], evaluation of inflammatory bowel disease [31], and assessment of ovaries [32], prostate [33] and thyroid [34].

In this review, we present an overview of this established yet evolving imaging modality. First, we present a brief summary of the fundamental physics of microbubble behaviours that are critical for the effectiveness of this approach, followed by an introduction to the main conventional pulse sequences that are designed to exploit these behaviours to generate bubble-specific images. Next, we discuss exciting advancements in the techniques and applications of ultrasound contrast imaging, including the development of emerging contrast agents, novel imaging and image analysis techniques, and the implementation of contrast ultrasound as a therapy monitoring technique. Note that this is not a comprehensive review, rather an overview of the critical work that has defined this modality and salient investigations into new and ground-breaking applications.

1.1.3. Ultrasound-Microbubble Interactions

A gas-filled microbubble vibrates when traversing through an acoustic beam, contracting and expanding about its equilibrium radius R_0. Almost all the current models that explain the oscillation dynamics of a bubble have their origin in Rayleigh-Plesset-type equations [35], which describe the radial motion of an isolated, unencapsulated bubble. This equation, which only incorporates spherical vibrations, can be derived by applying Newton's third law to the surface of a bubble and equilibrating the pressure on the bubble wall from the gas inside and the surrounding fluid media outside, resulting in the following equation:

$$\mathrm{R\ddot{R}} + \frac{3}{2}\dot{R}^2 = \frac{1}{\rho}\left[\mathrm{P_{G0}}\left(\frac{\mathrm{R_0}}{\mathrm{R}}\right)^{3\gamma} + \mathrm{P_v} - \frac{2\sigma}{\mathrm{R}} - 4\eta_{\mathrm{L}}\frac{\dot{\mathrm{R}}}{\mathrm{R}} - \mathrm{P_0} - \mathrm{P_{ac}(t)}\right] \tag{1.1.1}$$

where R is the radius of the bubble, ρ is the density of the liquid, $P_{G0} = P_0 - P_v + 2\sigma/R_0$ is the pressure inside the bubble with P_0 the atmospheric pressure, P_v the vapor pressure inside the bubble and σ is the surface tension at the gas-liquid interface, γ is the polytropic exponent of the gas; η_L is the dynamic viscosity of the liquid; P_{ac} is the driving acoustic pressure due to the ultrasound field and dots denote differentiation with respect to time. From fundamental fluid dynamic principles, including conversation of mass and momentum, the microbubble scattered pressure P_{sc} due to its vibration can be approximated by

$$P_{SC} \approx \rho\frac{\ddot{R}R^2 + 2R\dot{R}^2}{r} \tag{1.1.2}$$

Name	Gas Core	Shell Material	Conc. (10^9 bub/ml)	d_N (µm)	d_V (µm)	f_{res} (MHz)	Approved Uses	Region	Company
Definity (Luminity)	C_3F_8	DPPA, DPPC, MPEG5000 DPPE	8-13 [36–38]	< 1.0 [36,39]	6-8 [36,40]	~10 [36,41]	- LVO/EBD (adults)	USA, Canada, Europe, India, NZ, Australia	Lantheus
Lumason (Sonovue)	SF_6	DPSC, DPPG-Na, palmitic acid	0.1-0.5 [38]	1.5-2.5 [42]	6 [43]	~2 [43]	- LVO/EBD (adults and pediatric patients) -Characterization of liver lesions (adults and pediatric patients) - Evaluation of suspected or known vesicoureteral reflux (pediatrics)	USA, Canada, Europe, China, Brazil	Bracco
Optison	C_3F_8	Albumin	2-8 [38,43,44]	3-4.5 [38]	6-7 [38,45]	2-4 [44]	- LVO/EBD (adults)	USA, Europe	GE
Sonazoid	C_4F_{10}	Hydrogenated egg phosphatidylserine sodium, sucrose	1.2 [46]	2.1[38, 46]	2.6 [46]	4-6 [47]	-Myocardial perfusion -Living imaging -Focal breast lesions	Japan, South Korea, China, Norway, Taiwan	Daiichi-Sankyo / GE

Table 1.1: Current clinical contrast agent microbubbles, their salient characteristics, and their approved uses.

where r is the observational distance from the bubble surface. In the context of ultrasound imaging, bubble activity is commonly separated into two acoustic regimes that give rise to distinct spectral features. Under low amplitude driving conditions at frequency f, microbubbles undergo periodic oscillations about their equilibrium size resulting in echoes that possess a rich resonant structure, exhibiting energy at harmonic ($nf, n = 2,3$ ...), sub-harmonic ($^{f}/_{(n+1)}, n = 1,2,$ ...) and ultra-harmonic ($(2n+1)f/2, n = 1,2$ ...) frequency bands (Fig. 1.1a&b). This type of cavitation is called stable (or non-inertial) cavitation, which is typically desired in routine contrast examinations. When the acoustic pressure is increased above a threshold value, microbubbles can rapidly expand and collapse during the compression phase of the ultrasound wave resulting in a transient, high-amplitude echo characterised by broadband emissions. As this bubble collapse is dominated by the inertia of the surrounding fluid, it is often referred to as inertial cavitation [48]. Quantitative indicators of inertial cavitation on an individual microbubble scale have been suggested, including when the maximum bubble radius $R_{max} \geq 2R_0$ otherwise known as the Flynn criteria[49]. The disruption of microbubbles results in an immediate loss of gas and thus in a time-dependent loss of contrast signal. On clinical scanners, the mechanical index $MI = {}^{P}/_{\sqrt{f}}$, where P is the peak-negative pressure amplitude in MPa and f is the centre frequency in MHz, is a metric used to estimate the likelihood of inertial cavitation and is generally maintained at low values to minimize bubble destruction [50]. Indeed, across the broad spectrum of all clinical contrast imaging applications, it is recommended to start at the manufacturers default contrast MI. If perfusion is still not well visualized after exhausting other image-enhancing strategies (*e.g.* receiver gain), then the MI should be increased by the smallest increment allowed on the given clinical system [23], with a maximum recommended MI between 0.2-0.3 [51–53]. However, specific techniques have been developed (*e.g.* disruption-replenishment [54,55]) whereby short

duration, large MI pulses (*e.g.* high MI flash under the FDA limit of MI=1.9) are employed to purposefully disrupt microbubbles in the focal volume, followed by a rapid switch back to low MI imaging pulses. The rate at which these bubbles replenish the imaging plane can be used to assess blood flow characteristics upon application of relatively simple models [54,55]. The specific MI that elicits microbubble disruption has been the subject of much investigation [56–60] and has been shown to be dependent on microbubble formulation, size, and surrounding environment.

Ultrasound-driven microbubble response is resonant in nature, and the resonance frequency is one of the important factors in agent design and optimization. Under low acoustic driving conditions, the nonlinear equation of motion Eq. (1.1.1) can be reduced to one of a harmonic oscillator with a linear resonance frequency f_0 given by:

$$f_0 = \frac{1}{2\pi}\sqrt{\frac{3\gamma P_0}{\rho R_0^2} + \frac{2\sigma(3\gamma - 1)}{R_0^3}} \tag{1.1.3}$$

where an inverted relationship between resonance frequency and size can be observed. The addition of an encapsulating shell has led to adjustments of Eq. (1.1.1), which incorporate the viscoelastic properties of the thin shell, *i.e.* shell stiffness and viscosity. While many models have been developed to capture various aspects of microbubble physics, under low-amplitude transmit pressure conditions they are all in agreement with experimental observations which confirm that the encapsulating layer serves to increase the resonance frequency and the vibration dampening of an otherwise identical bubble (Fig. 1.1c). As driving amplitudes increase, microbubbles display nonlinear resonance phenomena, including strain-softening behaviour resulting in asymmetric resonance curves shifting to lower resonance frequencies [61,62] (see Fig. 1.1d).

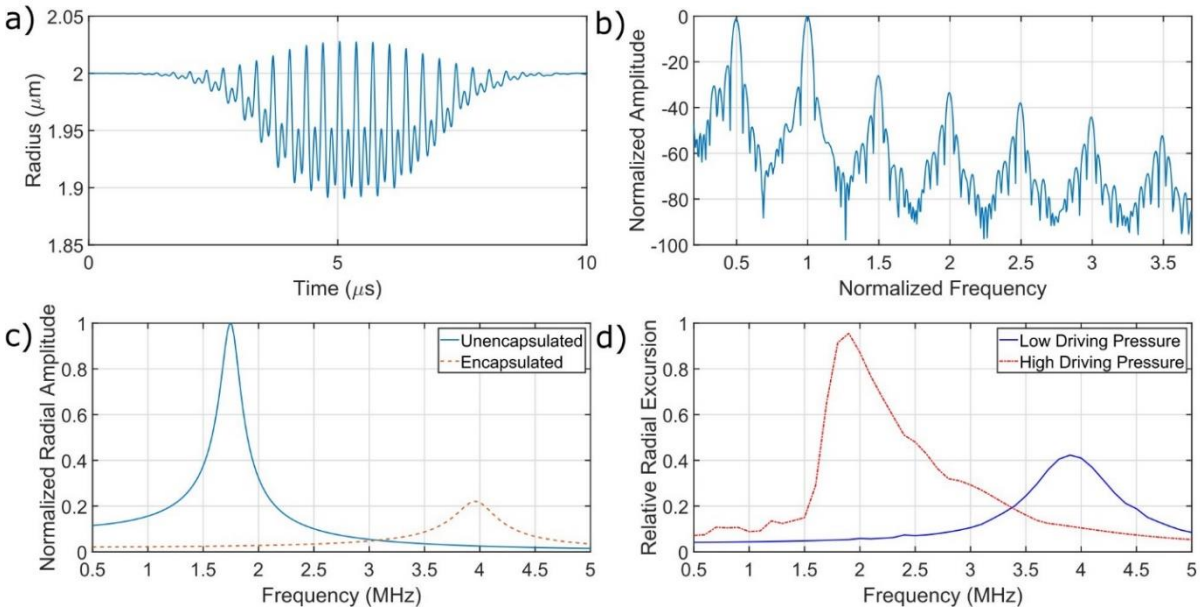

Figure 1.1. Illustrative microbubble simulations depicting its resonant and nonlinear behaviour. a) Radius versus time of an oscillating microbubble and b) it's corresponding frequency content. Note the presence of subharmonic (0.5), ultraharmonic (1.5, 2.5, 3.5) and harmonic (2,3) energy, as well as energy at the fundamental frequency band (1). c) The presence of an encapsulating shell serves to increase the resonance frequency and dampen the vibrational amplitude of an otherwise identical microbubble. d) Under large forcing conditions, microbubbles exhibit asymmetrical resonance, including a shift down in resonance frequency with increasing forcing amplitude. Note here the inherent skewing of the resonance response, typical of a strain-softening resonator.

While these nonlinear behaviours can be generated by unencapsulated gas bubbles [63], the surface rheology of the encapsulation material at megahertz oscillations plays a key role in amplifying these effects [64]. As such, there have been extensive efforts to understand the underlying physics of encapsulated microbubble vibration dynamics, including asymmetric oscillations [65], nonlinear resonance [66], multiple scattering [45], and boundary effects [67].

1.1.4. Contrast Pulse Sequences

Nonlinear behaviour of vibrating microbubbles is central to their effectiveness as an ultrasound contrast agent. These emissions provide a means to separate bubble signals within small vessels from those of the surrounding (approximately linear) tissue (Fig. 1.2). Original methods of bubble

detection consisted of harmonic imaging, whereby energy at the second harmonic (twice the driving frequency) was collected and filtered from the receive signal. Since microbubbles generate much larger second harmonic signal than tissue, this results in better signal-to-noise ratios than that from the fundamental energy. This approach however requires long-duration (narrowband) transmit pulses in order to ensure separation of the spectral components at f and $2f$, as well as to fit within the transducer bandwidth. These conditions result in decreased axial resolution and ultimately a trade-off between image resolution and contrast quality. Multi-pulse contrast imaging pulse sequences, consisting of pulse inversion (PI; [29]), amplitude modulation (AM; [68]) and combinations thereof (contrast pulse sequences, CPS; [69]), have been developed to circumvent these issues to specifically image the blood pool with high specificity and sensitivity. The following sections briefly outline these two main approaches; for a more exhaustive survey of microbubble-specific imaging methods, the reader is referred to a recent review article [70].

1.1.4.1. Pulse Inversion

The generalized scattered signal from a scatterer $O(x(t))$ can be modeled by a polynomial expansion:

$$O(x(t)) = \sum_{m=1}^{\infty} a_m x^m \tag{1.1.4}$$

where $x(t)$ is the transmit waveform. The contributions of the nonlinear components are defined by the coefficients a_m, whereby for linear systems only a_1 is nonzero.

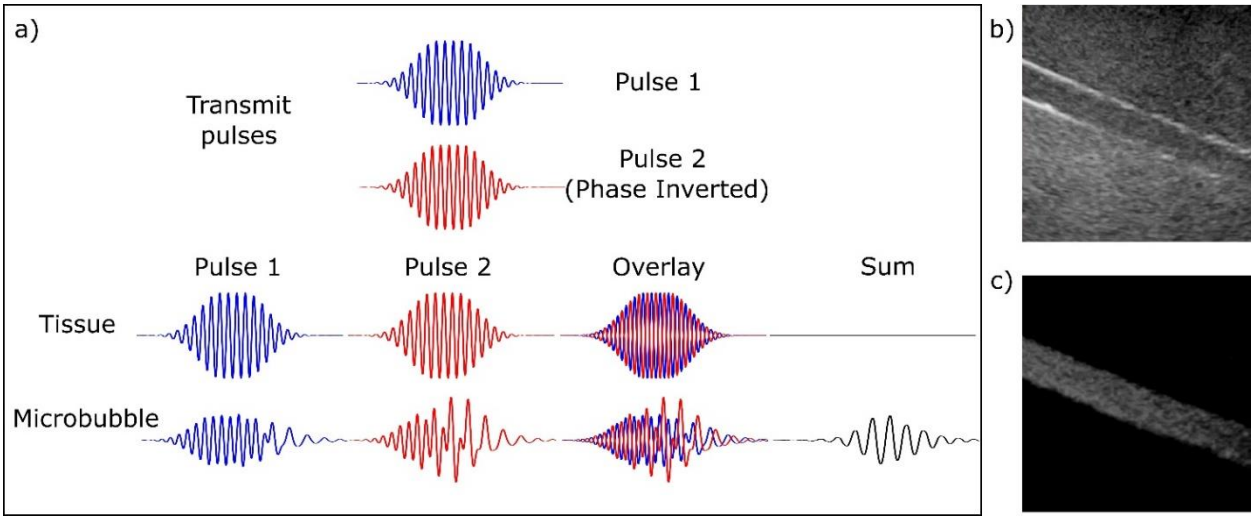

Figure 1.2. Microbubble-specific imaging sequences capture nonlinear signal from contrast agent while rejecting linear scattering tissue. a) Schematic diagram depicting the pulse inversion technique. Two pulses that are 180 degrees out of phase will result in tissue echoes that are similarly out of phase. However, this is not the case for microbubbles due to their nonlinear behaviour. The summed echo results in near complete cancellation for linear tissue and significant signal from echoes generated from microbubbles. b) B-mode and c) contrast-specific imaging of an 8mm vessel phantom highlights the increased vessel contrast due to microbubble-specific imaging. This was acquired with a Philips iU22 scanner using a C5-2 probe and DefinityTM contrast agent.

As ultrasound pulses consist of sinusoidal transmit sequences, *e.g.* $x(t) = \cos(\omega t)$ with $\omega = 2\pi f$ the angular transmit frequency, the nonlinear echo can be approximated by

$$O(x(t)) \approx a_1 \cos(\omega t) + \frac{a_2}{2}[1 + \cos(2\omega t)] + \frac{a_3}{4}[\cos(\omega t) + \cos(3\omega t)] + \frac{a_4}{8}[3 + 4\cos(2\omega t) + \cos(4\omega t)] + \cdots \quad (1.1.5)$$

Note from the above equation that even-order terms create echoes at even harmonics (and DC), while the odd-order terms account for echoes at the fundamental frequency and odd-order harmonics. The pulse inversion multi-pulse sequence consists of sending in two transmit pulses

that are 180 degrees out of phase with each other (Fig. 1.2a). Upon summation of the resulting echoes $s(t)$, the linear contributions are removed and only even order harmonic signal is retained:

$$s(t) = O_1\big(x(t)\big) + O_2\big(-x(t)\big) = 2\sum_{m=1}^{\infty} a_{2m}x^{2m} \tag{1.1.6}$$

While this technique suppresses fundamental signal, it still requires careful selection of transmit frequency to be able to sensitively detect even order harmonics with the given transducer.

1.1.4.2. Amplitude Modulation

In a similar attempt to preserve nonlinear contributions, amplitude modulation consists of transmitting a sequence of pulses that are scaled by a constant factor. Typically, the echoes received from $x_1(t)$ and $x_2(t) = {}^1\!/_2\, x_1(t)$ (referred to as 'full amplitude' and 'half-amplitude' pulses respectively) are scaled and subtracted, resulting in a residual signal $s(t)$ defined as:

$$s(t) = O_1\big(x_1(t)\big) - 2O_2\left(\frac{1}{2}x_1(t)\right) \tag{1.1.7}$$

This results in a signal that partially retains all harmonics, including signal at the fundamental frequency; shown here to third order:

$$s(t) \approx \frac{a_2}{4}[1 + \cos(2\omega t)] + \frac{3a_3}{16}[\cos(\omega t) + \cos(3\omega t)] + \cdots \tag{1.1.8}$$

It is important to note here that the signal component within Eq. 1.1.8 at the driving frequency ω represents the scaled difference in the fundamental component due to different amounts of nonlinear signal in the two driving pulses. This 'nonlinear fundamental' signal results from the

fact that microbubbles exhibit nonlinear resonance characteristics, specifically an amplitude dependent resonance frequency (Fig. 1.1d). As such, the fundamental microbubble response will not necessarily be linearly proportional to the input transmit pressure, *e.g.* the response from $x(t)$ will not be twice that of $\frac{1}{2}x(t)$. Indeed, bubble-specific strategies are currently under development that exploit the accompanying echo phase lag associated with this phenomenon [71]. While this approach retains less even-order harmonic energy than PI, the residual 'nonlinear fundamental' is particularly useful as it can be well detected within the transducer bandwidth.

Both PI and AM methods can be performed using three or more pulses, offering some advantages in tissue rejection at the cost of temporal resolution. The combination of these two approaches (PIAM, or CPS) retains similar levels of odd-order nonlinear energy as AM while preserving more even-order harmonics, albeit less than the PI technique alone.

1.1.5. Emerging Technologies

Contrast-enhanced ultrasound imaging is employed in many clinically approved and off-label applications worldwide. Cutting-edge advancements in this area are being made simultaneously on many fronts, including contrast agent synthesis, the design of novel pulse sequences and image processing techniques, device development, and on the development of remote monitoring for ultrasound therapeutics (Table 1.2).

1.1.5.1. Contrast Agents

Microbubbles are currently the only clinically approved ultrasound contrast agent. One of the strengths of these bubbles is that they remain intravascular due to their size, allowing for diagnostic measurements that would be otherwise difficult with diffusible tracers. However, there is a

Emerging Technology/Technique	Concept	Applications
New contrast agents	To design novel acoustically-sensitive agents that allow for the extraction of diagnostic information otherwise impossible with standard microbubble contrast agents	*Targeted microbubbles*: Molecular imaging of vascular-based markers of disease (*e.g.* thrombosis, angiogenesis, ischemia) *Droplets/nanobubbles:* Extravascular imaging in cancer applications *Gas vesicles:* Acoustic reporter genes, environmentally-triggered acoustic reporters
Super-harmonic Imaging	To use higher order harmonic signal unique to microbubble vibrations to generate high contrast-to-tissue ratio contrast images	Tumor vasculature imaging
Non-invasive pressure estimation	To extract ambient pressure information from microbubble acoustic signatures	Portal vein hypertension, intra-cardiac measurements
Ultrasound Localization Microscopy	To use bubble localization information to generate images that surpass the diffraction limit	Tumor vasculature imaging, neurological
Microbubble-therapy monitoring	To extract qualitative and quantitative microbubble emission characteristics as a surrogate for therapeutic endpoints	Cardiovascular and cancer-based applications of focused ultrasound therapy, immunotherapy, and microbubble-mediated therapeutic delivery

Table 1.2: Summary of emerging ultrasound-microbubble based techniques. See text for references and further details.

growing focus to extend the use of these 'traditional' ultrasound contrast agents towards other applications, including molecular-based imaging, imaging of the extravascular space, and as a dual imaging and therapeutic delivery platform.

1.1.5.1.1 Molecularly Targeted Microbubbles

Non-invasive imaging of pathophysiological events has recently been shown feasible with ultrasound due to the synthesis of functionalized microbubbles [72], *i.e.* microbubbles with one or

more targeting moieties incorporated into the phospholipid encapsulation [73]. Due to the strictly intravascular nature of microbubbles, target sites have aimed at processes that occur within the vasculature, such as inflammation [74], angiogenesis [75], and thrombus formation [76]. This technique has shown significant pre-clinical promise, with agents synthesized to target key endothelial biomarkers involved in disease, *e.g.* ICAM-1 [77], VCAM-1 [74], $\alpha_V\beta_3$ [78], E-selectin [79]. Clinical trials to assess safety and tumor detection sensitivity have shown encouraging results using microbubbles functionalized for vascular endothelial growth factor receptor 2 (VEGFR2) in ovarian, breast and prostate cancer [80,81]. Indeed, this technique can be used as a means for early differential disease detection, as pathological molecular expression often occurs at an earlier timepoint in relation to anatomical changes – but it can also be used as a tool for non-invasive therapy monitoring [82]. In either case, the objective is to establish a proportional relationship between detected bound bubble signal and the level of target molecule expression. Part of this strategy is therefore to preferentially detect signals from bound bubbles, as distinct from freely circulating, or non-bound stationary agent. While there have been some suggestions of novel echo characteristics that would specifically indicate a bound versus unbound bubble [83,84], imaging techniques to exploit this behaviour are not yet used robustly in practice. Instead, a number of approaches have been developed to estimate adherent bubble signal, one of which is to exploit the increased persistence of bound bubbles. Exploiting the relatively short half-life of freely circulating microbubbles, image acquisition ~10 min. post injection will preferentially capture bound bubble signal [85]. Another strategy is to first acquire a baseline image consisting of all bubbles (both bound and unbound) and to apply a large magnitude pulse to disrupt them [72]. Contrast images are then acquired immediately post-disruption to monitor the reperfusion of circulating microbubbles into the imaging plane. The bound-bubble specific image is then

estimated as the difference between the pre- and post-burst images. A third approach is to exploit the increased decorrelation due to motion associated with circulating bubbles relative to stationary ones. While this has shown significant promise in pre-clinical testing [86], it is expected to have limitations in regions of substantial tissue motion.

Despite the relative success of the aforementioned bound bubble quantification techniques, only a small fraction the injected microbubbles bind to the activated endothelium, on the order 1-2% [87]. A clever approach to increase the number of microbubbles that make direct contact with the endoluminal border is through the use of acoustic radiation force, originally postulated for such a purpose over two decades ago [88,89]. Acoustic radiation forces, otherwise known as Bjerknes forces, are the forces imparted to a small object within an acoustic beam by the acoustic wave [12]. In the context of ultrasound-stimulated microbubbles, the primary Bjerknes force magnitude F directed away from the transducer experienced by a resonating microbubble in a pulsed field of duty cycle D and pulse repetition interval T can be estimated as [90]

$$F = \frac{P^2 R_0}{\delta \rho c f_0}\left(\frac{D}{T}\right) \tag{1.1.9}$$

where δ is the damping coefficient [91] and c is the speed of sound. Secondary Bjerknes force, which is the force ascribed to the translational dynamics between two vibrating microbubbles, can also be shown to be highly dependent on microbubble size and separation distance [90]. While the physical acoustics of these phenomena have long been investigated [92,93], it has been since utilized as an approach to increase microbubble binding efficiency [90,94,95]. Quantification of acoustic radiation force (ARF)-enhanced microbubble imaging can be performed using a relative

measure of bubble signal pre- and post-ARF burst, allowing for an attenuation-independent measure of quantification (*i.e.* one that does not rely on the absolute signal intensity) [96,97].

1.1.5.1.2 Sub-micron Contrast Agents

Motivated by the enhanced-permeability and retention effect [98], whereby small nanometer sized particles locally extravasate from leaky blood vessels and accumulate in the perivascular space of solid tumors, there are numerous ultrasound-sensitive sub-micron agents currently under investigation. These mainly include phase-shift droplets [99], nanobubbles [100], gas vesicles [101], echogenic liposomes [102], and polymeric nanoparticles [103]. Perhaps the most well-studied of these are volatile, phase-shift sub-micron droplets synthesized from perfluorocarbons (PFCs). As a liquid, droplets provide limited acoustic contrast and are generally not detectable with conventional ultrasound. However, under externally applied ultrasound conditions, these droplets can be acoustically vaporized into detectable, micrometer-sized bubbles approximately 5-10 times their precursor size [104]. Droplet compositions generally consist of PFCs due to their low toxicity, low solubility and their boiling points near physiological temperatures [99], allowing the design of droplets in or near a superheated state. As these superheated droplets are thermodynamically unstable, they are stabilized through phospholipid encapsulation – reducing surface tension and inhibiting diffusion of the PFC into the surrounding medium. Indeed, droplets can be synthesized directly from pre-cursor microbubbles, *e.g.* commercially employed agents such as Definity^{TM} [105,106]. While the physics of acoustic droplet vaporization is still an active area of research, the process likely involves both intrinsic (*e.g.* PFC, encapsulation material) and extrinsic (*e.g.* sound and its propagation medium) factors. The vaporization threshold of individual droplets empirically exhibits a size-dependence, with larger, micron-sized droplets requiring lower pressures to vaporize [104,107,108]. Further, there is an increasing threshold with decreasing

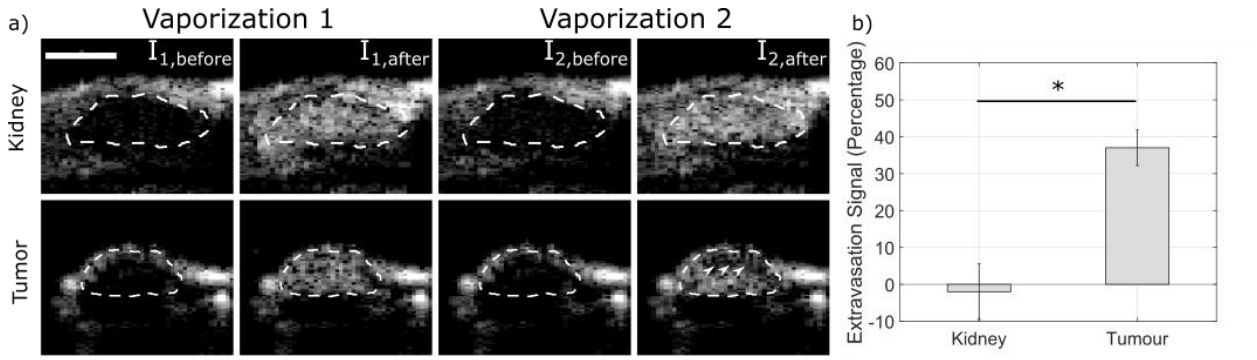

Figure 1.3. Estimated droplet extravasation signal is larger in tumor than in kidney. a) Two successive vaporization sequences (Vaporization 1 and 2) separated by 30 seconds were transmitted to both the kidney (highly intravascular organ) and tumor xenograft (intravascular and extravascular components) in a mouse model, outlined in the dashed lines. The white arrowheads denote the lack of signal enhancement from the second vaporization pulse within the tumor, suggesting droplet extravasation. Scale bar is 5 mm. b) Quantification of extravasation signal ($p<0.001$). Reprinted by permission of Elsevier from Helfield et al. Ultrasound and Medicine and Biology, 2020 [109]**, see the reference for more details.**

frequency [110] – indeed these two factors make the vaporization of small, sub-micron droplets at clinically relevant frequencies a challenge. However, recent translational studies using pre-clinical and programmable array systems have shown the feasibility of *in-vivo* image-guided vaporization and extravascular imaging [109,111], see Figure 1.3.

As an alternative to phase-shift low-boiling point droplets, recent studies have begun to explore nanobubble contrast agent, typically on the order of several hundred nanometers in size [112]. According to classical models (*e.g.* Eq. [1.1.1] and Eq. [1.1.3]), nanobubbles are not expected to undergo significant vibrations and scattering at clinically relevant frequencies (*e.g.* 1-10 MHz). However, studies have demonstrated scattered emissions from nanobubbles at both low [113,114] and high frequencies [115]. The increased concentration of nanobubbles per unit volume may compensate for the weak scattering from an individual nanobubble, and bubble coalescence (multiple nanobubbles combining to form a microbubble) may also play a role in the observed

signal. In addition to these aspects, recent surface modifications (surfactants, *e.g.* Pluronic) to nanobubble encapsulation layers has been suggested as a potential mechanism to further reduce surface tension and increase flexibility [112,114]. Regardless of the mechanism, observations of intact nanobubbles in the extravascular space have very recently been documented [116,117].

Recently, a new and exciting type of biologically-derived, sub-micron ultrasound contrast agent has been developed by harnessing gas vesicles (GVs) [101]. These vesicles, which were originally identified within gas vacuoles of cyanobacteria, function natively to regulate cellular buoyancy for optimal exposure to light and nutrients [118]. GVs are inert, hollow, gas-filled structures formed entirely from protein. The main consistent is a small protein (GVpA) arranged in a linear crystalline array along ribs that form the GV shell and conical caps. A second protein (GVpC) adheres to the outside of the ribs and stabilizes the structure. These vesicles are freely permeable to gases and liquid water is kept out due to surface tension at the hydrophobic inner surface. GVs have been found in many prokaryotes (*e.g.* bacteria and archaea), and extensive research has concluded that these GVs possess similar morphology and are constructed from a homologous protein. The size and shape of GVs is a function of the species that generate them, but they are typically cylindrical or spindle-liked shaped, with lengths ranging from 0.1 to 2 μm and widths between 45-200 nm [119]. While similar in principle to other pre-formed sub-micron agents, GVs are rigid, non-spherical structures. In the pioneering work by Shapiro et al. [101], purified GVs generated from *Halobacterium salinarum* (Halo) produced robust contrast using a pre-clinical scanner, including nonlinear harmonic content *in-vitro* and in mouse liver using an amplitude modulation pulse sequence (*e.g.* Eq. [1.1.7]). Since then, many experimental and theoretical investigations have confirmed that GVs are able to elicit nonlinear signal and acoustically-mediated collapse *in vitro* and *in-vivo* [120,121], which highlight the potential of GVs to serve as

background-subtracted imaging agents. However, perhaps the greatest differentiator between GVs and traditional ultrasound contrast agents is their ability to be genetically modified. Indeed, the acoustic properties of GVs can be modified at the level of their constituent proteins [122], which enables the concept of environmentally-modulated nonlinear contrast signal (*e.g.* detecting the presence of specific proteases [123]). Further, recent work has demonstrated the capacity of GVs to act as an acoustic reporter gene in mammalian cells (*e.g.* an acoustic version of an optical reporter like green-fluorescent protein), whereby contrast signal can be correlated to genetic expression [124].

1.1.5.2. Super-Harmonic Imaging

As microbubble vibrations possess a rich resonant structure (Fig. 1.1b), there have been recent developments towards generating contrast images using microbubble super-harmonic frequency components, defined as third-order harmonics and higher ($nf;\ n = 3,5,6\ ...$). An extension of traditional second harmonic imaging techniques, the selective reception of these higher-frequency signals results in higher image resolution and contrast-to-tissue ratios compared to standard contrast imaging sequences. Due to the bandwidth of standard clinical transducers, which limits its ability to transmit and receive signals at both the fundamental and super-harmonic energy bands, the implementation of this approach requires multiple, independent transducer elements. This can be accomplished by designing novel phased arrays with interleaved elements for transmit and receive [125,126], and confocally aligned dual-element transducers [127,128]. Recent incarnations of this approach, termed acoustic angiography [129], performs super-harmonic imaging using transmit frequencies between 2-4 MHz and receives echo signal from 25-30 MHz. Using this device, an *in-vivo* resolution of 150-200 μm and a contrast-to-tissue ratio of 20 dB has been demonstrated [130,131]. To date, this technology has been employed to image and assess

tumor microcirculation [132,133] and remains mostly pre-clinical; although very recent work highlights its potential for clinical translation [134,135] and is currently an active area of research.

1.1.5.3. Non-Invasive Pressure Estimation

Local blood pressure estimation provides valuable clinical information on the physiology of many organs, and can be employed in the diagnosis of disease in the heart and kidneys. Most current clinical techniques to assess blood pressure within non-limb vessels use catheter-based manometers, which is an invasive approach and introduces changes to the local blood circulation and thus the blood pressure. Perhaps one of the most impactful applications of non-invasive pressure estimation would be for the early detection of clinically significant portal vein hypertension, defined as an increase in the pressure gradient between the portal vein and hepatic veins exceeding 10 mmHg [136]. As noted almost four decades ago [137], bubble response is a direct function of the ambient hydrostatic pressure and may, in principle, be used as a pressure sensor to detect fluctuations in local blood pressure. An increase in ambient pressure effectively compresses the microbubble, resulting in a shift upwards in resonance frequency. For a given transmit frequency, this will manifest itself in the amplitude of the resulting scattered echo. These original works performed on unshelled bubbles resulted in large uncertainties (as much as 30%, or 50 mmHg compared to reference standards [138]) due to the challenge of detecting the relatively small shift in resonance frequency (~1 kHz shift from a change in 10 mmHg). While the rheological characteristics of phospholipid encapsulated microbubbles results in much larger resonant shifts (~0.07-0.24 MHz per 10 mmHg[139]) that may be sufficiently detectable for clinical utility, major advances in this application of remote blood pressure estimation are derived from investigations into the modulation of subharmonic scattering. Based on earlier works on commercially available contrast microbubbles that indicate a decrease in subharmonic scattering

with increasing hydrostatic pressure [140], subharmonic-aided pressure estimation efforts (referred to as SHAPE [141]) have met initial success in pre-clinical models [142,143] and in clinical trials for portal hypertension [144] and intra-cardiac measurements [138].

1.1.5.4. Ultrasound Localization Microscopy

A flourishing research area within diagnostic ultrasound is the development, implementation and interpretation of ultrafast ultrasound imaging, in which up to 20 kHz frame rates (compared to 10–100Hz using conventional scanners) can be achieved through advances in hardware and software. This concept is based off the transmission of an ultrasonic plane wave (*i.e.* unfocused beam), which avoids the time-consuming process of sequential scanning and beamforming conducted by traditional focused-mode imaging. The echoes from a single plane wave transmission are received by the transducer elements and subsequently processed and beamformed in parallel. While the use of a single, unfocused transmit beam results in poor image resolution, SNR can be markedly increased by transmitting multiple plane waves at different angles and compounding the coherent beamformed images. Despite this slight subsequent reduction in frame rate, this still results in a very fast acquisition relative to conventional focused beam, limited in principle only by the two-way speed of sound in tissue. Ultrafast plane wave imaging has opened an array of contrast and non-contrast ultrasound applications that take advantage of such increased temporal resolution, including ultrafast elastography [145], cardiac [146], and Doppler- based applications [147].

Perhaps the most disruptive technique derived from a microbubble-based application of this technology to date is ultrasound localization microscopy (ULM) [148]. As a super-resolution imaging technique, it has begun a paradigm shift in biomedical ultrasound imaging applications despite many previous investigations into methods to improve ultrasound imaging resolution. In

standard imaging techniques, image resolution is bound by diffraction to the scale of the wavelength; for example, in a 6-MHz ultrasound imaging system ($\lambda = 250$ μm), the diffraction

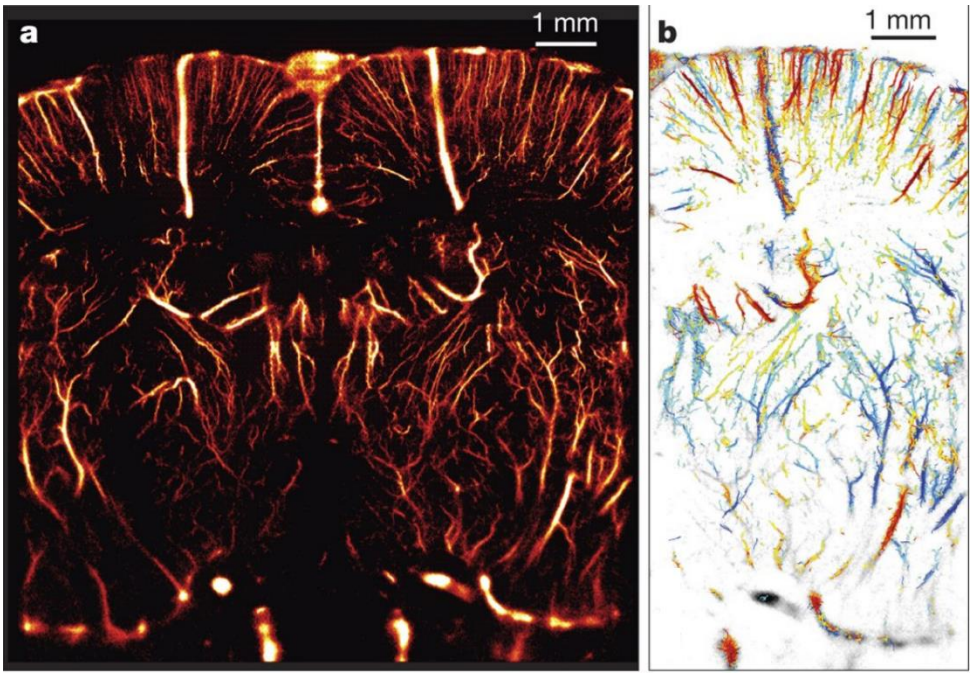

Figure 1.4. An example of ULM applied in a rat brain through a thinned, intact skull providing a resolution of 10μm x 8 μm in depth and lateral direction, respectively. Reprinted from [149] **with permission from the authors and Nature Publishing Group.**

limit is 125 μm ($\lambda/2$). The ULM approach exploits the localization of microbubbles to finely sample and image the microcirculation beyond the limit imposed by diffraction, showing impressive results in the areas of oncology [132,150] and neurology [149,151] that result in an improvement of the resolving power of ultrasound up to a factor of 10 compared to the diffraction limit [152,153]. It is an approach inspired by the light microscopy counterpart; photoactivated localization microscopy (PALM) and stochastic optical reconstruction microscopy (STORM). These cutting-edge light microscopy techniques, which can image beyond the diffraction limit by an order of magnitude [154–156], rely on photoactivatable fluorescence probes that display unique

spectral features upon exposure to different wavelengths of light. These reversible, 'photo-switchable' probes in combination with fast-frame imaging cameras enable the rapid acquisition of frames in which only a subset of the sources is visible. With knowledge of the point-spread function of the imaging system, the collection of many sub-wavelength localizations can be reconstructed with resolution lower than the diffraction limit. Indeed, the development of these techniques was so important that it led to the attribution of the 2014 Nobel prize in Chemistry to Eric Betzig, Stefan Hell and William E. Moerner.

An ultrasonic version of super-resolution is achieved by replacing the fluorescent markers with microbubbles (which are sub-wavelength, individual acoustic sources), and the fast cameras with plane-wave, programmable ultrasound imaging systems. These programmable systems give access to the pre-beamformed time-domain data (RF data), whereby assuming a single source, the signal time delay τ as a function of array position x produced by a single microbubble echo propagating at a constant speed c is given by:

$$\tau = \frac{\sqrt{z_0^2 + (x - x_0)^2}}{c} \tag{1.1.10}$$

where z_0 and x_0 are the depth and lateral position of the microbubble, respectively. One approach to microbubble localization is to fit this delay function (*i.e.* a parabolic function), the peak of which will provide the position of the microbubble at much higher resolution than the wavelength [148]. Alternatively, even on beamformed images acquired from conventional ultrasound scanners, various algorithms have been developed to estimate the intensity-weighted centroid of an individual microbubble and has shown success in dilute microbubble applications [157,158].

The general concept of acquiring a super-resolution imaging using ULM will next be outlined here. After injection of a dilute suspension of contrast agent, video acquisition of the location of interest, either using B-mode or contrast-specific sequences, can be taken using either conventional beam or fast-frame plane wave techniques. Since the resulting ULM image is constructed point by point, a sufficient quantity of microbubbles is required to reconstruct the vasculature, on the order of 1 million events [149] depending on the vessel density and field of view. Given the relatively slow blood velocities in the microvasculature, this often requires long image acquisition times and results in a vast amount of data for processing. Motion correction algorithms are next applied to minimize motion-related localization artefacts, which present a particular challenge due to these long scan times. Various techniques have been demonstrated within the context of the ULM workflow, including phase-correlation approaches between successive B-mode images, all of which result in corrections on the order of hundreds of micrometers for in-plane motion [159–161]. While out-of-plane motion correction is not possible using this 2D approach, 3D ULM techniques are currently being assessed [162]. Following this, a microbubble-filtering processing step is introduced, which can include isolating nonlinear emissions [151,157] as well as alternative image processing strategies including spatiotemporal-based filtering algorithms [149,161,163]. Microbubble localization is then performed by estimation of its centroid using either the raw RF data or the beamformed image. A critical challenge here is the reliable separation of one microbubble from another. The most direct way of localizing a single microbubble is to use a low concentration of contrast agent (*e.g.* 10^6 bubbles/ml) [151,157,164], which guarantees an inter-bubble spacing (*e.g.* 100 μm) of several imaging wavelengths at traditional transmit frequencies. Even in such instances, the robust SNR generated from an individual microbubble is of paramount importance, and will ultimately affect the ULM resolution. Recent work [165] has suggested that

exploiting the phase response of vibrating microbubbles, a property linked to their resonant nature [91], can increase ULM image quality. However, there are emerging alternative strategies that allow for higher local doses of microbubbles, attempting to circumvent the spatial resolution versus acquisition time trade-off inherent to ULM. Increased local microbubble concentrations not only shorten the scan time, but increase the SNR. In order to overcome the overlapping of the point-spread functions, spatiotemporal filtering algorithms to separate overlapping microbubble signals [166,167] have been introduced. Recently, algorithms based on deep learning (Deep-ULM) have been proposed, offering the advantage of acquiring high resolution images with high microbubble concentrations and lower computation load compared to other techniques. This AI-based approach is capable of learning the nonlinear image domain implications of overlapping point-spread functions originating from populations of closely spaced microbubbles [168]. Finally, tracking of microbubble trajectories, using simple or more complex algorithms [161,169], allows not only for the estimation of super-resolved blood flow velocities [149,160], but for improved image quality due to the fact that a single microbubble can reconstruct several pixels during its trajectory. Indeed, as adequate sampling of microbubble location is critical for the success of tracking algorithms, ultrafast imaging techniques offer a major advantage over conventional imaging approaches. Images are often then reconstructed by projecting the detected tracks on a sub-wavelength grid matrix. True estimates of vessel diameter, therefore, cannot rely on sparse tracks but require them in sufficient number to ensure mapping of the entire lumen, a track density determined by the width of the vessel divided by the super-resolved pixel size [170].

While still in its infancy, ULM has already provided a new *in-vivo* approach to the study of tissue pathology, providing quantitative information on the density, tortuosity, and small modulations of flow patterns within the microvasculature at depth. The first clinical applications of this

technology, using conventional focused beam acquisition, have been conducted on breast cancer [171], lower limb assessment [172] and liver imaging [173]. While there are still limitations to this approach, including slow scan times, SNR, the use of plane-wave scanners not typical in clinics, large amounts of data storage and processing, and motion artefacts, significant advancements in all of these areas are currently ongoing.

1.1.5.5. Microbubble-Therapy Monitoring

It has long been recognized that ultrasound interactions with biological tissue induce bio-effects of both thermal and mechanical origin [174]. On clinical diagnostic scanners, exposure levels are limited in order to avoid these effects [175]. From a therapeutic standpoint, ultrasound-mediated bioeffects have been investigated as a desired endpoint: with effects ranging from tissue ablation [176], microvascular permeability [177], immunomodulation [178], and vascular occlusion [179]. Recent works have highlighted that microbubble contrast agents, under specific acoustic conditions, can generate a wide spectrum of bioeffects [180–182] that contribute towards the treatment of many diseases. Due to their intravascular nature, a primary avenue of research in microbubble-mediated bioeffects is based on the spatially targeted and temporary enhancement of microvascular permeability, employed to promote local drug delivery to regions of disease. One such promising application is the local and transient opening of the blood-brain-barrier [183,184] and blood-spinal cord barrier [185,186] for targeted therapeutics into the central nervous system. This technology has recently entered clinical trials in patients with brain tumors [187–189], Alzheimer's disease [190] and amyotrophic lateral sclerosis (ALS) [191].

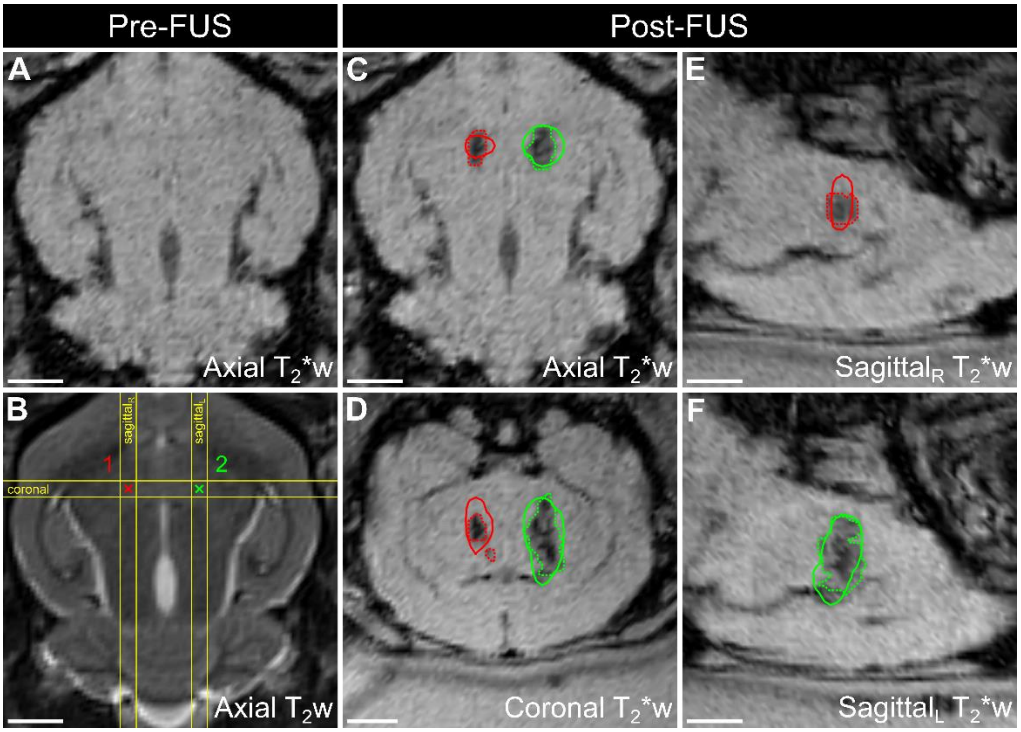

Figure 1.5. Spatial correlation of ultrafast 3D microbubble cavitation with focused ultrasound (FUS) brain tissue damage in a rabbit model. Baseline T_{2^*w} (A) and T_{2w} MRI (B) images pre-sonication depict target locations for two focused ultrasound treatment conditions (labeled 1 and 2). Axial, coronal and sagittal T_{2^*w} MRI images immediately post-sonication (panels C, D, E and F respectively) depict hypointense regions indicative of tissue damage (dotted lines) overlaid by the corresponding spatial microbubble cavitation data (solid lines). The coronal and sagittal slice volumes are indicated in panel B (yellow lines). Scale bar = 5 mm. Figure modified from Jones et al. Theranostics, 2020 [192] **with permission from the authors.**

Despite being met with initial success, widespread clinical adoption of microbubble-based therapeutics will require the continued development of online, real-time imaging strategies to guide and control treatments. While some of these applications employ MRI guidance, there is increasing interest in employing the acoustic scattering from the microbubbles themselves as an indicator of treatment outcome. Since the spectral echo characteristics can be indicative of the underlying microbubble vibrations [193], remote detection of these signals during treatment is

under investigation as a robust and sensitive tool for therapy guidance. Many preclinical applications of targeted microbubble therapeutics, including cardiovascular disease [194,195] and cancer [182], are performed as a dual imaging and therapeutic technique. Contrast enhanced ultrasound is applied and interleaved with a therapeutic pulse from either a separate ultrasound transducer [182] or incorporated by way of clinical [196] or custom-designed sequence. In this way, the presence of microbubbles within the anatomical site of interest can be visually confirmed before, during and after the treatment sequences. The acoustic emissions detected during microbubble-based therapies have been identified as potential markers for treatment outcome in applications including blood-brain barrier disruption [197,198], and targeted therapeutic delivery [199]. To this end, passive cavitation detectors are typically employed to measure raw acoustic data to extract quantitative metrics. Most of these methods to date utilize a single element passive transducer, which does not allow the bubble signal to be localized in space. Ongoing novel engineering of array transducers, combined with passive beamforming algorithms, are currently being designed to spatially map bubble activity and allow for confirmation that elicited bioeffects are localized to the target site [192,200], see Figure 1.5. Above and beyond these correlative measures, efforts are underway to establish control feedback algorithms based on the measured bubble acoustic activity to promote safe levels of vibration and avoid more violent, disruptive bubble behaviour that leads to unwanted damage. These algorithms modulate the acoustic transmit parameters based off the real-time feedback from nonlinear microbubble emissions, including sub-harmonic energy [201,202], harmonic energy [203,204], or both [205].

1.2. Therapeutic Applications of Contrast Agents in Medical Ultrasound

There are many possibilities for exploiting the vibration dynamic of microbubbles for various kinds of therapy; among them are blood-brain barrier opening, sonoporation, drug and gene

delivery, neuromodulation, clot lysis, and cancer therapy. The following are some of the more recent applications that have gained lots of attention, which I will briefly introduce in this section.

1.2.1. Blood-Brain-Barrier Opening

Neurodegenerative diseases include a vast range of conditions, including Alzheimer's disease, Parkinson's disease, amyotrophic lateral sclerosis, and many others [206]. One of the common features observed in the mentioned conditions is functionality loss inside the brain, characterized by the accumulation of misfolded proteins [207]. Clinical treatments for such diseases still need to be improved due to many challenges, one of the most important being the presence of the blood-brain barrier (BBB), which prevents drug distribution inside the brain. BBB is a selective membrane separating the circulatory and central nervous systems CNS. This membrane regulates molecules and ion transfer between blood and the brain, which has a critical role in maintaining the health and stability of the CNS [208]. Studies show that large molecules (larger than 500 Da) do not pass the membrane, and smaller molecules have a 2% chance of passing the barrier [209,210].

Many strategies have been developed to bypass the BBB, such as open surgery for direct injection with surgical risks, intra-arterial injection needing general anesthesia, or modification of targeting ligands, which has a low targeting efficiency [211–216]. The current techniques either have surgical or anesthesia risks or have lower accuracy. Considering the non-invasive, safe, and repeatable nature of ultrasound wave and contrast agents, there is a great interest in utilizing ultrasound contrast agents in BBB opening since its first safe utilization in a rabbit by Hynynen et al. [217].

1.2.1.1. BBB Opening Mechanism and Evaluation Methods

This technique combines focused ultrasound (FUS) and microbubbles (MB). Under specific conditions, an acoustic wave can be made to penetrate the skull; hence, FUS can interact with MBs confined to the vasculature system inside the brain. Even though this technique has shown promising outcomes in recent years, the exact mechanism still needs to be totally understood. Recent literature suggests that the BBB opening results from a combination of effects such as cavitation, sonoporation, and thermal effects [218–220]. The thermal effect is described as an increase in tissue temperature caused by FUS [221], and sonoporation is the transient creation of pores in the cell membrane [181]. Based on recent literature, the process of US-driven reversible BBB opening can last for several hours [218,222], and no significant temperature increase has been recorded. Hence, the BBB opening is mostly caused by the cavitation effect discussed in section 1.1.3.

Recent literature shows that BBB opening happens in low and high mechanical indexes, representing stable and inertial cavitation [218,220,223,224]. In conditions of stable cavitation, the radiation force on MBs will push them toward the vessel wall [89], and the contraction-expansion vibration of MBs causes a push-pull force near the vessel wall. This push-and-pull behavior can open the tight junction in BBB [180], allowing otherwise impermeable molecules to move through. Furthermore, microstreaming caused by MBs induces shear stress on the vessel wall [218,223], which can further disrupt the BBB. Aside from this, in conditions of inertial cavitation, acoustic emission, and micro-jetting can also create a gap in tight junctions.

1.2.1.2. Preclinical Advances of FUS/MBs BBB Opening

1.2.1.2.1 BBB Opening in Alzheimer Disease

Among the neurodegenerative diseases, Alzheimer's disease (AD) is the most prevalent and is the most common cause of dementia. AD is characterized by the over-deposition of β-amyloid and Tau protein in the brain [216,225,226]. Currently, there is no definitive cure for AD, and one of the major challenges in the treatment of this condition is bypassing the BBB, in which FUS with MBs shows promising effects. For example, Dubey et al. increased BBB permeability with the help of MBs in MR-guided FUS therapy to increase the concentrations of intravenous immunoglobulin inside the brain, which is known to reduce β-amyloid protein [227]. In this study, the T1-weighted contrast-enhanced MR image confirmed increased BBB permeability. Applying FUS and MBs with intravenous immunoglobulin decreased the mean surface of β-amyloid plaque by 68% compared to the control. Also, it increased the hippocampal neurogenesis by four times the control group. In another study, Leinenga et al. showed that applying FUS and MBs will increase the aducanumab concentration, an anti-β-amyloid antibody [228]. They measured the concentration of 21.77 ng/ml in the brain lysate as opposed to 4.32 ng/ml with no FUS or MBs. Furthermore, Janowicz et al. conducted a series of measurements comparing the delivery efficiency of different anti-tau antibodies [229]. They showed that all measured antibodies could bypass the BBB when combined with FUS and MBs.

1.2.1.2.2 BBB Opening for Parkinson's Disease

Another prominent neurodegenerative disease is Parkinson's disease, which is characterized by overexpression of α-synuclein and loss of dopaminergic neurons [230,231]. L-dopa is the most common drug used for Parkinson's disease therapy, and it is capable of crossing the BBB [232]. However, it does not stop the ongoing loss of dopaminergic neurons [233], a problem that can be

addressed by neurotrophic factors [234], but these factors cannot easily penetrate the BBB. In a study by Lin et al., the authors used FUS and MBs in conjunction with glia-derived neurotrophic factor, and achieved a 5-10-fold increase in transfection efficiency [235].

1.2.1.2.3 BBB Opening in Primary Brain Tumors

There has been limited success in treating patients with brain cancer, such as glioblastoma (GBM). Even after surgical and chemotherapy treatments, the median survival rate of patients with GBM is 15 months [236]. One of the major causes of high fatality in brain tumors is the presence of the BBB, which prevents the penetration of therapeutic agents. It has been shown in many animal studies that BBB opening using FUS is effective and repeatable, and the effect lasts between 6 and 8 hours. Furthermore, no tissue damage was recorded [217]. These studies show a successful increase in agent uptake, such as Doxorubicin [237] and Trastuzumab [238], after the opening of BBB with FUS and MBs.

Due to the promising results and high mortality rate of patients with brain tumors, the applications of BBB opening using FUS and MBs have been approved for clinical trials in humans. For example, in a clinical study by Mainprize et al. [189], the authors used a transcranial non-invasive device containing 1024 individually driven transducer elements surrounding the skull to sonicate the MBs. They controlled the process with a real MR-guided imaging system. The study was done with five patients with malignant tumors, and the FUS/MBs were used to open BBB to increase the uptake of IV liposomal Doxorubicin, 58 mg, and PO Temozolomide, 160 mg. They showed that the FUS/MBs were successful in opening BBB, and no adverse effect was observed.

1.2.2. Sonoporation, Drug and Gene Delivery

Systemic drug delivery is one of the most common methods of drug delivery, in which drugs rely on the circulatory system to reach the intended location. There are two major limitations in systemic drug delivery: first, drugs circulate the whole body and can affect both healthy and diseased tissue. Second, in some cases, the drug has limited penetration capability and cannot penetrate physiological barriers [189]. Different methods and carriers have been developed to address these issues and facilitate systematic drug delivery [239]. Microbubbles (MBs) combined with ultrasound energy have proven to be a viable option to address these limitations. Ultrasound can penetrate deeper tissue, and MBs only get activated inside the ultrasound field, the location of which is easily controlled; this makes MBs ideal for specificity. The applications of MBs in delivery are not limited to drugs; they can also be used for gene delivery in gene therapy applications. In the previous section, we covered the physical behavior of MBs while activated in the forms of stable and inertial cavitation. It has been shown that physical MB response within an ultrasound field can create pores in the cell membrane in a process called sonoporation, increasing the chance of drug or gene uptake inside the cells [181].

Moreover, aside from the mechanical effect of MBs on cells, they can also be used as drug or gene carriers in a process called functionalizing MBs. Many methods can be used to functionalize MBs. Some drugs can be linked directly to the lipid shell of the MBs [240]. Hydrophilic drugs that cannot attach directly, can be liposome encapsulated and then bind with the outer lipid shell [241]. Furthermore, hydrophobic drugs can bind to the hydrophobic tail of the shell lipids [242] or dissolve within the oil layer in MBs for specific bubbles that have oil [243]. For gene delivery, the first method is to couple liposome-containing genes to MBs' shells, which will be released in the

ultrasound field [244,245]. The second method is to attach negatively charged genes on a positively charged bubble's surface through electrical charge attraction [246–249].

For example, in a study in our lab by He et al. [249], authors used gene delivery by microbubble to promote angiogenesis in human umbilical vein endothelial cells (HUVECs). MicroRNAs (MiRs) are short, non-coding RNAs used by cells to control gene expression; hence, delivering specific MiRs to cells allows for manipulating certain gene expressions. Their capabilities made them an attractive choice in gene therapy for various diseases, including cancer [250–253]. In the mentioned study by He et al. [249], authors developed a new methodology to deliver small amounts of MiR-126 to endothelial cells to promote therapeutic angiogenesis, a promising method to treat cardiovascular diseases such as ischemia. In this study, cationic MBs were created in the lab with in-house formulation, and MiR-126s were attached to bubbles through charge attraction. Finally, a combination of MBs and HUVECs was placed inside a chamber as a suspension and treated with an ultrasound wave. The authors observed that using MBs as gene delivery agents increased the intracellular level of miR-126 by up to 2.3-fold while maintaining cell viability by more than 95%. This methodology has shown that MBs can be used as gene carriers as a viable option for treating ischemic disease.

Furthermore, many other studies show the positive effect of MBs in overcoming physical barriers and increasing drug uptake in tumor tissues. For example, in a study by Snipstad et al. [254] they showed an increase in the delivery of cabazitaxel in breast cancer xenograft due to the application of MBs while not observing any physical damage, resulting in complete remission of the tumor. Similar results were observed in other cancer studies using MBs and FUS to enhance the drug delivery to tumor regions [255–257]. The applications of MBs and FUS in drug and gene delivery

are not limited to the examples mentioned here. Many other studies have shown promising treatment results in different diseases [239,244].

1.3. Numerical Models and Simulation of Ultrasound Contrast Agent Physics

As we covered many current applications of MBs in various medical ultrasound fields and their promising future, it is important to emphasize that their effectiveness is closely tied to their physics and behavior in the ultrasound field, whether it be their strong backscattered pressure, fluid microstreaming in the context of therapeutic applications, or their non-linear behavior in the generation of harmonic and subharmonic response which makes them great blood markers in ultrasound imaging. The dynamic response of MBs depends on many variables, such as the bubbles' characteristics or the local properties of the surrounding environment in which microbubbles are active. Investigation of microbubble vibration physics, either for bubbles in a population or an individual bubble, is of major significance as it provides the knowledge and understanding needed to design and optimize bubble synthesis, pulse sequences, and image interpretation specific to the field and application (our paper, Helfield, Wang, et al. 2018, Goertz 2015).

1.3.1. Physics of bubbles

The most common physical equation to describe bubble vibrations is derived from the conservation of mass and liquid incompressibility. Liquid incompressibility and conservation of mass can be expanded into a mass flux equation, which, combined with the effect of liquid viscosity and surface tension derived from the Young-Laplace equation, can be summarized in an equation widely referred to as the Rayleigh-Plesset equation [258–262]:

$$\rho(R\ddot{R} + \frac{3\dot{R}^2}{2}) = \left(P_0 + \frac{2\sigma_0}{R_0}\right)\left(\frac{R_0}{R}\right)^{3k} - \frac{2\sigma_w}{R} - \frac{4\mu\dot{R}}{R} + P_0 - P(t) \qquad (1.3.1)$$

in which $R, \dot{R}\ and\ \ddot{R}$, are bubble radius, bubble wall velocity and acceleration. $R_0, P_0 and\ \sigma_0$are initial bubble radius, ambient pressure and initial surface tension at gas bubble interface. In equation 1.3.1 μ is fluid viscosity, σ_w is the surface tension and k polytropic coefficient. Equation 1.3.1 is a preliminary equation to model a gas bubble behavior.

Despite its widespread use, this equation has some limitations. For example, it cannot explain some nonlinear and behaviors of MBs, such as compression-only behavior [263]. Another limitation is the assumption that bubbles always remain spherical, known to be untrue under specific acoustic conditions [261]. Perhaps the most notable limitation is the lack of explanation for the viscoelastic shell on MBs. Most commonly used MBs have viscoelastic lipid-monolayer shells, drastically changing surface tensions and bubble reactivity to ultrasound waves. Some studies have incorporated and adjusted some terms of the equation to explain the mentioned behavior [263–265]. One of the most commonly used models in numerical studies of microbubbles is the model proposed by Marmottant et al. [263], which incorporates a viscoelastic shell accounting properties for buckling and rupture. The modified Rayleigh-Plesset equation is written as:

$$\rho\left(R\ddot{R} + \frac{3\dot{R}^2}{2}\right) - P_0 = \left(P_0 + \frac{2\sigma_0}{R_0}\right)\left(\frac{R_0}{R}\right)^{3k}\left(1 - \frac{3\kappa}{c}\dot{R}\right) - \frac{4\mu\dot{R}}{R} - \frac{2\sigma_R}{R} - \frac{4\kappa_S\dot{R}}{R^2} - P(t) \quad (1.3.2)$$

in which σ_R is a dynamic and radially dependant surface tension, c is the speed of the sound in fluid and κ_S is surface dilatational viscosity of the monolayer. Based on this model the term σ_R in equation 1.3.2 further expands into:

$$\sigma(R) = \begin{cases} 0 & if\ R \leq R_b \\ \chi\left(\frac{R^2}{R_b^2} - 1\right) & if\ R_b \leq R < R_r \\ \sigma_{water} & if\ R \geq R_r \end{cases} \quad (1.3.3)$$

In which χ is the shell elasticity, σ_{water} is water's surface tension, $R_b \; and \; R_r$ are "buckling" and "rupturing" radius defined as $R_b = R_0\left({\sigma_0}/{\chi} + 1\right)^{-{1}/{2}}$ and $R_r = R_b\left({\sigma_w}/{\chi} + 1\right)^{{1}/{2}}$.

1.3.2. Finite Element Modeling

The finite element method (FEM) is one of the more popular methods used for solving differential equations [266]. FEM is applied in many fields of engineering, such as fluid dynamics, structure analysis, heat flow analysis, deformation, acoustics, and electromagnetic potential. In FEM modeling, the geometry of the system, either 2D or 3D, is divided into smaller pieces or a finite number of elements. Figure 1.6 depicts an axis-symmetric 2D schematics of a modeling environment in which the study area is the environment around the half-circle. This figure divides the study environment into finite elements by a specific space discretization implemented by constructing a mesh. After dividing the large system into smaller parts, the numerical analyses and the differential equation solving are done on each small part separately, and the solutions are reassembled back into the original system. In the FEM environment, each element is solved independently, yet its boundary condition is affected by and will itself affect other nearby elements.

Using FEM has many advantages, which is the reason that it is being used extensively in engineering and manufacturing [266]. One of the major advantages of using FEM is geometrical adaptability and the ability to show the local effects. Since the elements are solved independently, they can also move. The movement of one element transfers to another, changing the shape and initial conditions of the second, and this effect translates into the whole system, making it possible to study deformities and local pressure, heat, or force effects between 2 elements. Furthermore,

since the system has many independent elements which can move, there is no need for geometrical simplifications.

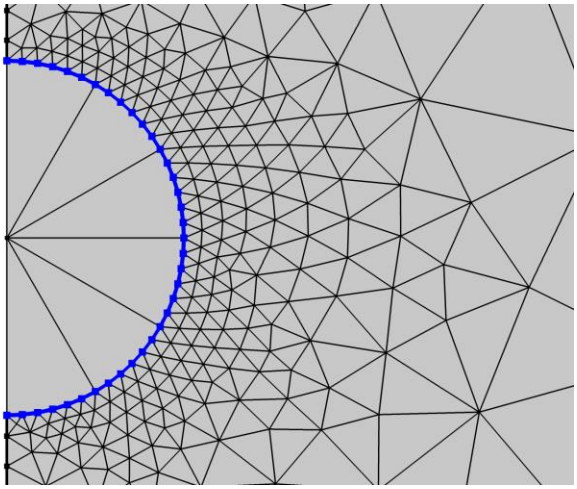

Figure 1.6. FEM model environment with triangle mesh selection

The advantages of FEM in numerical analysis and simulation make it a great tool for studies in fluid dynamics and structural analysis. Hence, I chose this method as the core of this PhD project. It was mentioned in the previous section that one of the limitations of the Rayleigh-Plesset equation is considering the bubble to remain a sphere during its vibration. However, by using FEM, I can allow the bubble to deform, which is closer to real-life behavior. Furthermore, the Rayleigh-Plesset equation defines only bubble behavior and not the effect of boundaries outside the bubble, such as other bubbles or a vessel wall. With FEM, it is possible to incorporate boundaries and external effects on bubbles vibration. For example, in Figure 1.6, Navier-Stokes equations can study fluid pressure, velocity, and stress from the bubble and translate that effect back to the bubble. This coupling between bubble and fluid can be further expanded into systems of two bubbles and vessel walls, and the effect between all these sections will be connected through elements inside the fluid

domain. By using FEM in MB studies, it is possible to create a more realistic scenario to study MBs in an environment closer to the experimental setup.

Furthermore, the bubble is divided into six segments, allowing it to have different initial values on each surface segment at each simulating step. It is worth mentioning that I have tested 12 segments and 24 segments, and the final results were very similar to a six-segmented bubble (maximum of ~2% variation). Considering the small variation, I used a six-segmented bubble to save computation time.

The final output of my model is the change in bubble radius based on time. Since the bubble in our model can deform, but I report a radius versus time, I calculated the radius of the bubble with both methods of surface integration and the average mesh distance from the center, which both yielded similar results, and I chose to use the integration.

1.4. The Model and Objectives of The Thesis

Applications of MBs in medical ultrasound have proven to be very promising, and the field is expanding quickly. My motivation as a Physics student was to study the physical behavior of MBs in conditions close to their experimental and clinical applications to provide some knowledge and understanding needed to optimize MBs further to enhance their effectiveness.

For this PhD project, I used COMSOL Multiphysics® software [5], a FEM-based simulation software. I have created a model and environment based on FEM in which a bubble can be dynamically coupled with its environment through fluid dynamics. Furthermore, I validated the model with existing numerical and experimental results, preparing it to study more realistic scenarios.

Throughout this project, I studied how two individual MBs affect each other's resonance behavior based on different bubble sizes and bubble-bubble distances in various pressure ranges and frequencies. Then, I moved on to study the bubble-bubble effect on harmonic and subharmonic response based on different values of initial phospholipid packing in various pressure and frequency conditions. Finally, in my most recent article, I studied the behavior of MBs vibrating close to each other inside a capillary in bubble-bubble-vessel interaction from both the bubble perspective and vessel perspective. The combination of work done in this project sheds light on some interesting and non-linear MB behavior, which has implications in both imaging and therapeutic applications of MB.

Even though my model provides new insight into bubble vibration dynamics in an environment closer to the experimental setup, it still has some limitations. For example, in my model, the transmitted ultrasound wave is directly applied on the bubble's surface, and there is no acoustic source in this model, which means my model cannot take into account phase differences, delays, and acoustic radiation force. Furthermore, I do not consider blood flow and the presence of other entities in the blood, such as red blood cells, which can slightly alter the response of microbubbles.

Chapter 2. The Influence of Inter-Bubble Spacing on The Resonance Response of Ultrasound Contrast Agent (Manuscript)

This manuscript was published in the Journal of "**Ultrasonics Sonochemistry**" in October 2022

Authors: Hossein (Sohrab) Yusefi[1], Brandon Helfield[1, 2]

[1]Department of Physics, Concordia University, Montreal, Quebec, Canada
[2]Department of Biology, Concordia University, Montreal, Quebec, Canada

2.1. Abstract

Ultrasound-driven microbubbles, typically between 1-8 μm in diameter, are resonant scatterers that are employed as diagnostic contrast agents and emerging as potentiators of targeted therapies. Microbubbles are administered in populations whereby their radial dynamics – key to their effectiveness - are greatly affected by intrinsic (*e.g.* bubble size) and extrinsic (*e.g.* boundaries) factors. In this work, we aim to understand how two neighbouring microbubbles influence each other. We developed a finite element model of a system of two individual phospholipid-encapsulated microbubbles vibrating in proximity to each other to study the effect of inter-bubble distance on microbubble radial resonance response. For the case of two equal-sized and identical bubbles, each bubble exhibits a decrease between 7-10% in the frequency of maximum response (f_{MR}) and an increase in amplitude of maximum response (A_{MR}) by 9-11% as compared to its isolated response in free-space, depending on the bubble size examined. For a system of two unequal-sized microbubbles, the large bubble shows no significant change, however the smaller microbubble shows an increase in f_{MR} by 7-11% and a significant decrease in A_{MR} by 38-52%. Furthermore, in very close proximity the small bubble shows a secondary off-resonance peak at the corresponding f_{MR} of its larger companion microbubble. Our work suggests that frequency-

dependent microbubble response is greatly affected by the presence of another bubble, which has implications in both imaging and therapy applications. Furthermore, our work suggests a mechanism by which nanobubbles show significant off-resonance vibrations in the clinical frequency range, a behaviour that has been observed experimentally but heretofore unexplained.

2.2. Introduction

Small gas-filled microbubbles, typically ranging in size from 1-8 μm and encapsulated with a thin, flexible, and biocompatible stabilizing shell, are currently employed as diagnostic ultrasound contrast agents [13]. Microbubbles vibrate within an ultrasound beam about their equilibrium radius with scattering cross-sections several orders of magnitude larger than a solid size-matched particle [14]. Through resonant oscillations and nonlinear harmonic and subharmonic emissions [262], microbubble signal enables the detection and separation of echoes originating from the blood - to which microbubbles are confined due to their size - from that of the much greater energy of the echoes from the surrounding tissue [267]. This vasculature-specific signal enables the quantification of blood flow and has many applications spanning from detection, diagnosis and therapy monitoring in cardiology and oncology [25,268]. More recently, ultrasound-stimulated microbubbles have been exploited to deliver local and targeted bioeffects under specific acoustic stimulus [269,270]. Microbubble-mediated shear stress and microstreaming are among the mechanisms behind these targeted therapies, including the transient opening of the blood-brain-barrier [217], site-specific drug/gene delivery [181,271,272], vascular shutdown therapy [182] and sono-reperfusion [273].

For both diagnostic and therapeutic techniques, an understanding of ultrasound-driven microbubble dynamics is critical to ensure robust and repeatable application. As has been

previously well documented, microbubble behaviour is a function of both its intrinsic features [64,262,274,275] (*e.g.* bubble size, shell properties) and extrinsic environmental factors [64,276–279]– including fluid viscosity, fluid temperature, local boundaries and the presence of neighboring microbubbles. Indeed, there have been many mechanistic studies investigating the physics of vibrating microbubbles to elucidate the role of these factors on bubble behaviour as it relates to its imaging and therapeutic potential, the majority of which are performed on an individual microbubble [275,277,280–283]. These investigations have explored unique physical and biophysical phenomena on an individual bubble scale, resulting in new insights towards contrast imaging [61,65] and ultrasound-mediated cellular therapies [284–286].

While it is a challenge to estimate local concentrations of contrast agent *in-vivo*, microbubbles may not be in isolation when used diagnostically or as a therapeutic agent. Order of magnitude estimates result in clinical agent doses (~1:5000 dilution) possessing an average inter-bubble spacing of 80 μm, which can decrease due to *i)* acoustic radiation forces [89], *ii)* ultrasound-induced bubble coalescence [287] and *iii)* complex fluid flow patterns [288]. Furthermore, smaller ultrasound-sensitive agents are currently being investigated for both diagnostic and therapeutic application, including phase-shift nanodroplets that can acoustically vaporized into *in-situ* microbubbles [99], and stabilized nanobubbles – encapsulated bubbles on the order of several hundreds of nanometers in radius [112,289]. Assuming a volume-limited dose similar to clinically used micron-sized bubbles, a decrease in size by a factor of 10 translates to a 1000-fold increase in local bubble density [100].

To begin to address this, there are limited studies exploring the physics of bubble clusters, generally performed using analytical modifications of a second-order ODE describing bubble wall motion (*e.g.* Rayleigh-Plesset-type equations [290]). The majority of these studies focus either on

bubbles without a material encapsulation or do not take into account any of the fluid dynamic considerations of the surrounding fluid [291,292]. In this study, we propose to study effect of bubble proximity in a system of two encapsulated microbubble contrast agents using a finite element approach to ensure the two-way coupling between bubble vibrations and the local fluid environment. Specifically, we examine the coupling between different microbubble sizes and inter-bubble spacings with a view towards the resonance response of the system, as it is one of key features that make microbubbles an ideal ultrasound agent for imaging and therapy.

2.3. Mathematical Model

2.3.1. Fluid Domain

In the present study, the radial oscillations of two individual microbubbles in free space are considered, situated a distance h apart - see Figure 2.1. The fluid domain surrounding the microbubbles is modeled as a Newtonian fluid. Given that the acoustic wavelength is much larger than the microbubble size and that the fluid velocity is much slower than the speed of sound, the fluid was further assumed to be incompressible [261]. Under these circumstances, the fluid motion is modeled by the Navier-Stokes equations, given below:

$$\nabla . \vec{v} = 0 \tag{2.1}$$

$$\rho \left(\frac{\delta v}{\delta t} + v . \nabla v \right) = -\nabla p + \mu \nabla^2 v \tag{2.2}$$

where v is the fluid velocity, ρ is the fluid density, μ is the dynamic viscosity of the fluid and p is the fluid pressure.

2.3.2. Microbubble Dynamics

The gas inside each microbubble is assumed to be spatially uniform and is modeled as an ideal gas via a polytropic process [261]. The pressure difference across the bubble wall P_B, is a result of the combined affects of surface tension, the surrounding fluid viscosity, and the pressure contributions from the viscoelastic encapsulation, and is given as follows:

$$P_B = \left(p_0 + \frac{2\sigma_0}{R_0}\right)\left(\frac{R_0}{R}\right)^{3k}\left(1 - \frac{3\kappa}{c}\dot{R}\right) + P_v - \frac{4\mu\dot{R}}{R} - P_{elas} - P_{visc} - P(t) \tag{2.3}$$

where p_0 is the ambient pressure, σ_0 is the initial surface tension at the gas-liquid interface, k is the polytropic index, P_v is the vapour pressure which is considered negligible compared to the gas pressure ($P_v = 0$), R and $\dot{R}$ represent the bubble radius and wall velocity, respectively, P_{visc} and P_{elas} are the pressure contributions due to the viscosity and elasticity of the shell, respectively, and $P(t)$ is the externally applied acoustic pressure at the bubble wall. Multiple models have been proposed to explain the behaviour of microbubbles characterized by a thin viscoelastic shell by incorporating elastic and viscous terms [35,262,293]. Perhaps the most successful nonlinear bubble models to date incorporate phospholipid monolayer dynamics – indeed, experimental lipid research highlights that the surface tension of a lipid monolayer, such as those commonly employed in contrast microbubble synthesis, decreases with increasing compression rate (*i.e.* decreasing intermolecular area) [294]. Incorporation of this physics into simplistic Rayleigh-Plesset type bubble models [263,295] have been shown to predict unique microbubble vibrational signatures that have been observed experimentally, including 'compression only' behaviour [65,296]. Given this, we chose to implement an encapsulation model that considers a radially-

dependent surface tension, as manifested through the elastic pressure contribution $P_{elas} = {2\sigma(R)}/{R}$, with the radially dependent surface tension $\sigma(R)$ given as:

$$\sigma(R) = \begin{cases} 0 \; if \; R \leq R_b \\ \chi\left(\frac{R^2}{R_b^2} - 1\right) if \; R_b \leq R < R_r \\ \sigma_{water} \; if \; R \geq R_r \end{cases} \tag{2.4}$$

where χ is the shell elasticity, and $R_b = R_0\left({\sigma_0}/{\chi} + 1\right)^{-1/2}$ and $R_r = R_b\left({\sigma_w}/{\chi} + 1\right)^{1/2}$ are defined as the 'buckling' and 'rupturing' radius, respectively, with R_0 as the equilibrium radius of the microbubble. These are the radial limits within which the shell contribution dictates a quadratic-dependence on radius [263]. Indeed, Eq. 2.4 models the repartitioning of phospholipid molecules as it is manifested through the alterations in surface tension. Further, we consider the viscous contribution as $P_{visc} = {4\kappa_S \dot{R}}/{R^2}$ with κ_S defined as the surface dilatational viscosity of the monolayer [262]. Note that the compressibility term proportional to ${\dot{R}}/{c}$ in Eq. (2.3), which was added despite our assumption of an incompressible fluid, does not play a large role in our simulation results (as $\dot{R} \ll c$). It was however incorporated for validation purposes against well-known models (see below). Further, note that Eq. (2.4) was originally derived from surface area arguments, however, was incorporated into the current study in the form presented – as has been done previously [297].

2.3.3. Model Description and Method of Solution

The boundary conditions imposed along each bubble free surface are such that the velocity and pressure across the boundary remain continuous, namely:

$$v(R) = \dot{R} \tag{2.5a}$$

$$p(R) = P_B \tag{2.5b}$$

where P_B, the pressure at the bubble wall, is given by Eq. (2.3). Note here that we are imposing a no-slip velocity condition and negligible shear stress in the tangential direction along this interface. In this manner, these conditions exert two-way coupling between the bubble wall motion and the surrounding fluid. In order to allow the slight perturbations deviating from spherical oscillations

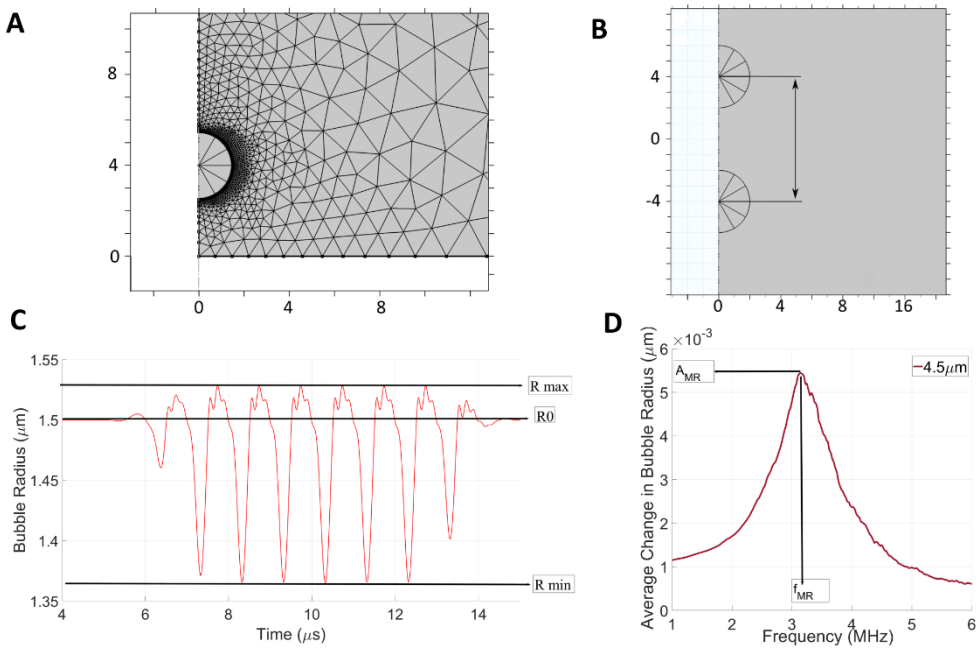

Figure 2.1. Finite-element model environment and data analysis description. A) A representative example of the mesh grid placement on an individual bubble, where the bubble is divided into 6 sections to allow for spatially dependent application of Eq. (3). Simulations were performed using an axisymmetric environment. Units are in micrometers. B) Schematic view of the two-microbubble system; h denotes the center-to-center distance between the two microbubbles. Units are in micrometers. C) A sample plot of a radial response of a microbubble at a given transmit frequency. Both the maximum R_max and the minimum R_min radius were used to calculate the radial excursion. D) The frequency of maximum response (f_MR) and amplitude of maximum response (A_MR) of an individual microbubble.

to influence the fluid domain, each bubble free surface was divided into 6 different sections (Fig. 2.1), in which each section is subjected to the local boundary conditions given above. This allows the local curvature, approximated as spherical and spatially averaged over 1/6 of the microbubble, to contribute to the neighboring fluid motion. Pilot studies using 12 segments did not yield significantly different results. The final microbubble dynamic curve calculated in our model is derived from the average of the radius changes from the different sections of a given microbubble.

The governing equations subject to the above boundary conditions, along with the boundary conditions of constant p_0 along the edges of the simulation domain, were solved computationally using the finite-element method (FEM) with COMSOL Multiphysics 5.8 (COMSOL AB. Burlington, MA). Figure 2.1B illustrates the geometry of the model and Figure 2.1A is a sample of the mesh grid in our FEM simulation for an individual bubble. Due to the symmetry of the two microbubbles and the computational domain, only half of the simulation space was calculated in an axisymmetric environment to minimize the computational time. The mesh size was selected to be 8-20 times smaller than the smallest bubble radius. This results in a mesh size that is much smaller than the wavelength of the acoustic wave. Further, the mesh density was much higher in the neighborhood of the microbubble wall in order to capture the salient physics of interest, and decreased further from the bubbles, where we do not expect any significant effects. The moving microbubble free surface was described using a moving mesh arbitrary Lagrangian-Eulerian (ALE) algorithm. This allows for the computational mesh to move arbitrarily to optimize the shape of the elements and for the mesh nodes to track the moving boundary. The microbubbles are considered to be inside the focal volume of a conventional ultrasound transducer. Based of the size of a typical focal volume (~mm^3) and the size of contrast agent microbubbles (~μm), the microbubbles were considered to be inside a uniform domain of ultrasound energy. This energy

contribution enters our model as a change in acoustic pressure on the microbubble surface ($P(\mathrm{t})$ in equation 2.3). The transmit pressure employed was a Tukey windowed (tapered cosine) 10 cycle pulse at a sampling frequency of 500 MHz. The other parameters in this study were held constant; $\rho = 1000\, kg/m^3$, $k = 1.095$, $\mu = 0.001\, Pa.s$, $\chi = 1\ N/m$, $\kappa_S = 1.5 * 10^{-9}\ kg/s$, $\sigma_{\mathrm{w}} = 0.072\ N/m$ and $\sigma_0 = 0.01\ N/m$. We acknowledge that recent work has demonstrated transmit frequency/bubble size dependent shell properties [36,62]. Given that the current study explores many transmit frequency and bubble size combinations, the shell parameters adopted here were chosen to lay well within the range of previous experimental reports on phospholipid-encapsulated contrast agent microbubbles.

To study the effect of frequency-dependent microbubble vibration, we performed our simulations using individual tone bursts with a transmit frequency ranging from 1-8 MHz in increments of $df = 25$ kHz. The microbubble diameter ($d = 2R_0$) range investigated in this study spanned from $0.5 \leq d \leq 4$ μm to cover both nanobubble and traditional microbubble size ranges [36], with a bubble center-to-center distance varying from 2-32 μm and peak-negative pressure ranging from 1-120 kPa. The parameter range here was selected due to its relevance in clinical imaging and therapeutic studies.

2.3.4. Analysis of Radial Oscillations

For a given microbubble radial profile, the radial excursion was calculated based on the average of R_{max} and R_{min} over the 6 regions of the microbubble, which represent the maximum and minimum dynamic radius, respectively (Fig. 2.1C). To study frequency-dependent microbubble vibrations, the radial excursion was calculated for each bubble at each transmit frequency to generate a resonance curve. The metrics extracted from this curve, as shown in Fig. 2.1D, were

the amplitude of maximum response (A_{MR}) and the frequency of maximum response (f_{MR}). Indeed, f_{MR} represents the frequency at which the damped radial oscillations are maximal (*i.e.* the resonance frequency of the nonlinear damped microbubble system) – not to be confused with other closely related 'resonance' frequencies, including the frequency at which maximal scattered pressure or scattering cross-sections are observed [36,298].

2.3.5. Validation

We employed four different metrics to validate our numerical model. Firstly, our model was validated in the limit of a single microbubble in free fluid under low acoustic pressures and compared to the well-known analytical Rayleigh-Plesset equation (RPE) under the same acoustic conditions [261,263]. Figure 2.2A shows the radial oscillation profile for a microbubble ($R_0 =$ 1.5 μm) driven at $f =$1 MHz at 45 kPa. The graphs show that the result of our simulation (solid; red) and the RPE (dashed; black) are in excellent agreement with an average percent error of 0.3%. A second validation (Fig. 2.2B) was performed by assessing the resonance response of an individual

microbubble as a function of acoustic pressure from 10-30 kPa. Our simulation generates the expected strain-softening behaviour of decreasing resonance frequency with increasing pressure and a skewing of the resonance curve – as has been observed both experimentally [62,299] and through numerical modeling [300]. Thirdly, under low-amplitude driving conditions (~1 kPa) where the bubble experiences small deviations about its equilibrium radius, all bubble models reduce to a similar expression for the size-dependent resonance frequency [301]. In this limit, our model results over the range of $2.5 \leq d \leq 5$ μm (red dots in Fig. 2.1C) show excellent agreement with an average percent error of 3.8% as compared to the well-known equation. Finally, the fourth

validation was conducted by simulating an individual microbubble adjacent to a rigid wall. Indeed, by modifying the RPE via a 'method-of-images' approach [261], it can be shown that the f_{MR} of an individual microbubble decreases by a factor of $\approx \sqrt{2/3}$ and its A_{MR} increases by a factor of $\approx \sqrt{3/2}$ as it moves in direct contact with the rigid wall ($h = R_0$). We ran our simulation for a $d = 3\mu m$ microbubble situated at varying distances from such a rigid wall under a transmit pressure of 30 kPa. The results of this model validation are shown in Fig. 2.2D, resulting in a shift of f_{MR} and A_{MR} of ~13% and ~10% respectively in the expected direction, as the bubble sits at $h = 4\ \mu$m

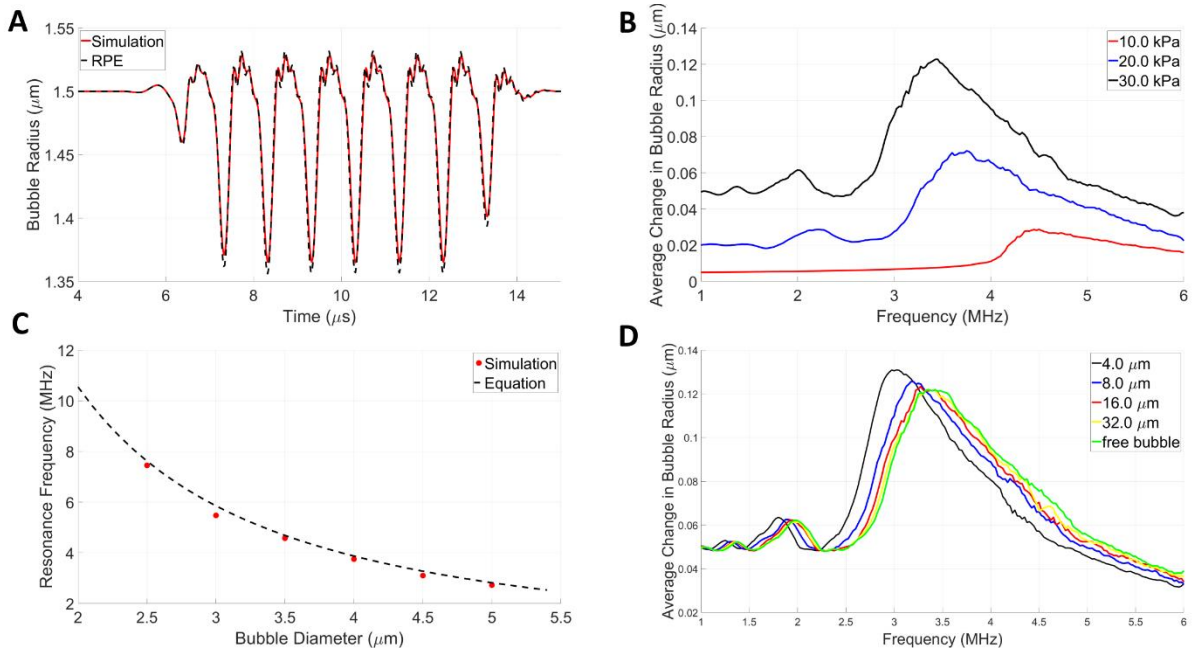

Figure 2.2. Validation of our finite-element model using four different metrics. A) The radial response of a microbubble driven at $f = 1$ MHz at 45 kPa. Our model (solid red) is in excellent agreement with the well-known Rayleigh-Plesset type equation (dashed black). B) The resonance response of a microbubble at different driving pressures. The negative skewing of the resonance curve and the decreasing f_{MR} with increasing pressure is expected. C) The linear resonance frequency at a transmit pressure of 5 kPa versus microbubble size (red dots are results of our model and dashed line is result of the well-known resonance frequency equation)

D) The resonance response of an individual microbubble adjacent to a purely rigid wall. The direction and magnitude of the shift in f_{MR} and A_{MR} is consistent with the 'method-of-images' analysis.

from the rigid wall. While we note that the 'method-of-images' does not capture the complex fluid dynamics at the boundary and may not strictly serve as a validating tool, it has been employed in more simplistic microbubble modeling scenarios [302]. Indeed, as a rigid wall is not a biologically relevant boundary, we did not explore this arrangement any further.

2.4. Results

We examine the frequency-dependent response of a two-microbubble system in three different scenarios: *i)* the effect of the presence of an identical, size-matched microbubble, *ii)* the effect of the presence of a nearby smaller microbubble, and *iii)* the effect of the presence of a nearby larger microbubble. In all scenarios, the frequency-dependent radial resonance response is investigated for varying inter-bubble distances h, and the response for the individual microbubble in free-space (*i.e.* in isolation) is shown for comparison in green to better appreciate the contributions due to the second microbubble.

2.4.1. Two Identical, Size-matched Microbubbles

Figure 2.3 shows the result of a simulation in a system of two identical microbubbles ($d_1 = d_2$) with diameters of 2, 3, and 4 μm. Microbubbles were subjected to a series of tone bursts at a constant peak-negative pressure of 30 kPa and simulated with center-to-center distances of h=8, 16 and 24 μm. In all examined scenarios, the results show that when a given microbubble approaches another microbubble of the same size, each bubble experiences a decrease in f_{MR} and an increase in A_{MR}. Further, the extent of this effect amplifies as the microbubbles get closer to each other, with the maximal effect shown here at $h = 8\,\mu m$. Taking into account all sizes

investigated here, the maximum amount of the shift from two closely-positioned microbubbles at $h = 8\ \mu m$ apart as compared to its response in free space is a decrease in f_{MR} ranging from 7-10% and an increase in A_{MR} from 9-11%. Note here the small secondary peaks due to harmonic coupling (*e.g.* 3-4 MHz for $d = 2\ \mu$m in Fig. 2.3A) also exhibit the same trend as the primary resonance peaks; albeit at a lower amplitude. Indeed, the presence of these harmonic peaks is a well-known and established feature of resonant bubble systems [63,300,303].

2.4.2. A microbubble in the Presence of a Smaller Microbubble

In the following two subsections, we examine the results of two unequal sized microbubbles ($d_1 \neq d_2$). Figure 2.4 highlights the resonance curves for the larger microbubble d_1. The following four combinations were examined: a $d_1 = 2$ µm bubble in close proximity to a $d_2 = 0.5$ µm bubble

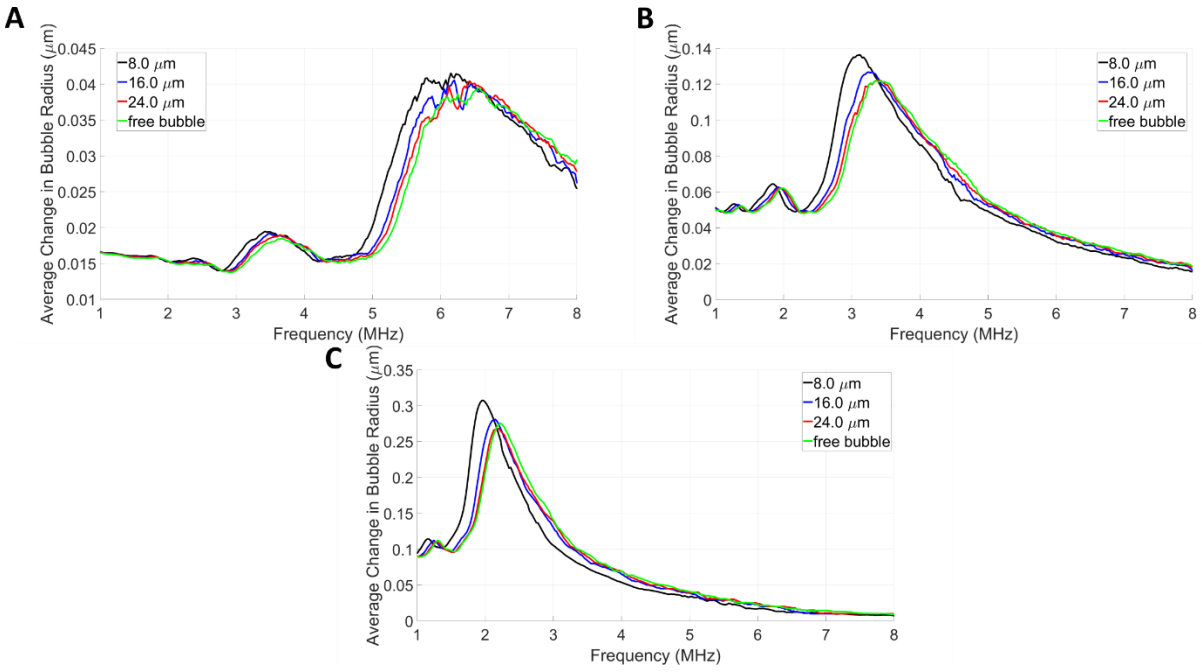

Figure 2.3. The resonance response of each microbubble within a two-microbubble system of equal sized bubbles shifts towards lower f_{MR} and higher A_{MR} as the bubbles approach each other. A) $d_1 = d_2 = 2\ \mu$m B) A) $d_1 = d_2 = 3\ \mu$m; C) A) $d_1 = d_2 = 4\ \mu$m. Note that each of these two bubble-systems was insonicated at 30

kPa and show the same general trend. Individual resonance response in free-space (green curve) is shown for comparison. Note the presence of second-harmonic coupling, and that these secondary peaks follow the same trend as the primary resonance peaks.

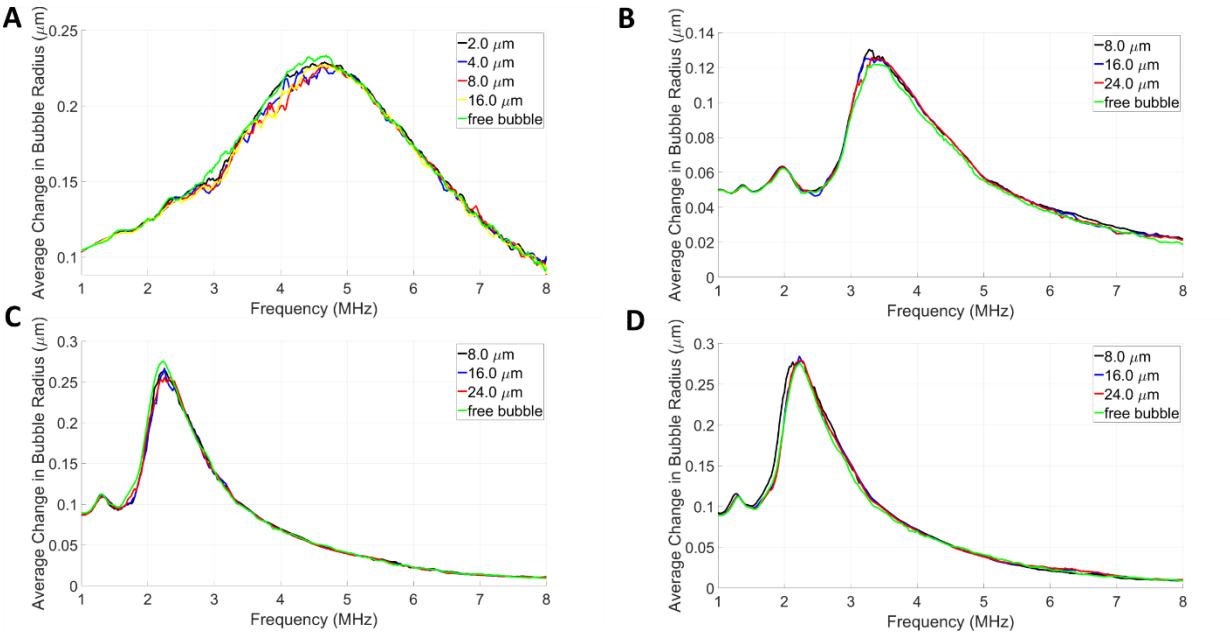

Figure 2.4. A small microbubble exerts no influence on the resonance characteristics of a larger microbubble. The response responses of the larger microbubble d_1 in the following situations: A) $d_1 = 2\ \mu m$; $d_2 = 0.5\ \mu$m; B) $d_1 = 3\ \mu m$; $d_2 = 2\ \mu$m; C) $d_1 = 4\ \mu m$; $d_2 = 2\ \mu$m; D) $d_1 = 4\ \mu m$; $d_2 = 3\ \mu$m. Panel A was insonicated at 120 kPa; all others at 30 kPa. Individual resonance response in free-space (green curve) is shown for comparison.

(Fig. 2.4A), a $d_1 = 3$ μm bubble in close proximity to a $d_2 = 2$ μm bubble (Fig. 2.4B), a $d_1 = 4$ μm bubble in close proximity to a $d_2 = 2$ μm bubble (Fig. 2.4C), and $d_1 = 4$ μm bubble in close proximity to a $d_2 = 3$ μm bubble (Fig. 2.4D). For the system depicted in Fig. 2.4A, the microbubbles were insonicated at 120 kPa, and all others were insonicated at 30 kPa. We simulated the system with center-to-center distances of 2, 4, 8, 16 and 24 μm. The results presented here

indicate that, for all combinations examined, the presence of the smaller microbubble d_2 has negligible influence on the vibration physics of the larger microbubble d_1. Within the frequency resolution employed here, there is no change in f_{MR} and only a slight shift towards lower A_{MR} (2-3%) as compared to its free, isolated response.

2.4.3. A microbubble in The Presence of a Bigger Microbubble

As opposed to the results shown in Fig. 2.4, there is a significant effect on the smaller microbubble d_2 due to the presence of a neighboring larger microbubble d_1. Figure 2.5 shows the results of the following bubble size combinations: a $d_2 = 0.5$ μm bubble in close proximity to a $d_1 = 2$ μm bubble (Fig. 2.5A), a $d_2 = 2$ μm bubble in close proximity to a $d_1 = 3$ μm bubble (Fig. 2.5B), a $d_2 = 2$ μm bubble in close proximity to a $d_1 = 4$ μm bubble (Fig. 2.5C), and $d_2 = 3$ μm bubble in close proximity to a $d_1 = 4$ μm bubble (Fig. 2.5D). As in the scenario above, the results in panel Fig. 2.5A were simulated at 120 kPa, while the others were insonicated at 30 kPa. We simulated the system with center-to-center distances of h =2, 4, 8, 16 and 24 μm. The influence of the larger bubble is most strongly felt as the two bubbles approach each other. For all combinations of microbubble sizes examined here, the results consistently indicate that the smaller microbubble of size d_2 exhibits a strong and significant increase in f_{MR} ranging from 7-11%, and a decrease in A_{MR} ranging from 38-52% as compared to its isolated response. In looking at Fig. 2.5B, for example, the isolated, free f_{MR} of a d_2 =2 μm microbubble (green curve) at the simulated pressure is approximately 6.5 MHz. In either the presence of a neighboring $d_1 = 3\mu m$ (Fig. 2.5B) or $d_1 = 4\mu m$ (Fig. 2.5C) microbubble, this peak exhibits a drastic decrease in amplitude and shift to higher frequency ($\approx$ 7 MHz in panel C). Note that the primary resonance of the $d_2 = 0.5\ \mu m$ microbubble

(*i.e.* a nanobubble) is well out of the range of examined frequencies (> 8 MHz) and is thus not visible in Fig. 2.5A.

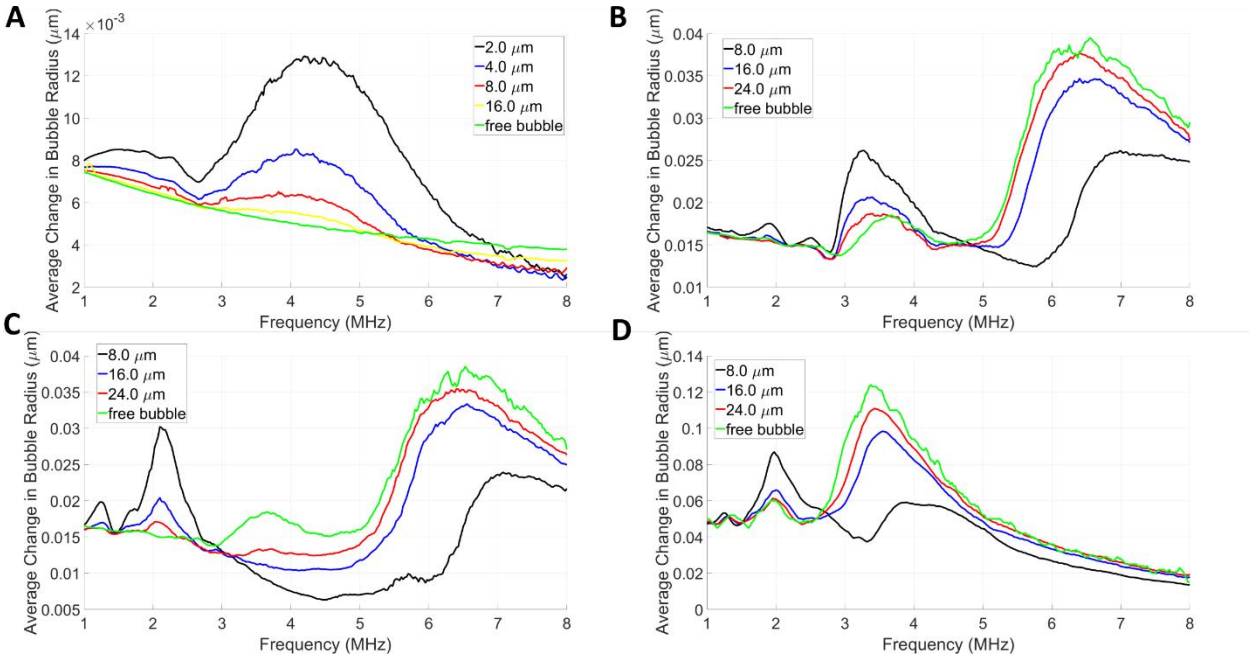

Figure 2.5. A large microbubble exerts significant influence on the resonance characteristics of a nearby smaller microbubble. The response responses of the smaller microbubble d_2 in the following situations: A) $d_1 = 2\ \mu m$; $d_2 = 0.5\ \mu$m; B) $d_1 = 3\ \mu m$; $d_2 = 2\ \mu$m; C) $d_1 = 4\ \mu m$; $d_2 = 2\ \mu$m; D) $d_1 = 4\ \mu m$; $d_2 = 3\ \mu$m. Panel A was insonicated at 120 kPa; all others at 30 kPa. Individual resonance response in free-space (green curve) is shown for comparison. The primary resonance peak shifts to higher f_{MR} and lower A_{MR} as the inter-bubble spacing h decreases. The primary resonance peak of the $d_2 = 0.5\ \mu$m nanobubble is not visible in panel A. Note the secondary, off-resonant peak occurring at the f_{MR} of the larger microbubble. This strong off-resonant nonlinear coupling occurs for all bubble combinations investigated. See text for details.

Another glaring and significant result stemming from the influence of a larger microbubble is the presence of a secondary, off-resonance peak that is distinct from the harmonic peak. Indeed, this secondary peak in the frequency-dependent response exhibited by the smaller bubble d_2, observed

in all combinations of bubbles examined here, corresponds precisely to the f_{MR} of the large microbubble d_1 and thus represents a nonlinear coupling between the two bubbles. As previously stated, while the primary resonance response from the nanobubble is not depicted, the off-resonance peak due to the neighboring $d_1 = 2\ \mu m$ is clear, with its influence becoming stronger as the bubbles approach each other (Fig. 2.5A). The appearance of this peak, which is maximum at $h = 2\ \mu m$, appears precisely at a frequency of 4.5 MHz, in excellent agreement with the f_{MR} of the $d_1 = 2\ \mu m$ microbubble shown in Fig. 2.4A. This is also readily observed in the other three panels as the inter-bubble spacing is decreased, with the f_{MR} of the larger bubble ($d_1 = 3\ \mu m$ in panel B; $d_1 = 4\ \mu m$ in panel C&D) corresponding to 3.5 MHz and 2.1 MHz, respectively. Indeed, the final two panels highlight that this peak derived from the off-resonance nonlinear coupling of the larger bubble vibrations is distinct from the harmonic peak – a peak observed even in isolated, individual bubbles (see Fig 2.2A for example). While these peaks overlap in Fig. 2.5D due to the specific sizes of the microbubble pair, they are clearly separated in Fig. 2.5C ($d_2 = 2\ \mu$m), where the harmonic peak expectedly shifts up due to the decreasing size of d_2 in Fig. 2.5C versus that of Fig. 2.5D; whereas the off-resonance peak at 2.1 MHz remains consistent between these two scenarios since the larger microbubble size is constant between these two panels ($d_1 = 4\ \mu$m). Further, this nonlinear coupling effect can result in a large magnitude effect that rivals or even exceeds the A_{MR} of the primary resonance peak (*e.g.* Fig. 2.5C, black curve). Finally, Fig. 2.6 highlights the influence of a larger neighboring microbubble on bubble response with a particular emphasis on the transmit frequency (the panels represent the same two-bubble system as those

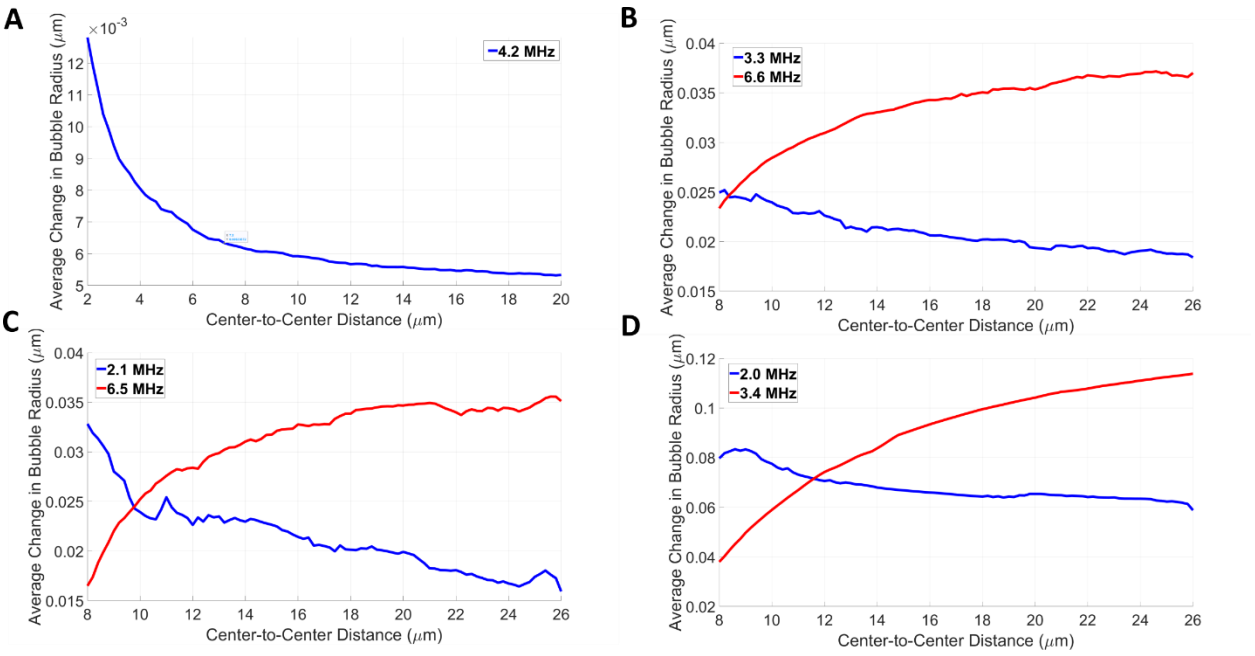

Figure 2.6. The direction and magnitude of the proximity effect is highly dependent on the transmit frequency (i.e. clinical application) of interest. The panels correspond to the same two-microbubble systems as described in Fig. 2.5. The red curves denote a transmit frequency near the primary resonance response, while the blue curve denotes a frequency near the off-resonance peak corresponding to the f_{MR} of the larger microbubble.

described in Fig. 2.5). Indeed, clinical applications of ultrasound are conducted at a fixed transmit center frequency, varying from the lower end of the MHz range for deep targets (*e.g.* 1-2 MHz for abdominal imaging), to mid-range for more superficial parts (*e.g.* 6-10 MHz for breast imaging, carotid imaging) [304]. While clinical pulses are shorter in length (and thus more broadband) than the pulses employed here, it is still apparent that depending on the clinical application, the direction and magnitude of the influence exerted by the two-bubble system shifts as the inter-bubble spacing decreases. The fixed frequencies here are chosen to align with the main (*e.g.* primary) and off-resonance coupling peaks.

2.5. Discussion

The results presented here indicate that the presence of a neighboring microbubble influences the radial resonance response of an individual microbubble. We note here that a subset of studies performed on 'clean', unencapsulated microbubbles yield similar relationships regarding $f_{MR}$and A_{MR}. This phenomenon plays a role not only in ascertaining the resonance response of these bubbles in clinically relevant doses, but also in the application dependent (*i.e.* transmit frequency-dependent) response of a system of bubbles. Specifically, the magnitude and direction of the shift in response due to bubble proximity is a strong function of the transmit frequency, a direct result of the changes in f_{MR} and A_{MR}. For the simplest and idealized case of two equal sized bubbles, the frequency of maximum response for both of them shifts to lower frequencies while the amplitude of maximum response increases. This type of behaviour is similar to the effect of a rigid wall (*i.e.* non-biologically relevant) on the response of a single microbubble – which generates the same potential flow as two symmetrically positioned microbubbles oscillating in phase - shown theoretically using the method of images [305–307].

Of perhaps more interest is the situation of unequal microbubble sizes. In this type of two-bubble system, the smaller sized microbubble exhibits a strong shift towards higher f_{MR} and a drastic decrease in A_{MR} – in stark contrast to the equal-sized bubble scenario described above. Further, when the two bubbles are in very close proximity, the smaller microbubble exhibits a strong off-resonance response that corresponds to the resonance frequency of its larger companion microbubble, while this larger microbubble exhibits no detectable change in its radial response – neither f_{MR} nor A_{MR}. These effects are shown specifically in Fig. 2.6 which is the result of a fixed frequency simulation for the condition of Fig. 2.5. Indeed, only small differences in bubble sizes are required for this drastic change in overall response. As shown in Figs. 2.5 and 2.6, only the

relatively small difference in bubble diameter of 0.5 μm is required to switch the observed effects demonstrated for a two-bubble system of two equal sized bubbles to that of unequal sized bubbles. This is especially of interest when considering practical application of contrast microbubbles. Clinically and commercially available microbubbles (*e.g.* Definity, SonoVue) are characterized by polydisperse microbubble populations (*e.g.* [36,43]). While there is ongoing research on the design of monodisperse microbubble formulations with a view to improving contrast image sensitivity, these are still characterized by typical coefficient of variations on the order of 5% [308,309] which results in an increased likelihood of the situation presented in Figs 2.5,2.6: unequal sized microbubbles. The phenomenon observed here also sheds insight into the recent development and characterization of sub-micron bubbles (*i.e.* nanobubbles). Indeed, while possessing resonance frequencies much larger than the clinical frequency range on account of their small size (linear estimates beyond f=30 MHz [100]), robust acoustic measurements have recently provided evidence of nonlinear scattering [113,115], contrast imaging, and therapeutic potentiation [117] from nanobubble populations within clinical and pre-clinical ultrasound frequency ranges. The results presented here, specifically for the nanobubble dataset ($d = 0.5\ \mu$m), suggest a possible mechanism for this off-resonance behaviour, namely strong acoustic coupling from a neighboring micron-sized bubble (Fig 2.5.A,2.6.A). The 'contaminating' microbubble need not be an artefact of bubble synthesis but can also be due to ultrasound-induced bubble coalescence within typical imaging and therapeutic pulsing schemes. In this scenario, numerous off-resonant driven nanobubbles in addition to neighboring resonant microbubbles would contribute to the observed echo at clinical frequencies. Indeed, for ultrasound therapeutics, it is the oscillation amplitude examined here that is relevant as they can be linked to sonoporation and other bioeffects (*e.g.* [181]). In fact, there are many current investigations into nanobubble-based therapeutics

[100,112,116]. However, for imaging purposes, we can estimate the far-field scattered pressure P_s at a distance r via the following relation [261]:

$$P_s \approx \rho\left(\frac{\ddot{R}R^2 + 2R\dot{R}^2}{r}\right) \tag{2.6a}$$

where under low driving conditions, the maximum pressure reduces to

$$P_s \approx \rho\left(\frac{\omega^2 R_0^3 \epsilon}{r}\right) \tag{2.6b}$$

where ω is the angular frequency and ϵ is the radial excursion. From the above equation, for a fixed frequency and bubble size (as is the case in Fig. 2.5a), the maximum scattered pressure scales proportionally to the radial excursion, and thus we expect a similar increase between a nanobubble in free-space (green curve in Fig. 2.5a) and a nanobubble close to a microbubble (black curve in Fig. 2.5b).

It is insightful here to place our numerical, finite-element model within the framework of the very limited experimental data investigating the influence of a neighboring microbubble and/or a planar boundary on the radial response of an individual ultrasound contrast agent. In perhaps the only dataset to be directly comparable to our model, Garbin et al.[279] measured the influence of a bigger microbubble ($d_1 = 4.8\,\mu$m) on the radial dynamics of a smaller one ($d_2 = 4.5\,\mu$m) by employing a combination of optical trapping and ultrafast full-frame microscopy [310]. In this single frequency ($f = 2.25$ MHz), 8-cycle acquisition, the vibrational response of the smaller bubble d_2 was significantly lower when placed $h = 8\,\mu$m away from the larger bubble as compared to its free, isolated response (Fig 3B in Garbin et al. [279]). Our simulated result within this system consistent with the measured data, with the presence of the larger bubble resulting in

a 2% decrease in maximum radius R_{max} and an 8% decrease in minimum radius R_{min} as compared to its free response (Fig. 2.7). While this does not directly provide conclusive evidence of the bubble-proximity based f_{MR} and A_{MR} shifts observed in the present manuscript – since no such experiment has even been conducted – it is consistent at this individual transmit frequency. Further, while the individual shell parameters for Garbin et al.'s data were not known, our simulation predicts a similar trend over a wide range of lipid shell parameter estimates.

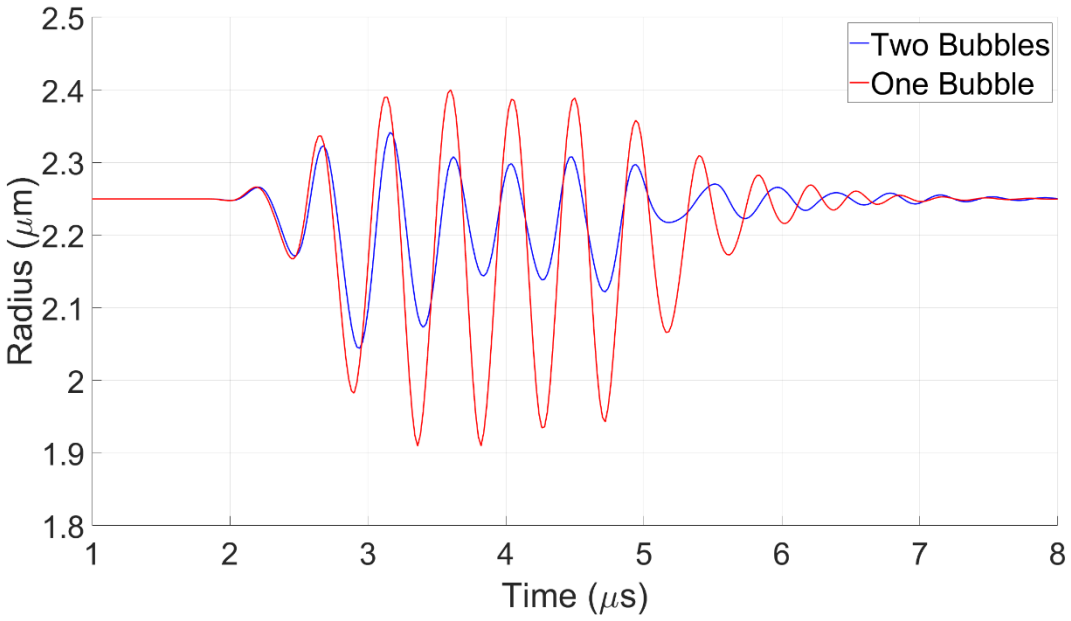

Figure 2.7. Simulation results are consistent with only known experimental data of a similar system. The radius versus time of an individual $d_2 = 4.5\ \mu m$ simulated (red) in free space and (blue) in the proximity of a larger bubble ($d_1 = 4.8\ \mu m$) situated h=12.5 μm away, insonicated at f=2.25 MHz with a single 8-cycle Hanning-windowed pulse. The trend documented here, of the bigger bubbles' influence on the smaller one resulting in a decrease in overall radial amplitude, is consistent with the experimental work conducted by Garbin et al. – the only known such experiment.

It is also worth noting here that our model does not incorporate bubble coalescence, nor the effects of secondary Bjerknes force. While this is a noted limitation of the model, this force is likely not

the dominant bubble-bubble interaction under the acoustic forcing conditions imposed here (single 10-cycle burst, ~30 kPa). Indeed, in one of the only comparable experimental datasets, Garbin et al.[311] noted no significant translation (on the order of 100-200 nm) between two lipid-encapsulated agents situated $h = 12.5\ \mu$m apart from each other subjected to 150 kPa – higher than the transmit pressures used in the present manuscript.

2.6. Conclusions

For two identical microbubbles vibrating in close proximity to each other, our results show the frequency of maximum response (f_{MR}) decreases (7-10%) and the amplitude of maximum response (A_{MR}) increases (9-11%) as the microbubbles approach one another. For a two-bubble system of different microbubble sizes, the larger bubble shows no change in f_{MR} and a slight shift of A_{MR} (2-3%). However, the smaller bubble exhibits an increase in f_{MR} (7-11%) and a significant decrease of A_{MR} (38-52%). Furthermore, in very close proximity, smaller bubbles exhibit a secondary resonance peak corresponding to the f_{MR} of the larger bubble, with amplitudes comparable to its primary resonance peak. These results have implications in both contrast imaging and microbubble-mediated therapeutic applications.

Chapter 3. Subharmonic Resonance of Phospholipid Coated Ultrasound Contrast Agent Microbubbles (Manuscript)

This manuscript was published in the Journal of "**Ultrasonics Sonochemistry**" in January 2024

Authors: Hossein (Sohrab) Yusefi[1], Brandon Helfield[1, 2]

[1]Department of Physics, Concordia University, Montreal, Quebec, Canada
[2]Department of Biology, Concordia University, Montreal, Quebec, Canada

3.1. Abstract

Phospholipid encapsulated ultrasound contrast agents have proven to be a powerful addition in diagnostic imaging and show emerging applications in targeted therapy due to their resonant and nonlinear scattering. Microbubble response is affected by their intrinsic (*e.g.* bubble size, encapsulation physics) and extrinsic (*e.g*. boundaries) factors. One of the major intrinsic factors at play affecting microbubble vibration dynamics is the initial phospholipid packing of the lipid encapsulation. Here, we examine how the initial phospholipid packing affects the subharmonic response of either individual or a system of two closely-placed microbubbles. We employ a finite element model to investigate the change in subharmonic resonance under 'small' and 'large' radial excursions. For microbubbles ranging between 1.5-2.5 μm in diameter and in its elastic state (σ_0=0.01 N/m), we demonstrate up to a 10% shift towards lower frequencies in the peak subharmonic response as the radial excursion increases. However, for a bubble initially in its buckled state (σ_0=0 N/m), we observe a maximum shift of 8% towards higher frequencies as the radial excursion increases over the same range of bubble sizes – the opposite trend. We studied the same scenario for a system of two individual microbubbles for which we saw similar results.

For microbubbles that are initially in their elastic sate, in both cases of a) two identically sized bubbles and b) a bubble in proximity to a smaller bubble, we observed a 6% and 9% shift towards lower frequencies respectively; while in the case of a neighboring larger bubble no change in subharmonic resonance frequency was observed. Microbubbles that are initially in a buckled state exert no change, 5% and 19% shift towards higher frequencies, in two-bubble systems consisting of a) same-size, b) smaller, and c) larger neighboring bubble respectively. Furthermore, we examined the effect of two adjacent bubbles with non-equal initial phospholipid states. The results presented here have important implications in ultrasound contrast agent applications.

Keywords: Cavitation, Nonlinear Dynamics, Ultrasound Imaging, Non-spherical vibrations, Finite-Element Modeling

3.2. Introduction

Ultrasonic contrast agents, which consist of intravascular encapsulated gas bubbles on the order of 1-8 μm in size, are resonant oscillators in an ultrasound field and give rise to strong scattered echoes, notably at resonance[312]. Indeed, these microbubbles are clinically approved with applications in cardiology and radiology, with recent approval in pediatric patients[313]. While the large magnitude backscatter provides strong signal to the otherwise relatively anechoic blood pool, it is their nonlinear oscillation behaviour that makes microbubbles viable and robust contrast agents[262,304]. Microbubble vibration within a time-dependent ultrasound beam is inherently nonlinear, resulting in asymmetric bubble vibrations that can yield harmonic and subharmonic radial vibrations and scattered emissions – behaviour that is not typical of the relatively linear scattering from tissue. Subharmonic microbubble vibrations, that is oscillations occurring at half

the transmit frequency f, are of particular interest in diagnostic ultrasound applications. Harnessing the subharmonic signals is an attractive strategy for imaging applications since it is unaffected by harmonics generated from nonlinear ultrasound propagation through tissue. Indeed, contrast specific pulse designs have been developed on clinical systems to take advantage of these vibrations to generate bubble-specific images, allowing for suppression of signal originating from the surrounding tissue, recently reviewed in [70]. In addition to quantification of blood perfusion and flow, microbubble vibrations within the subharmonic frequency band for a subset of commercial agents have been shown to be correlated to the ambient hydrostatic pressure; denoted p_0. This correlation has recently been exploited to detect fluctuations in local blood pressure, enabling the new diagnostic application of non-invasive pressure estimation – a technique that has shown promising results in various applications (*e.g.* portal hypertension[144,314], cardiology[315]).

Aside from its use as a diagnostic agent, vibrating microbubbles can be made to elicit local bioeffects under specific ultrasound conditions that may be harnessed for therapeutic applications[270]. Perhaps the most notable of these is the transient opening of the blood-brain-barrier (BBB), which was first demonstrated over two decades ago[217]. While this opening allows a window for local drug delivery to the brain, there have been many pre-clinical studies exploring the acoustic conditions required to ensure safe BBB opening without tissue damage. To reach this goal, recent work in this application has acknowledged that precise control of bubble cavitation is required, and that subharmonic emissions can be employed to actively calibrate exposure levels to increase BBB permeability while minimizing tissue damage[192,201].

For decades, forced bubble vibration physics has been primarily modeled using a 1D ordinary differential equation (ODE) with assumptions on spherical vibrations[261] and bubble isolation

(*i.e.* that the bubble is within an infinite medium). Further extensions of these models to include the effects of the viscoelastic encapsulation of ultrasound contrast agent models have also been established[263,293,295,316]. In practical applications, many of the assumptions of this 1D ODE may not hold; as the non-spherical nature of bubble oscillation has been observed at clinically relevant driving pressures, and that the average inter-bubble spacing between neighboring bubbles *in-vivo* may result in the coupling of two adjacent bubbles. While there have been some insightful studies that further modify the 1D ODE to attempt to incorporate some of these aspects[292,317], they inherently do not capture the influence of the fluid dynamics of the surrounding liquid. In the present manuscript, we extend our previously developed finite-element model[318] to examine the subharmonic response of either an individual or a system of two closely-packed phospholipid encapsulated microbubbles. We examine a range of clinically-relevant microbubble sizes and acoustically interrogate the system over a range of transmit frequencies and acoustic pressures. In this manner, we aim to explore the roles of the salient encapsulation feature of initial phospholipid packing and the presence of an adjacent, nearby microbubble on the frequency-dependence of subharmonic vibrations.

3.3. Mathematical Model

The computational domain employed here is similar to our previous work[318]. Briefly, we simulate either an individual or a system of two microbubbles separated a distance $h = 8\ \mu$m apart (inter-bubble distance; see Fig 3.1). We employ an incompressible fluid (Newtonian) in the Navier-Stokes equations to define the surrounding domain of the microbubble as written below:

$$\nabla . \vec{v} = 0 \tag{3.1}$$

$$\rho\left(\frac{\delta v}{\delta t} + v.\nabla v\right) = -\nabla p + \mu\nabla^2 v \tag{3.2}$$

where v, ρ, μ and p are the velocity, density, dynamic viscosity, and pressure of the fluid respectively. Similar to our previous work, we define the pressure across the bubble wall P_B as a combined contribution of the surface tension, fluid viscosity and pressure due to the viscoelastic encapsulation given by the following equation:

$$P_B = \left(p_0 + \frac{2\sigma_0}{R_0}\right)\left(\frac{R_0}{R}\right)^{3k}\left(1 - \frac{3\kappa}{c}\dot{R}\right) + P_v - \frac{4\mu\dot{R}}{R} - P_{elas} - P_{visc} - P(t) \tag{3.3}$$

where σ_0 is the surface tension at equilibrium (*i.e.* when the bubble is at its resting size R_0), k/c is the ratio of the polytropic index to the acoustic sound speed, P_v is vapour pressure ($P_v \approx 0$), P_{visc} and P_{elas} are the contributions resulting from the viscoelastic nature of the shell (defined below), $P(t)$ is the time-varying driving ultrasound pressure applied at the bubble wall, and the overhead dots denote differentiation with respect to time. The subharmonic activity of an encapsulated microbubble is strongly affected by the viscoelastic material. The encapsulation model that we use for this work is based on a radially-dependent surface tension which is defined by the elastic pressure contribution $P_{elas} = {}^{2\sigma(R)}/_{R}$. This surface tension $\sigma(R)$ is defined by the following equation [263]:

$$\sigma(R) = \begin{cases} 0 \; if \; R \leq R_b \\ \chi\left(\frac{R^2}{R_b^2} - 1\right) if \; R_b \leq R < R_r \\ \sigma_{water} \; if \; R \geq R_r \end{cases} \tag{3.4}$$

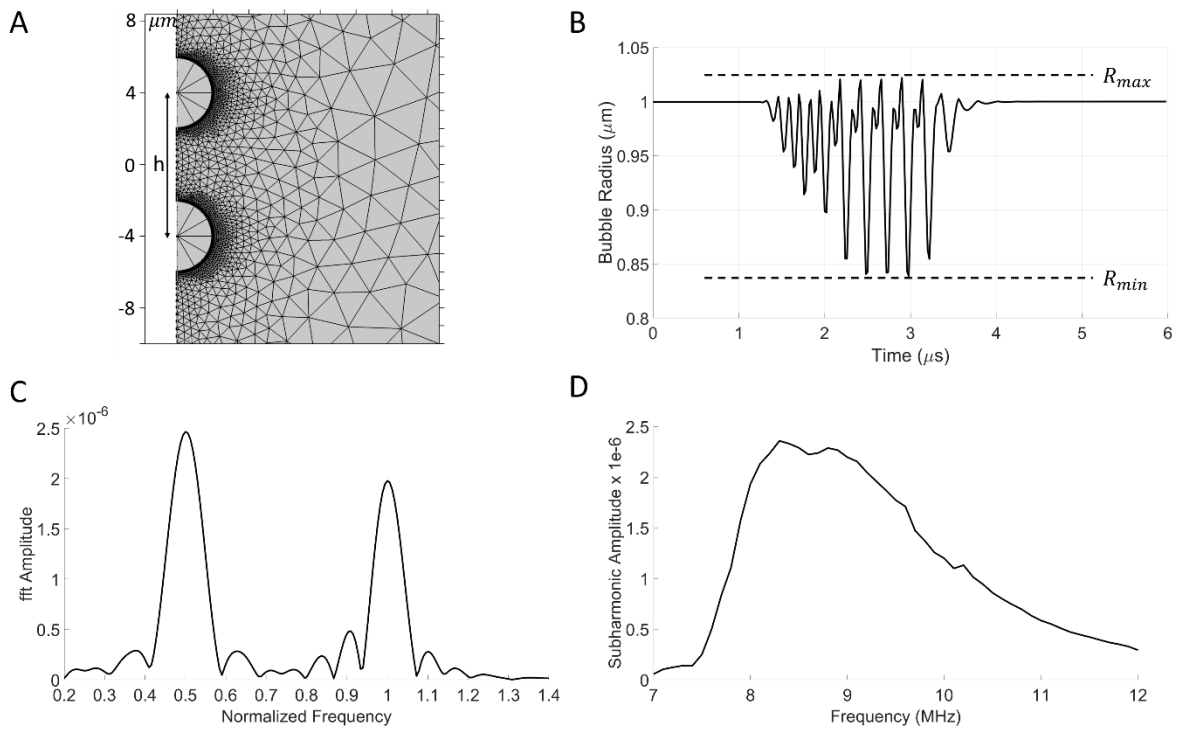

Figure 3.1. Schematic representation of the simulation space and representative example highlighting the subsequent data analysis. A) A finite-element approach was adopted in which an individual bubble (or two, as shown here) is divided into multiple slices to enable application of Eq. 5b in a spatially-dependent manner. An axisymmetric environment was chosen to limit computational time, and the measurement of center-to-centre distance between two bubbles is denoted as *h*. Units are in microns. B) A sample radius versus time plot (*f*=8.3 MHz) driven at 100 kPa. The maximum and minimum radius achieved (R_{max} and R_{min}) were employed to calculate the radial excursion (Eq. 6). Note the clear nonlinear character of the vibration dynamics. C) Fourier transform of the radial change of a 2 micron bubble ($R_0 = 1\ \mu m$) vibrating at 8.3 MHz under acoustic pressure of 100 kPa (same as shown in panel B) showing a powerful subharmonic at 4.15 MHz. D) A sample plot of subharmonic amplitude response as a function of transmit frequency for the same microbubble as in panel B &C. Here, the subharmonic vibration amplitude (in the example of panel C this would be the magnitude at 4.15 MHz – i.e. the normalized frequency of 0.5) is plotted directly against the transmit frequency (8.3 MHz) for a range of transmit frequencies (7-12 MHz, in this case). The transmit frequency at which the subharmonic activity peaks in panel D is termed the subharmonic resonance frequency and the amplitude of this subharmonic vibration is termed the peak subharmonic amplitude.

where χ is the encapsulation elasticity coefficient in units of N/m, and the transition radii – denoted as the 'buckling' and 'rupturing' radius, respectively - are given as $R_b = R_0\left({}^{\sigma_0}/_{\chi} + 1\right)^{{}^{-1}/_{2}}$ and R_r

$= R_b\left({}^{\sigma_w}/_{\chi} + 1\right)^{1/2}$. The selection of the above viscoelastic model warrants some justification. Firstly, it is well established that the interfacial surface tension at the boundary of a phospholipid monolayer changes under strain, seminal experiments of which have been conducted using Langmuir troughs[294]. This experimental evidence is limited to frequencies on the order of kHz and do not incorporate the spherical curvature of a micron-sized bubble, however very recent experimental work using high precision acoustic techniques on monodisperse phospholipid microbubble populations by Segers et al.[319] has demonstrated a similar dependence. The above equation is then a well-accepted model of this behaviour as applied to lipid-encapsulated contrast agents[61,64,263]. Indeed, the buckling of phospholipid encapsulated agents has been experimental observed[320]. Secondly, the initial phospholipid packing (*i.e.* the initial value of surface tension when the bubble is at its equilibrium radius $\sigma(R_0) = \sigma_0$) is known to play a critical role in the presence and magnitude of subharmonic vibrations[275,299]. Indeed, a bubble modeled in its 'buckled' state ($\sigma(R_0) = \sigma_0 = 0\ N/m$) may elicit subharmonic vibrations more readily than in its 'elastic' state ($\sigma(R_0) = \sigma_0 = 0.01\ N/m$)[275]. Practically, it is an unknown parameter for a given individual microbubble (ranging from $0 \leq \sigma_0 \leq \sigma_{water}$), and typical microbubble populations likely possess a range of bubbles with different initial phospholipid packing. The range of initial surface tensions σ_0 have been experimentally estimated via curve fitting experiments, specifically within the context of subharmonic activity, and is typically found to be in the range of $0 \leq \sigma_0 \leq 0.01$ N/m[64,275,299,321,322]. It is for this reason that we focus on examining the effect of this parameter on the resulting subharmonic activity.

The boundary condition on each bubble's free surface is set specifically to keep velocity and pressure on boundary domain continuous:

$$v(R) = \dot{R} \tag{3.5a}$$

$$p(R) = P_B \tag{3.5b}$$

where P_B is defined via Eq. (3.3). The boundary condition we are setting here ensures a no-slip velocity condition with consideration of the tangential shear stress to be of negligible magnitude. By setting the conditions as above, we force a two-way coupling between the fluid domain and the dynamic motion of the bubble wall. To estimate the radius *R(t)*, the surface area of the bubble is calculated, and then the radius is derived from the surface area assuming a sphere (*i.e.* an effective radius).

The aforementioned conditions as well as the condition of constant p_0 on the edges of the computational domain define the complete set of boundary conditions used in this model. For this work, we solve our system using a finite-element approach via COMSOL Multiphysics 5.8 (COMSOL AB. Burlington, MA). Furthermore, the computation was performed in an axis symmetric environment as the model system is symmetrical – this justifies simulating half of the simulation environment in order to save computational time. The dynamic free surface of the microbubble was modeled with a moving mesh via the arbitrary Lagrangian-Eulerian (ALE) algorithm. We used a Tukey windowed 10 cycle pulse as the transmit waveform with a sampling interval of 0.002 μs (sampling frequency equal to 500 MHz). We kept the rest of the parameters in our work constant, which results in $\rho = 1000\, kg/m^3$, $k = 1.095$, $\mu = 0.001\, Pa.s$, $\chi = 1\ N/m$, $\kappa_S = 1.5 * 10^{-9}\ kg/s$, and $\sigma_w = 0.072\ N/m$. The fluid parameters chosen here were based off of those of water, and the encapsulation stiffness and viscosity inputs are within the well-accepted range for phospholipid-encapsulated commercial agents [36,41].

3.3.1. Microbubble Vibration Analysis: Subharmonic Resonance

In our simulations, we use individual tone bursts. The transmit frequency f in this work spanned from 4-22 MHz (with a frequency interval *df* of 0.1 MHz), and the microbubble sizes that we interrogated were in the range of $1.5 \leq 2R_0 \leq 2.5$ μm in diameter ($d = 2R_0$), well within the size distribution of traditional and clinically used microbubble agents [53]. The peak negative pressure in our simulations ranged from 40 to 200 kPa, and the inter-bubble spacing (when simulating a two-bubble system) was kept constant at $h = 8$ μm. We chose the aforementioned parameter ranges due to their relevance in microbubble-assisted therapeutic studies and clinical contrast imaging.

From an individual microbubble radius versus time plot calculated at a given transmit frequency f (Fig. 3.1B), the Fourier Transform was performed at which point the amplitude of the subharmonic vibrational component (*i.e.* the amplitude at $f/2$) was stored (Fig. 3.1C). The amplitude of the subharmonic vibration as a function of transmit frequency is then mapped out, resulting in a subharmonic resonance curve, see Fig. 3.1D. The transmit frequency at which the subharmonic amplitude of this bubble is maximal is termed the subharmonic resonance frequency; and the amplitude at this frequency is termed the peak subharmonic amplitude.

3.3.2. Method of Comparison: Maximal Strain Matching

In addition to modeling the lipid encapsulation monolayer with a radially-dependent surface tension, it is important to note that recent experimental investigations have also gained critical insight into the shell rheology; that is to say how the viscoelastic properties of the shell are modulated as the bubble radial dynamics evolve. Indeed, through both numerical and experimental work[36,61,62,301], it is well understood that encapsulated microbubbles are both strain-softening and shear-thinning oscillators, which manifest as decreasing shell elasticity and decreasing shell

viscosity with increasing radial strain and shear rate, respectively. Therefore, to provide an appropriate comparison between bubble vibrations from different bubble sizes and at different transmit frequencies, we have made such comparisons at constant strain, *i.e.* between bubbles that exhibit approximately equal radial strain at their subharmonic resonance frequency. In this manner, the assumption is that this accounts for the apparent decrease in the viscoelastic properties (which would otherwise shift the native resonant response) and allows for a more direct comparison of subharmonic response. This is in contrast to the comparison of individual bubble responses at a fixed transmit pressure, as is commonly performed. Perhaps this issue is most easily exemplified through the subharmonic threshold phenomenon; whereby it is well established that the frequency-dependent transmit pressure is a threshold indicator of subharmonic activity for a given bubble[323]. Fixing this transmit pressure for a system of two bubbles for analysis of their subharmonic response is either not possible (*i.e.* one of the bubbles does not exhibit subharmonic vibrations) or is intrinsically a comparison between two bubbles vibrating at very different radial excursions, confounding the nonlinear contribution of the viscoelastic shell. Thus, in the results presented below, comparisons are made between microbubbles that exhibit the same ($\pm 2\%$) radial excursion ε at the transmit frequency of maximum subharmonic activity (*i.e.* the subharmonic resonance frequency). The excursion is calculated as

$$\varepsilon(f) = \frac{R_{max} - R_{min}}{R_0} \tag{3.6}$$

where R_{max} and R_{min} denote the maximum and minimum bubble radius at a given frequency, respectively (Figure 3.1B).

To add to our reasoning for choosing the excursion as a basis for comparison, we illustrate the concept via an example in Figure 3.2. The subharmonic resonance curve of an individual $d = 2$

μm microbubble driven at P=100 kPa is shown in Figure 3.2A as a function of initial phospholipid packing, ranging from $0 \leq \sigma_0 \leq 0.01$ N/m, with all other parameters remaining constant. It is clear that the nature of the subharmonic resonance is altered, ranging in subharmonic resonance frequencies from 8.5-10.5 MHz and demonstrating a ~1.5x change in peak subharmonic amplitude response, generally demonstrating a decreasing subharmonic response with increasing initial surface tension (previously shown theoretically for a given parameter set in [275]). However, we also note that the microbubble excursion at the subharmonic resonance frequency, as indicated in the figure legend, greatly varies based on the value of the initial phospholipid packing (14%-20%). From this, we can see that care must be taken in more complex scenarios when interpreting the subharmonic resonance behaviour of a given individual or set of microbubbles at different initial phospholipid density values. Next, we highlight that with all else equal, the microbubble diameter plays a large role in the resulting subharmonic resonance behaviour (Fig. 3.2B). While the shift in subharmonic resonance frequency and amplitude is perhaps not surprising (*e.g.* [61,324]), this data does highlight a range of resonant excursions (11-17%), and exemplifies how a given microbubble in a given context may not exhibit subharmonic emissions (and therefore a subharmonic resonance) at all. The existence of such a subharmonic threshold, for both unencapsulated 'free' bubbles and lipid-coated microbubbles, has been thoroughly explored theoretically and observed experimentally[275,323–327].

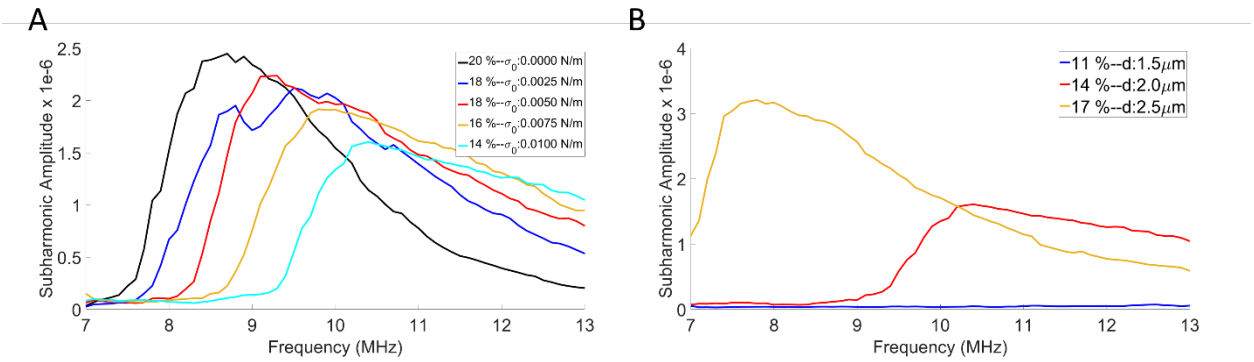

Figure 3.2. The nature of subharmonic resonance curves and the extent of radial excursion strongly depend on both phospholipid packing and bubble diameter. A) A series of subharmonic resonance curves from an individual d=2 μm microbubble with initial phospholipid packing varying from $0 \leq \sigma_0 \leq 0.01$ N/m at a peak-negative pressure of 100 kPa, keeping all other variables constant. Note that the subharmonic resonance excursion (listed in the legend) varies from 14-20%. B) Three subharmonic resonance curves (d=1.5, 2 and 2.5 μm) with all other parameters fixed (P=100 kPa; σ_0 =0.01 N/m). Both the excursion (listed in legend) and the characteristics of the subharmonic resonance are strongly affected by bubble size.

3.4. Results

3.4.1. The Effect of Initial Phospholipid Packing on Subharmonic Resonance

We begin in the simpler scenario of a single microbubble. The effect of the initial phospholipid packing, represented by σ_0, on the subharmonic resonance response as a function of radial strain is shown in Fig. 3.3 for both an individual $R_0 = 1$ μm and an individual $R_0 = 1.25$ μm bubble with σ_0=0.01 N/m (elastic state) and σ_0= 0 N/m (buckled state). As stated above, we compare these responses using the radial strain as the base of comparison, which in this case corresponds linearly with transmit pressure. From the data presented in Fig. 3.3A, the insonication frequency at which the subharmonic response is largest shifts to lower frequencies for bubbles in their 'elastic' state

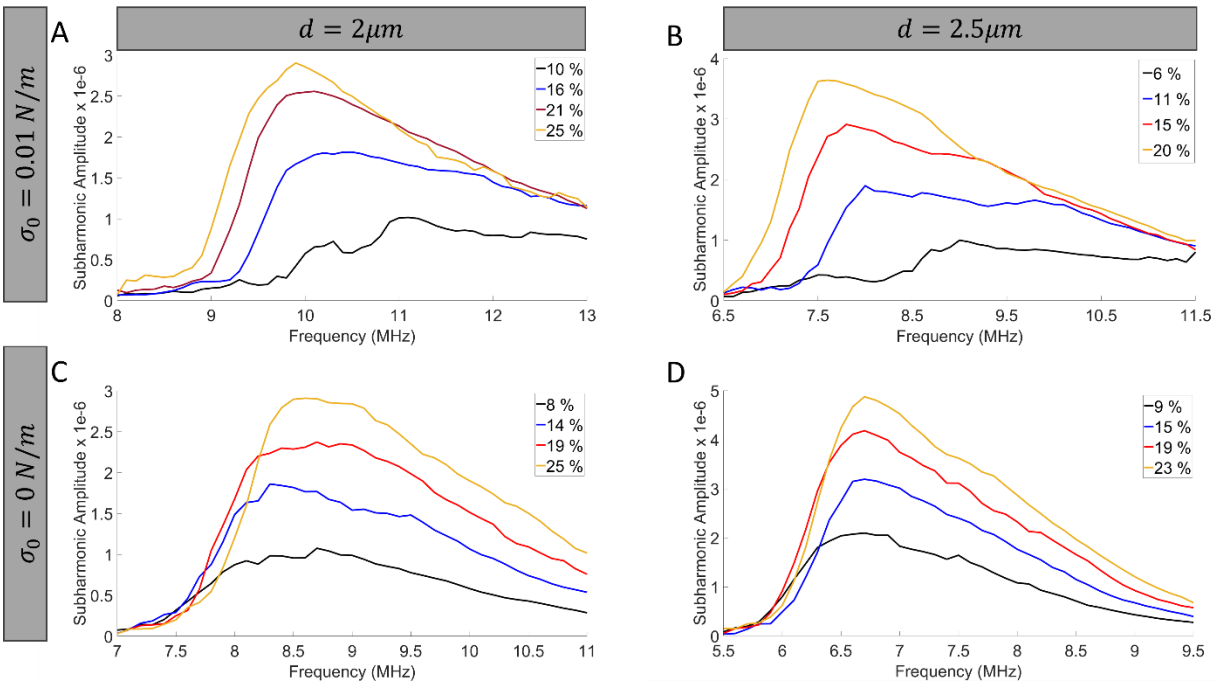

Figure 3.3. The direction of the shift in subharmonic resonance with radial excursion is a function of the initial phospholipid packing. A,B) With increasing radial excursion, the peak in subharmonic resonance frequency for microbubbles starting in their elastic state shifts to lower transmit frequencies regardless of microbubble size. This situation is reversed for microbubbles starting in their buckled state (C,D), where they exhibit an increasing in subharmonic resonance frequency with increasing radial excursion.

($\sigma_0 = 0.01$); for example, from $f = 11$ MHz at 10% excursion to $f = 10$ MHz at 21% excursion for the bubble in Fig 3.3A. In addition to the expected increase in the subharmonic peak amplitude with increasing radial excursion, the behaviour represented for the bubbles that start off in the elastic state mirrors the response typical of the overall radial amplitude[61–63,318].

However, by decreasing the initial phospholipid concentration to σ_0=0 N/m ('buckled' state), we observe the opposite behaviour in that the subharmonic resonance frequency shifts to higher frequencies as the excursion increases, a phenomenon observed for both bubble sizes (Fig

3.3C&D). As we still expect the overall radial amplitude peak f_{MR} to skew towards lower frequencies[318], this suggests that the ratio of these frequencies is decreasing. To examine this more generally, we repeated the simulation for different bubble sizes ranging from $0.75 \leq R_0 \leq 1.25$ μm and with initial phospholipid concentrations of σ_0= 0 N/m; 0.005 N/m and 0.01 N/m. Presented in Figure 3.4, we investigated the excursion-dependent effect of initial phospholipid packing on subharmonic resonance; quantified as the ratio of the subharmonic resonance frequency in the two scenarios of low and high radial excursions. The transmit pressures were chosen in such a way to compare

'low' radial excursions (10±2%) and 'high' radial excursions (20±2%). The data in Figure 3.4 highlights the ratio of the frequencies at which the subharmonic resonance response peaks at these two radial excursions, where the value of 1 corresponds to no change at all. For bubbles in the buckled state (σ_0= 0 N/m), this shift corresponds to an overall 5±2% increase in subharmonic resonance frequency relatively independent of initial size. As the initial packing increases to σ_0=

0.01 N/m, the magnitude of this trend increases and the direction shifts, quantified as a slight shift to lower frequencies (8±2%). For the intermediate value of σ_0= 0.005 N/m, we observe a size-dependent shift ranging from an 11% decrease to a 6% increase.

3.4.2. Two Identical Microbubbles

We next describe the slightly more complex situation in which two identical microbubbles ($R_0 = 1\ \mu$m) are placed within close proximity to one another (center to center distance of 8 μm). As illustrated in Fig 3.5., there is a stark difference in subharmonic resonance in this scenario as a function of the initial phospholipid state in a similar manner (and magnitude) to that of an isolated, individual microbubble. In the buckled state (σ_0= 0 N/m, Figure 3.5A) we see a shift towards

higher frequencies as we increase the pressure and bubble excursion, and in the elastic state (σ_0= 0.01 N/m, Fig. 3.5C) the opposite shift in frequency is observed. In between these two values, at σ_0= 0.005 N/m (Fig. 3.5B), a general shift towards lower frequency is observed with the difference that there is a change in shift direction at a specific threshold of radial excursion. In this scenario, the subharmonic resonance keeps shifting to lower frequencies until approximately 20%

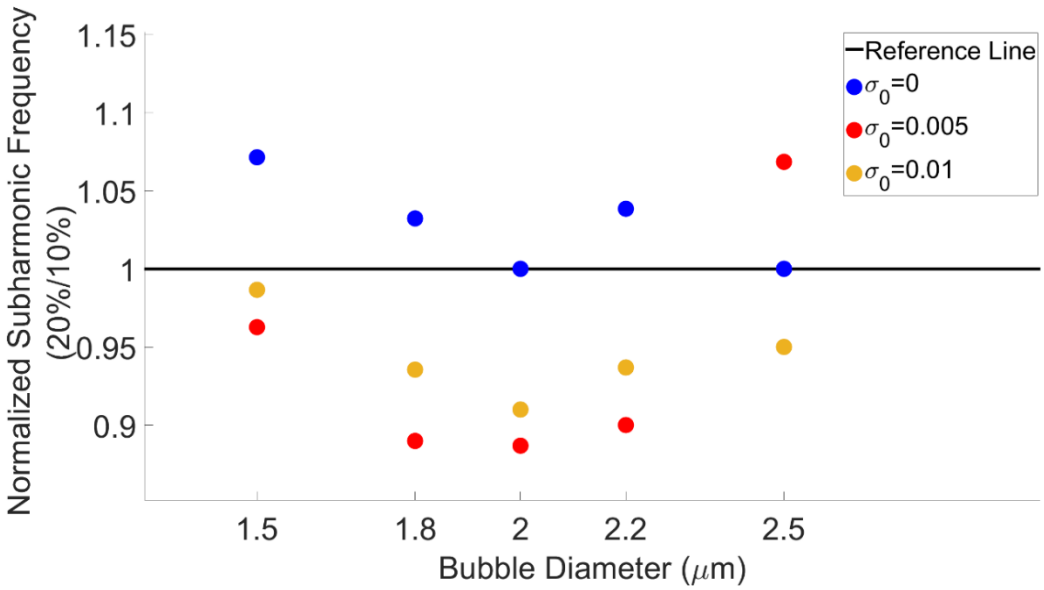

Figure 3.4. The frequency shift in subharmonic resonance behaviour strongly depends on initial phospholipid packing. Summary of the data presented in Fig. 3.3 for a range of microbubble sizes $1.5 \leq d \leq 2.5$ µm. Here, the ratio of the peak frequency of the subharmonic resonance curve for high excursion conditions (20%) to low excursion conditions (10%) is shown. A value of 1 (solid line) indicates no shift in frequency between these two excursion conditions. Subharmonic resonance shifts to lower frequencies when the bubble commences in its 'elastic' state ($\sigma_0 = 0.01$ N/m) while the opposite appears true in the 'buckled' state ($\sigma_0 = 0$ N/m). A mixed response is observed when the packing is in between ($\sigma_0 = 0.005$ N/m).

excursion, at which point there is a jump to higher frequency before which the previous behaviour repeats.

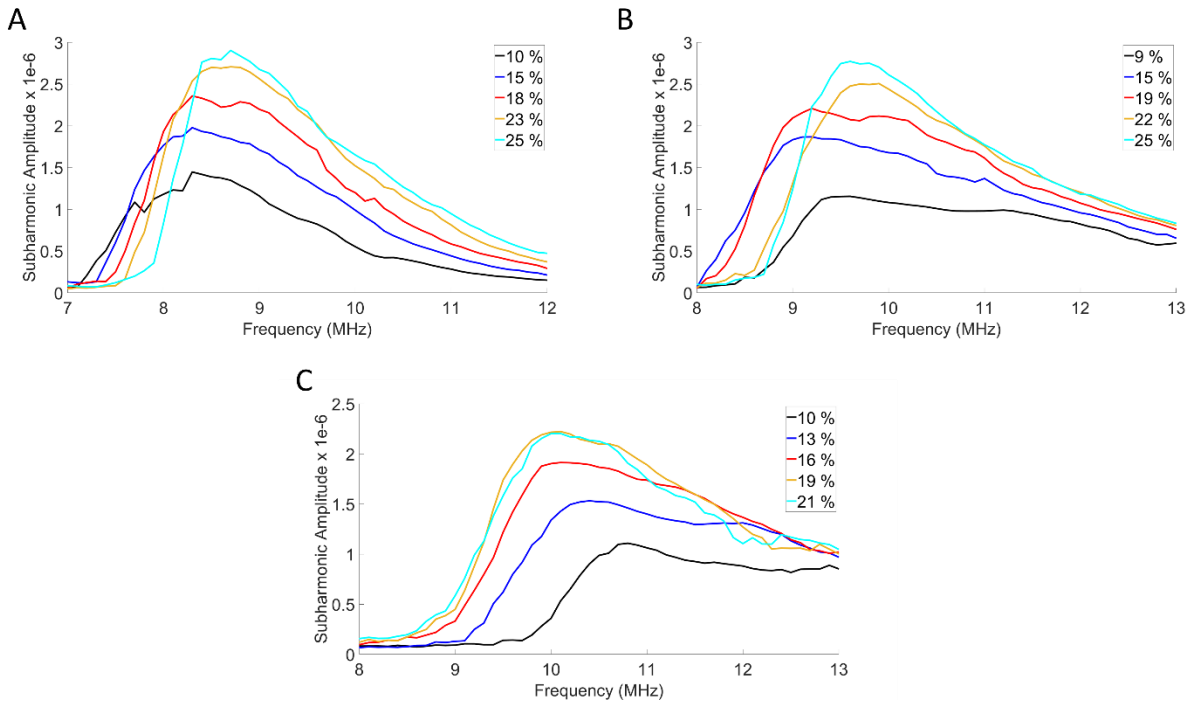

Figure 3.5. A system two identical bubbles exhibits different shifts in subharmonic resonance as a function of initial phospholipid packing. The subharmonic resonance of a 2 µm diameter bubble in close proximity to an identical microbubble modeled in A) its buckled state σ_0= 0 N/m and C) its elastic state σ_0= 0.01 N/m. These behaviours are similar in trend and magnitude to the response of an isolated, individual microbubble. Panel B) shows these curves when examining a system of two microbubbles at an intermediate value of σ_0= 0.005 N/m, which shows an initial shift towards lower frequencies as the excursion increases but switches trends to higher frequencies at a given excursion threshold.

3.4.3. Influence of a Size-Mismatched Neighboring Microbubble

We next evaluate the proximity effect of an adjacent microbubble of unequal size. In this section, we simulate the subharmonic resonance curves of a $d = 2\mu m$ microbubble undergoing different magnitudes of bubble excursion adjacent to either a smaller ($d = 1.5\ \mu m$; Fig. 3.6) or a larger ($d = 2.5\mu m$; Fig. 3.7) partner bubble as a function of initial phospholipid packing. Similar to previous work investigating the effects of a smaller nearby bubble on resonance activity, this smaller-sized microbubble does not significantly affect the subharmonic characteristics of the $d =$

$2\mu m$ bubble (compare figures 3.6A to 3.5A, for example). This includes the direction and magnitude of the

subharmonic resonance curve shifts as a function of initial phospholipid packing. However, a larger microbubble in close proximity does indeed influence the subharmonic response of a $d = 2\mu m$, as can be seen when comparing Figs. 3.5 and 3.7. Perhaps one of the clearer effects of this larger microbubble is the shift down in subharmonic resonance for a given excursion at a given initial surface tension. In comparing, for example, Fig. 3.6A to Fig. 3.7A, the subharmonic resonance frequency for a $d = 2\mu m$ ($\sigma_0 = 0$ N/m) undergoing 9% excursion (black curve) shifts down from 8.2 MHz to 7 MHz, a 15% drop. On an excursion-matched, surface tension-matched basis, this trend is generally true for all of the presented data in Figs. 3.5-3.7. Another influence of the larger

microbubble reveals itself in Fig. 3.7C, where it can be seen that the monotonically shifting subharmonic resonance frequency behaviour is no longer occurring (compare Fig. 3.6C to Fig. 3.7C). Indeed, this suggests that the threshold behaviour at which the direction of this shift changes is modified by both the initial surface tension and by the influence of a nearby, bigger microbubble in close proximity.

To clarify and summarize our findings, Table 3.1 recapitulates the simulations of the two-microbubble systems illustrated in Figures 3.5-3.7 both in terms of the direction and magnitude of the subharmonic resonance frequency shift and peak amplitude change.

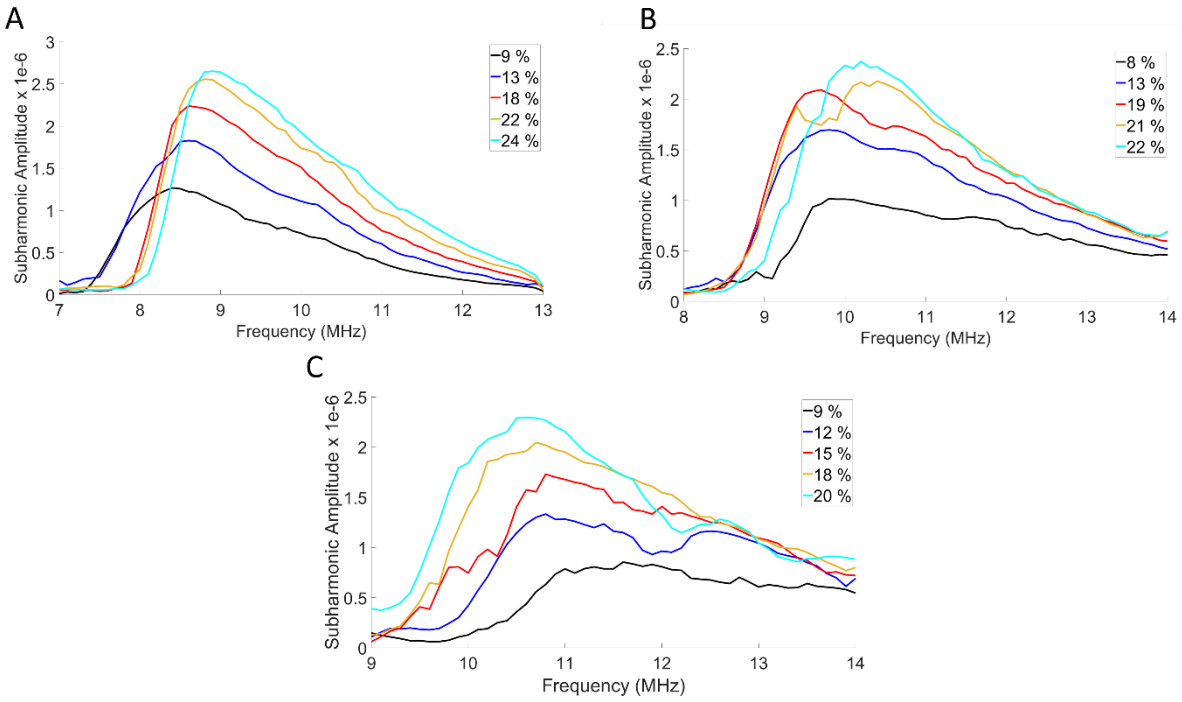

Figure 3.6. The presence of a nearby, smaller microbubble does not significantly alter the subharmonic resonance response of the larger microbubble. The subharmonic resonance curve over a range of maximum strain (given in the legends) of a 2 µm diameter bubble close to a 1.5 µm bubble at A) σ_0= 0 N/m, B) σ_0= 0.005 N/m and C) σ_0= 0.01 N/m. In comparison to the size-matched case (Fig. 3.5), the effect of the initial surface tension is similar both in terms of the shift in subharmonic resonance frequency and amplitude.

3.4.4. Interaction Between Two Bubbles With Different Initial Phospholipid Packing

Finally, we simulate a scenario in which two size-matched microbubbles are in close proximity to each other, each characterized by different initial phospholipid packing. Indeed, this is the most likely scenario in real-world applications of ultrasound contrast imaging. Fig. 3.8 depicts the subharmonic resonance of a $d = 2\,\mu m$ within a two-bubble system consisting of another $d = 2\,\mu m$ bubble, varying the initial surface tension $0 \leq \sigma_0 \leq 0.01$ N/m. The influence of another

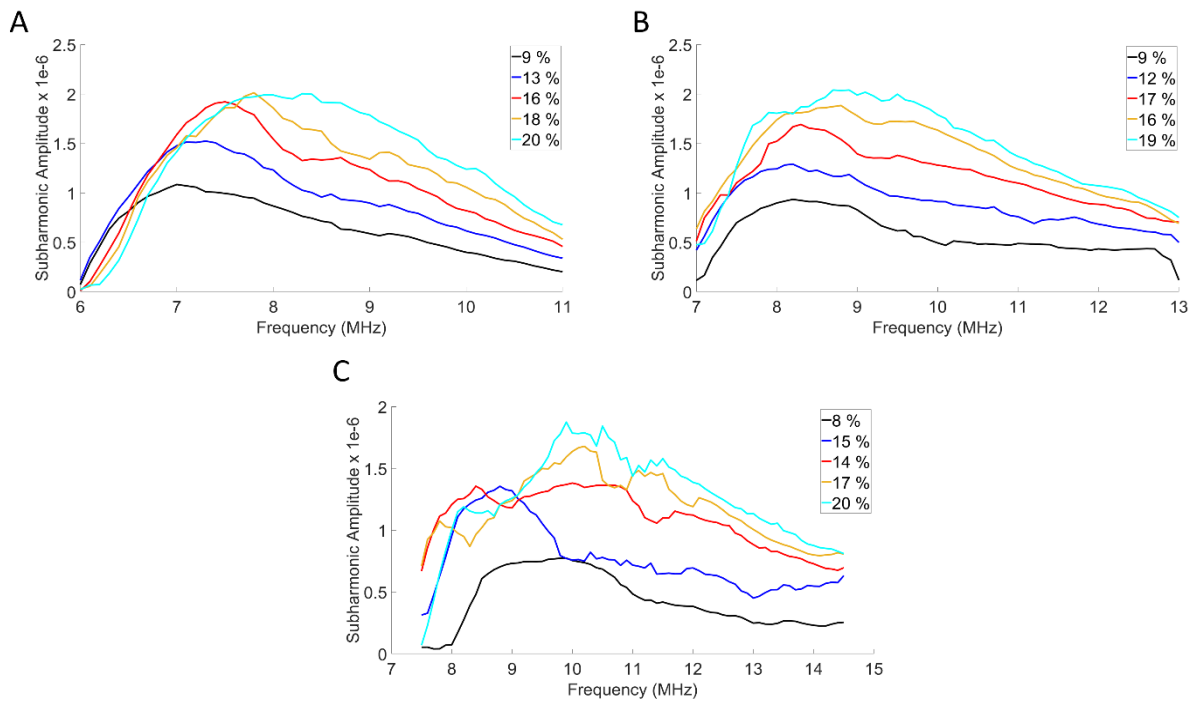

Figure 3.7. A neighboring, larger microbubble alters the character of the subharmonic resonance response of the smaller microbubble. The subharmonic resonance of a 2 µm diameter bubble positioned nearby a larger 2.5 µm diameter bubble at A) σ_0= 0 N/m, B) σ_0= 0.005 N/m, and C) σ_0= 0.01 N/m. In contrast to the other two systems, the presence of a larger nearby microbubbles lowers the transmit frequencies at which the 2 µm bubble elicits subharmonic vibrations. Further, when the two bubbles are modeled with σ_0= 0.005 N/m, there is a clear shift towards higher subharmonic resonance; while at σ_0= 0.01 N/m, we observe an initial decrease up to 15% radial excursion, above which we see a drastic shift to higher resonances.

size-matched bubble is very dependent on the nature of their initial phospholipid packing. In Fig. 3.8A, the subharmonic resonance frequency of an initially 'buckled' bubble slightly increases with increasing initial surface tension of the neighboring, size-matched bubble, while exhibiting a slight decrease in peak subharmonic amplitude. In fact, regardless of the initial phospholipid packing, increasing the σ_0 of the neighboring bubble results in an increase of the subharmonic resonance frequency and a decrease in the peak subharmonic amplitude. The summary of this effect is

displayed in Fig. 3.8D, with a microbubble with intermediate initial surface tension ($\sigma_0 = 0.005$ N/m) exhibiting behaviour in between the other two extremes.

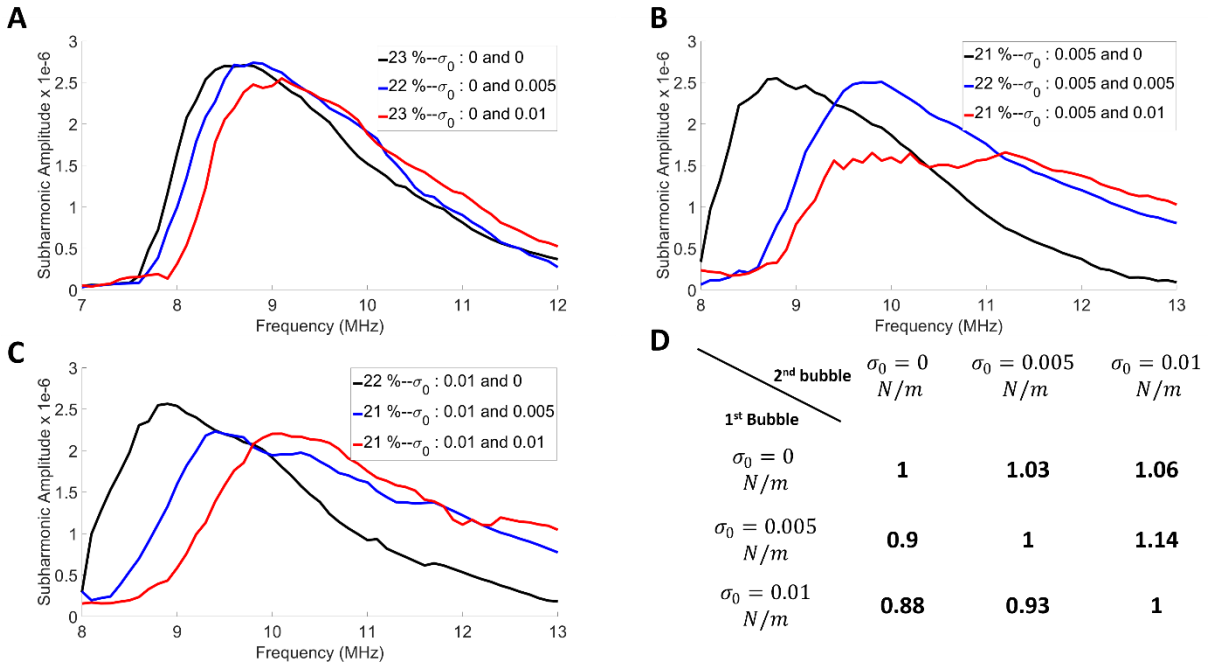

Figure 3.8: Interaction between two same-sized bubbles with different initial phospholipid packing. Subharmonic resonance of a 2 µm diameter bubble placed in close proximity to an equal size microbubble but possessing difference initial phospholipid states vibration at a peak radial excursion of ~21%. In all three scenarios (with the first bubble possessing A) σ_0= 0 N/m, B) σ_0= 0.005 N/m, or C) σ_0= 0.01 N/m), increasing the initial surface tension of the neighboring microbubble results in an increase in subharmonic resonance frequency and a decrease in the peak subharmonic amplitude. The subharmonic resonance frequency shifts are quantified in panel D..

3.5. Discussion

Our results demonstrate the strong effect of the initial phospholipid packing (*i.e.* the initial surface tension σ_0) on the pressure-dependent subharmonic resonance response of both an individual and a system of two closely positioned microbubbles. To place this work within context, it is important to note that the fundamental microbubble response (the radial response at the transmit frequency) as a function in increasing pressure (*i.e.* excursion) has been well examined. From both

experimental[61,62,328] and modelling work[63,66,318,325,329], the pressure-dependent frequency of maximum response f_{MR} from an individual microbubble shift towards decreasing

Peak Frequency Shift Between High and Low Strain			
Neighboring Microbubble	$\boldsymbol{\sigma_0 = 0\ \mathrm{N/m}}$	$\boldsymbol{\sigma_0 = 0.005\ \mathrm{N/m}}$	$\boldsymbol{\sigma_0 = 0.01\ \mathrm{N/m}}$
Size-Matched	0%	-4%	-6%
Smaller	5%	-1%	-9%
Larger	19%	6%	0%
Peak Amplitude Shift Between High and Low Strain			
Neighboring Microbubble	$\boldsymbol{\sigma_0 = 0\ \mathrm{N/m}}$	$\boldsymbol{\sigma_0 = 0.005\ \mathrm{N/m}}$	$\boldsymbol{\sigma_0 = 0.01\ \mathrm{N/m}}$
Size-Matched	+65%	+90%	+100%
Smaller	+100%	+105%	+170%
Larger	+85%	+120%	+140%

Table 3.1. Summary of the subharmonic resonance changes from high and low bubble strain. The percentages denote the ratio between a given metric (peak frequency on the top; peak amplitude on the bottom) under high microbubble strain (20%) to that under low strain (10%). The sign indicates the direction of the change.

frequencies as the transmit pressure is increased. The subharmonic response of an individual micron-sized bubble, in particular phospholipid-coated bubbles, has also been well investigated[65,193,275,296,324,327,330]. These studies, typically at a single frequency spanning a few transmit pressures, have confirmed that subharmonic response magnitude is very sensitive to initial phospholipid packing and bubble size. In particular, it is well understood that subharmonic activity is a threshold phenomenon, observed above a given driving pressure. The transmit frequency f at which this threshold is minimum has been shown theoretically to be $f = 2f_{MR}$ for unencapsulated agents[325], and anywhere between $f_{MR} \leq f \leq 2f_{MR}$ for encapsulated agents[275,327]. Given these two pieces of information, as the resonance frequency shifts towards lower frequencies, so too would the subharmonic resonance frequency be expected to decrease.

However, in one of the only experimental works examining the subharmonic resonance response of individual contrast agent microbubbles, this trend was only partially observed – the subharmonic resonance frequency shifted up on the order of 1-10% with increasing pressure both *in-vitro* and *in-vivo* for many of the individually examined bubbles [299,331]. Indeed, our findings (Fig. 3.2 & Fig. 3.4) suggest that this is due to the strong influence of the initial phospholipid packing and not necessarily the microbubble size (Fig. 3.4); whereby microbubbles that are in their elastic state in equilibrium do indeed exhibit a decrease in subharmonic resonance (as their fundamental resonance does); however microbubbles in their buckled state ($\sigma_0 = 0$ N/m) exhibit the opposite trend of an increase up to 8%, consistent with the aforementioned experimental results. Indeed, while the initial phospholipid packing is difficult to control during microbubble synthesis, there are ongoing techniques currently being explored to force pre-made phospholipid-coated microbubbles into their buckled state before use confirming an association between an initially buckled bubble and increased subharmonic activity[322,332].

It is interesting to note here that, while the direction of the shift in subharmonic resonance frequency (between 10% and 20% excursion) is typically monotonic, there exists specific values of initial phospholipid packing (*e.g.* $\sigma_0 = 0.005$ N/m) in given scenarios where this is not true (see Fig. 3.5B or 3.6B, for example). Indeed, under lower excursions, these bubbles display a similar response to those in their elastic state ($\sigma_0 = 0.01$ N/m), yet shift directions at higher excursions in the same vein as bubbles in their buckled state. This makes the quantified shift in subharmonic resonance frequency and peak amplitude very sensitive (see Table 3.1). We note that in the presence of a bigger microbubble, this phenomenon occurs at a different initial phospholipid packing (see Fig. 3.7C), which emphasizes that this effect is modulated in part by the nonlinear coupling between the oscillations of a neighboring bubble. In principle, this phenomenon can be

measured experimentally, however to our knowledge has not yet been performed. In the other scenarios ($\sigma_0 = 0.01$ N/m or $\sigma_0 = 0$ N/m), we see similar excursion-dependent responses between an individual microbubble and one positioned in close proximity to either a size-matched or a smaller bubble. However, a larger microbubble in close proximity does indeed significantly alter the subharmonic behaviour of the original microbubble, including a shift down in subharmonic resonance for a given excursion at a given initial surface tension.

3.6. Conclusions

In this work, we numerically examined the effect of initial phospholipid packing on the subharmonic response of the microbubbles in both single bubble and two bubble scenarios. We observed that for a range of microbubble sizes ($1.5 \leq d \leq 2.5$) μm in the elastic state (σ_0=0.01 N/m), there is a maximum of a 10% shift towards lower frequencies in the peak subharmonic response as the radial excursion increases; while initially 'buckled' bubbles (σ_0=0 N/m) exhibit on maximum shift of 8% shift in the opposite direction, towards higher frequencies. Furthermore, for a system of two individual microbubbles, we observed similar trends; albeit with a larger neighboring microbubble eliciting a large modulation of subharmonic activity than either a size-matched or smaller bubble. Furthermore, we investigated the effect of two neighboring bubbles with different initial surface tensions (0 N/m to 0.01 N/m) on each other; in this system we observed that the proximity of a nearby, adjacent microbubble with increasing initial surface tension serves to shift the frequency of maximum subharmonic response of the initial bubble towards higher frequencies. The results shown in this work shed some light on the subharmonic behavior of microbubble contrast agents which has important implications in both microbubble-mediated imaging and therapeutic applications.

Chapter 4. The Effect of Micro-Vessel Viscosity on The Resonance Response of a Two-Microbubble System (Manuscript)

This manuscript was submitted to the Journal of "**Ultrasonics Sonochemistry**" in August 2024

Authors: Hossein (Sohrab) Yusefi[1], Brandon Helfield[1, 2]

[1]Department of Physics, Concordia University, Montreal, Quebec, Canada
[2]Department of Biology, Concordia University, Montreal, Quebec, Canada

4.1. Abstract

Clinical ultrasound contrast agent microbubbles remain intravascular and are between 1-8 μm in diameter, with a volume-weighted mean size of 2-3 μm. Despite their worldwide clinical utility as a diagnostic contrast agent, and their continued and ongoing success as a local therapeutic vector, the fundamental interplay between microbubbles – including bubble-bubble interaction and the effects of a neighboring viscoelastic vessel wall, remain poorly understood. In this work, we developed a finite element model to study the physics of the complex system of two different-sized bubbles (2 and 3 μm in diameter) confined within a viscoelastic vessel from a resonance response perspective (3-12 MHz). Here, we focus on the effect of micro-vessel wall viscosity on the resulting vibrational activity of the two-bubble system. The larger bubble (3 μm) was not influenced by its smaller companion bubble, and we observed a significant dampening effect across all transmit frequencies when confined within the vessel of increasing viscosity, an expected result. However, the smaller bubble (2 μm) was highly influenced by its larger neighboring bubble, including the induction of a strong low-frequency resonant response – resulting in transmit frequency windows in which its response in a lightly damped vessel far exceeded its vibration amplitude when unconfined. Further, micro-vessel wall dynamics closely mimic the frequency-dependence of the adjacent bubbles. Our findings imply that for a system of multi-bubbles within a viscoelastic vessel, the larger bubble physics dominates the system by inducing the smaller bubble and the vessel wall to follow its vibration – an effect that can be amplified within a lightly damped vessel. These findings have important implications for contrast-enhanced ultrasound imaging and therapeutic applications.

Keywords:

Ultrasound imaging, Cavitation, Finite-Element modeling, Ultrasound contrast agents, Bubble dynamics, Bubble-Vessel interaction, Nonlinear vibrations

4.2. Introduction

Medical ultrasound contrast agents are small bubbles with diameters ranging from 1 to 8 μm. These bubbles contain a gas core and a thin viscoelastic encapsulating shell. A compressible gas core combined with a viscoelastic shell makes these bubbles very responsive to ultrasound stimulation which serves to increase the ultrasound scattered echo, especially at their resonance frequency [70,312]. These microbubbles are currently approved to be used clinically in cardiology, radiology, and pediatric patients [313]. Due to their size, microbubbles remain confined to the vessels and capillaries and produce a much stronger echo and scattered pressure than the blood pool or surrounding tissue, thus enhancing the vasculature contrast [267]. This improves the ability of quantifying blood flow, which has applications in detection and diagnosis within medical applications such as cardiology and oncology [17,25,72]. Aside from the strong echo of the ultrasound wave, microbubble vibration creates local shear stress and micron-scale fluid flow (micro-streams), which can be harnessed for therapeutic applications such as opening the blood-brain barrier [217], vascular shutdown therapy[182], and sonoperfusion [273]. Furthermore, by binding certain payloads on the surface of these bubbles, they can be used as non-viral carriers with applications in drug and gene delivery [181,249,272,333].

Understanding the behavior and vibration dynamics of microbubbles can play an important role in both diagnostic and therapeutic applications of biomedical ultrasound. One of the key features of microbubble vibration is their resonance response, in which they exhibit their maximum activity (maximum change in radius) at their resonance frequency [261]. Insight into the factors that affect

microbubble response within the context of microbubble synthesis design and pulse sequence development can lead to improved bubble performance. Furthermore, it will help produce more robust and more repeatable measurements and therapeutic outcome. Microbubble vibration dynamics are affected by intrinsic factors, such as bubble size, gas type, viscoelastic shell properties; as well as extrinsic factors such as bubble environment characteristics (*e.g.* fluid viscosity, fluid temperature), transmit ultrasound wave characteristics, and boundary conditions (*e.g.* vessel, particles, or other bubbles) [64,262,274,275,278,279,334] – which may also influence bubble-mediated bioeffects [335].

Indeed, bubble vibration physics has been a focus of many studies in the past decades primarily using 1D ordinary differential equations (ODE), with assumptions such as ensuring spherical microbubble oscillation and complete isolation within an infinite fluid [63,336]. These models have further expansions, each adding an extra consideration, such as viscoelastic encapsulation [263,293,295,316]. However, experimentally, it has been observed that the assumptions of such an underlying analytical 1D ODE may not be valid for biomedical applications. For example, at clinically relevant acoustic pressures, bubbles exhibit non-spherical vibrations [337,338] and can be affected by nearby boundaries such as vessel walls or neighboring bubbles [67,279,307]. There have been expansions of the 1D ODE models to incorporate some of these features further [292,317], however these expanded models are inherently limited as they cannot fully capture the fluid dynamics surrounding the microbubbles.

Finite-element modeling can be a powerful tool to bypass these limitations and consider most aspects of the dynamic interaction of bubbles with their surrounding boundaries. It has recently been applied in a limited number of studies [277,293] including our own previous investigations in which we studied the effect of bubble proximity on the resonance activity of bubbles [318] and

the effect of shell encapsulation on the subharmonic vibrations of a system of multiple bubbles [339]. Here, we further expand our model to incorporate the presence of a cylindrical micro-vessel as a viscoelastic boundary to examine the effect of the microvasculature in a system of two microbubbles, as well as the effect of microbubble vibration on the dynamics of the viscoelastic vessel boundary itself.

4.3. Mathematical Model and Computation Criteria

Our model domain consists of three different materials, a schematic of which is shown in Figure 4.1A, whereby the light blue domain corresponds to bubbles, teal/blue domain to the fluid representing the vessel lumen and extraluminal space, and the gray domain representing the viscoelastic vessel wall. The interaction of the two bubbles and the vessel wall is translated through the fluid. Our model has three multiphysics boundaries and three different types of two-way coupling: bubble-fluid, fluid-solid (inside the vessel), and solid-fluid (beyond the vessel wall). Here, we outline the equations governing each domain and boundary couplings.

4.3.1. Solid Domain

The solid domain is defined by the Cauchy equation of motion (Eq. 4.1a) in which ρ_s is the density of the solid, d_s is solid displacement, σ is Cauchy stress tensor and F_V is the volumetric force. In this model, we use a linear elastic model with Kelvin-Voigt approximation. In such a linear elastic material, Hook's law relates the stress tensor to the elastic strain tensor (Eq. 4.1b), where *C* is the 4th-order elasticity tensor based on Young's modulus and Poisson's ratio [340], ϵ_{el} is the elastic strain, σ_0 and σ_{ext} are initial and external stress, and σ_v is the stress due to viscoelasticity of the material. Indeed, here this contribution is represented with a Kelvin-Voigt formulation (Eq. 4.1c) in which $\dot{\varepsilon_{el}}$ is elastic strain rate and η is the viscosity of the vessel wall.

$$\boldsymbol{\rho_s}\frac{\partial^2 \boldsymbol{d_s}}{\partial t^2} = \nabla.\boldsymbol{\sigma} + \boldsymbol{F_V} \tag{4.1a}$$

$$\sigma = (\sigma_0 + \sigma_{ext} + \sigma_v\ ) + \boldsymbol{C}\colon \boldsymbol{\epsilon_{el}} \tag{4.1b}$$

$$\sigma_v = 2\boldsymbol{\eta}\dot{\varepsilon_{el}} \tag{4.1c}$$

4.3.2. Fluid Domain

The computational domain of fluid and bubbles is similar to our and others' previous works [341]. The fluid domain in this model is governed by the Navier-Stokes equations given below:

$$\nabla.\vec{v} = 0 \tag{4.2a}$$

$$\rho\left(\frac{\delta v}{\delta t} + v.\nabla v\right) = -\nabla P + \mu\nabla^2 v \tag{4.2b}$$

where, $\rho, v, \mu\ and\ P$ are the fluid density, velocity, dynamic viscosity and pressure, respectively. The above set of equations models an incompressible fluid, which is valid since the acoustic wavelength is much larger than the bubble size and fluid velocity is much slower than the speed of sound [261].

4.3.3. Microbubble Dynamics

The pressure on the bubble wall P_B is the result of the contribution of viscoelastic shell, surface tension and fluid viscosity, given as:

$$P_B = \left(p_0 + \frac{2\sigma_0}{R_0}\right)\left(\frac{R_0}{R}\right)^{3k}\left(1 - \frac{3\kappa}{c}\dot{R}\right) + P_v - \frac{4\mu\dot{R}}{R} - P_{elas} - P_{visc} - P(t). \tag{4.3}$$

Here, σ_0 and R_0 are surface tension and radius of the bubble at equilibrium. P_{visc} is the contribution due to the viscosity of the shell defined as $4\kappa_s\dot{R}/R^2$ with κ_s being surface dilatational viscosity of

the monolayer, k is the polytropic index, c is the speed of sound, and p_0 is the ambient pressure. The vapor pressure P_v is considered negligible, consistent with many other bubble modeling work (e.g. [263]). Furthermore, P_{elas} representing contribution due to the elastic shell is defined by $P_{elas} = 2\sigma(R)/R$, in which $\sigma(R)$ is the dynamic surface tension and defined below [263]:

$$\sigma(R) = \begin{cases} 0 \; if \; R \leq R_b \\ \chi\left(\frac{R^2}{R_b^2} - 1\right) if \; R_b \leq R < R_r \\ \sigma_{water} \; if \; R \geq R_r \end{cases} \tag{4.4}$$

with the terms R_b and R_r denoting 'buckling' and 'rupturing' radii and are defined as: $R_b = R_0\left({}^{\sigma_0}/_{\chi} + 1\right)^{-{}^{1}/_{2}}$, $R_r = R_b\left({}^{\sigma_w}/_{\chi} + 1\right)^{{}^{1}/_{2}}$, and χ is encapsulation elasticity coefficient with the unit of N/m.

4.3.4. Boundary Conditions and Coupling

The boundary conditions set in bubble-fluid interaction are such as to ensure continuity of velocity and pressure on the surface of bubbles, and given below:

$$v(R) = \dot{R} \tag{4.5a}$$

$$P(R) = P_B. \tag{4.5b}$$

Indeed, the above equations ensure a two-way coupling between bubble surface motion and the surrounding fluid. In this system, we have a no-slip velocity condition, and the tangential shear stress is considered to be negligible. Furthermore, the boundary conditions are set in fluid-solid interaction to ensure the continuity of velocity (Eq. 4.6a) and equilibrium of stress on the fluid-solid boundaries from inside and outside the vessel. The equations dictating these conditions are given below:

$$v = \frac{\partial d_s}{\partial t} \tag{4.6a}$$

$$\sigma.n = \boldsymbol{\tau}.n, \boldsymbol{\tau} = [-P\boldsymbol{I} + \mu(\nabla v + (\nabla v)^T)] \tag{4.6b}$$

Equation 4.6b represents the equilibrium of stress over the boundary. $\boldsymbol{\tau}$ is the linear stress derived from Navier-stokes equations, and I is the identity matrix.

4.3.5. Calculations

We developed this finite element model using COMSOL Multiphysics 5.6 [5] to calculate the radial dynamics of the bubbles. An example of the number of elements used in our calculations is shown in Figure 4.1B. The main output of our model is the time-dependent radius of the bubbles as derived from the integration over the surface area of the bubble. Further, we derive the maximum radial change by averaging the maximum amount of expansion and minimum amount of contraction (maximum radial change = $R_{max} - R_{min}/2$), as shown in Figure 4.1C. By running the same calculation over a range of transmit frequencies, we derive a resonance curve representing the maximum change in amplitude or maximum response as a function of transmit frequency. For each of these resonance curve, we calculate the amplitude and frequency of the maximum response, A_{MR} and f_{MR} respectively.

4.3.6. Variable Selection

Clinical ultrasound contrast agents are polydisperse, ranging broadly speaking in size from 1 to 8 μm and concentrations from ~3-100 x10^8 microbubbles per ml[313]. Previous work using established acoustic techniques have shown that the peak in the frequency-dependent response from microbubble populations corresponds well with the volume-weighted mean size[43,342]. Indeed, the volume-weighted mean size of commercial lipid agents fall between 2-3 μm in

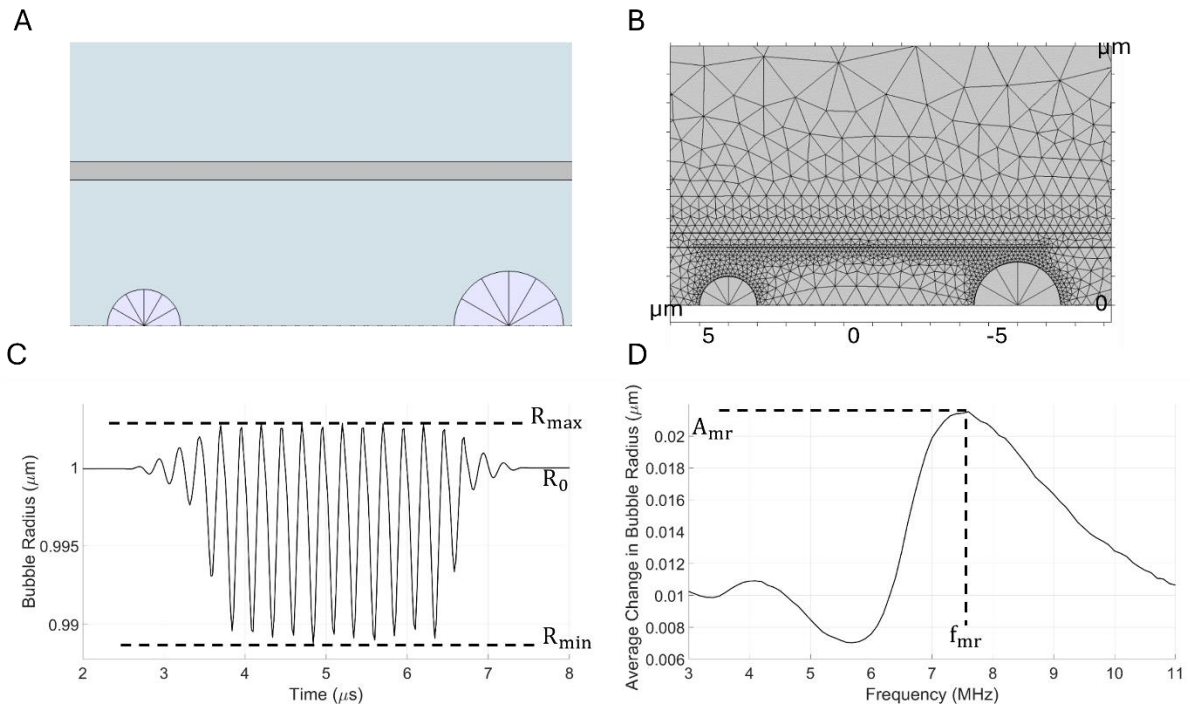

Figure 4.1. Model environment and representative example of the metrics employed. A) A schematic view of the model domain representation, in which the light blue area represents the gas, teal represents the fluid, and gray region represents a viscoelastic vessel wall. B) Example of mesh system representing the finite elements applied to the modeling environment. The areas of interest, including between the bubbles and the vessel wall, have a finer mesh pattern to increase calculation accuracy. C) Representative example of the resulting microbubble-time curve for a microbubble of initial size $2R_0$. Both maximum R_{max} and minimum R_{min} radii are recorded to develop an amplitude metric that is then plotted as a function of transmit frequency, as shown in panel D. From here, the frequency of maximum response f_{MR} and the amplitude of maximum response A_{MR} are extracted.

diameter, including Sonazoid[46], MicroMarker™ [343] and Definity™ (although it has a second volume peak at ~7-8 μm) [36,37]. Motivated by this, here we examine the radial dynamics of two microbubbles with diameters 2 μm and 3 μm, respectively, separated by a center-to-center distance of 10 μm. The physical parameters we employed for the fluid, $\rho = 1000\,\frac{kg}{m^3}, \sigma_w = 0.072\,\frac{N}{m}, , \mu = 0.001\ Pa.s$ are standard values for water, and we chose the following quantities for those related

to the microbubbles: $k = 1.095, \chi = 2.5\ \frac{N}{m}, \kappa_s = 1 \times 10^{-9} kg/s, \sigma_0 = 0.01 \frac{N}{m}$. Here, we acknowledge that there are complexities with strain-dependent elasticity and shear-dependent viscosity that we are ignoring[62,301,344]. However, while likely present to some extent, we selected to fix the shell elasticity, viscosity, and initial surface tension similar to those previously reported for lipid agents[36,61,64,84] to allow for a more direct comparison between transmit frequencies.

These two bubbles are situated within a small vessel (4 μm in diameter) that is on the order of the size of capillaries. Indeed, bubble dynamics has been shown to be affected by the mechanical properties of their neighboring boundaries[279,307]. Most tissues exhibit frequency-dependent viscoelastic properties[84,345,346], however few studies have explored such viscoelastic parameters of biological tissue at megahertz frequencies. Of relative note is the robust work by Hong Chen and colleagues[347] who, with ultrafast bright-field microscopy imaging, constrained the vessel relaxation time $\tau = \eta/E$ of rat mesentery venules driven at 1 MHz to on the order of microseconds, where η and E are the viscosity and stiffness measures, respectively. Static elastic moduli within arteries have been shown to decrease with decreasing intraluminal pressure, in the range of 1-20 MPa over 40-220 mmHg[348]. Given the mean *in-situ* capillary pressure is on the order of 10-60 mmHg[349,350], we set the elastic modulus to 1 MPa. Correspondingly, here we investigate microbubble-vessel dynamics over viscosity values η ranging from 0.1, 0.5, and 1 Pa·s to place our selection of the vessel mechanical properties within what is known of the current physical paradigm.

In terms of the transmit parameters, we employed a transmit pressure of 30 kPa consisting of a single 20-cycle cosine tapered Tukey windowed pulse at a sampling frequency of 500 MHz;

similar to single-pulse experimental studies[61,62,301,351]. Furthermore, we simulate the system in a frequency sweep range of 2-12 MHz, which covers most frequencies used in clinical ultrasound[267]. Since microbubble size (~µm) is much smaller than a typical focal point (~mm), they are considered to be in a uniform domain of ultrasound wave.

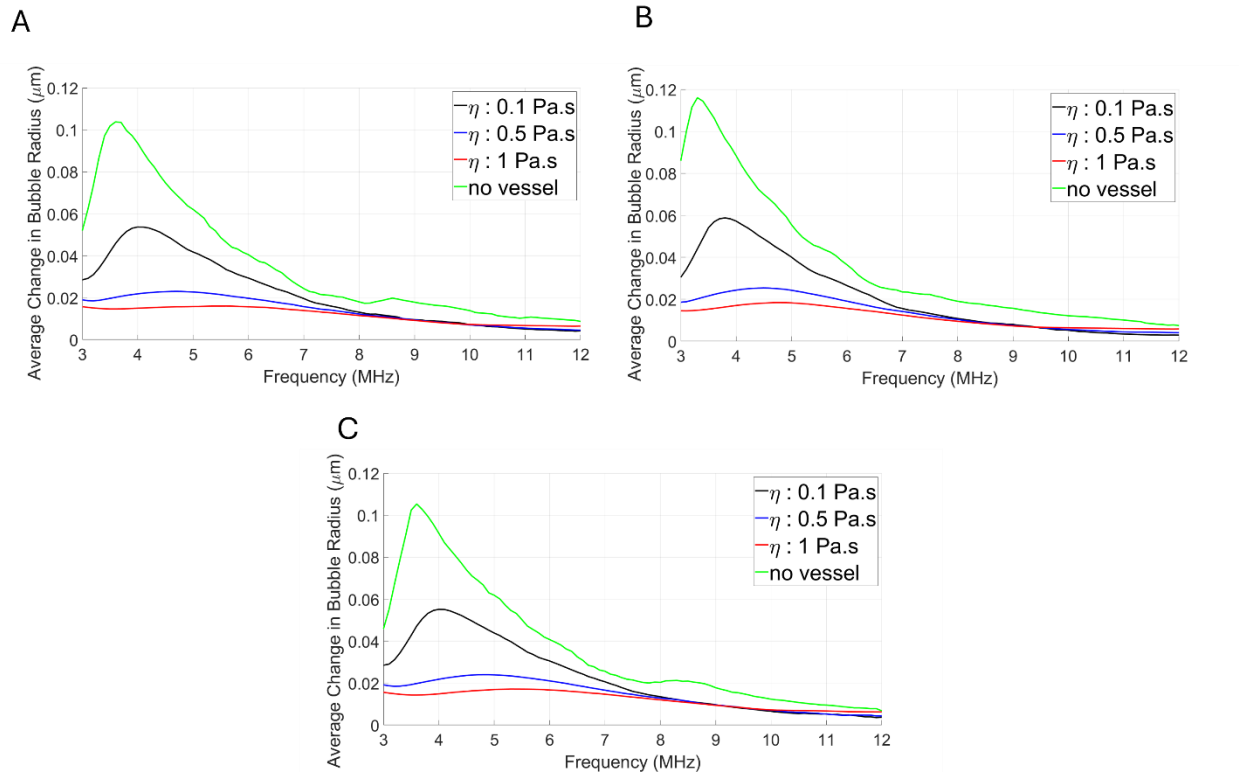

Figure 4.2. Large microbubble exhibits dampened response within the vessel and remains unaffected by smaller, companion bubble. A) For context, the resonance response of an individual 3 µm bubble in isolation and within free space. B) When placed near an identical microbubble, there are slight shifts in the frequency of maximum response. C) Further, when placed near a smaller, 2 µm bubble, there is no appreciable effect. In all cases, microbubble response is dampened as the bubble is placed within progressively more viscous micro-vessels.

4.4. Results and Discussion

4.4.1. Resonance Response of Each Bubble of a Two-Bubble System Within a Micro-vessel

We first analyze the frequency-dependent radial dynamics of a large bubble (3 μm in diameter) within the two-bubble system in various physical scenarios. In each panel of Figure 4.2, there are four lines representing this bubble confined in a vessel with increasing viscosity of η=0.1 Pa.s, 0.5 Pa.s, or 1 Pa.s. The green line represents a bubble vibrating in the absence of a vessel wall, in an infinite free medium with all other conditions equal. Across all panels, bubble confinement within a micro-vessel decreases the amplitude of maximum response A_{MR}, with the extent of this change increasing with increasing vessel viscosity. For an individual 3 μm bubble (Fig. 4.2A), A_{MR} decreased to 50% when placed in a vessel of η=0.1 Pa·s, dropping down to 10% and 5% in the η=0.5 Pa·s and η=1 Pa·s vessels, respectively. Furthermore, there is a slight increase in the frequency of maximum response f_{MR} with increasing vessel viscosity – ranging from 3-4 MHz with increasing η values. Indeed, this shift of bubble resonance to higher frequencies when confined in a viscoelastic vessel is consistent with other numerical studies[297,352]. When placed in the close proximity of an identical bubble (Fig. 4.2B), A_{MR} is slightly larger (ranging from 105-110% the values without its companion bubble) and f_{MR} shifts slightly to lower frequencies (~1-10% shift across all vessel conditions compared to in isolation). Finally, when placed adjacent to a smaller bubble of 2 μm (Fig. 4.2C), there is no appreciable change in behaviour compared to this bubble in complete isolation (Fig. 4.2A). This suggests that a smaller, neighboring companion bubble does not influence the dynamics of other bubbles – a concept that is consistent with previous works[318].

Next, we examine the response of the smaller, 2 µm bubble in the same set of confinements as above. First, we note that a 2 µm bubble in isolation (Fig. 4.3A) exhibits an asymmetrical resonance response, with an f_{MR} of 7.8 MHz, and a distinguishable second-harmonic peak at approximately 4.9 MHz. Asymmetrical resonance phenomena are a known nonlinear property of lipid encapsulated microbubbles, and have been previously observed both experimentally (e.g. [61]) and via modeling[63]. When placed within the viscoelastic micro-vessel, the expected dampening

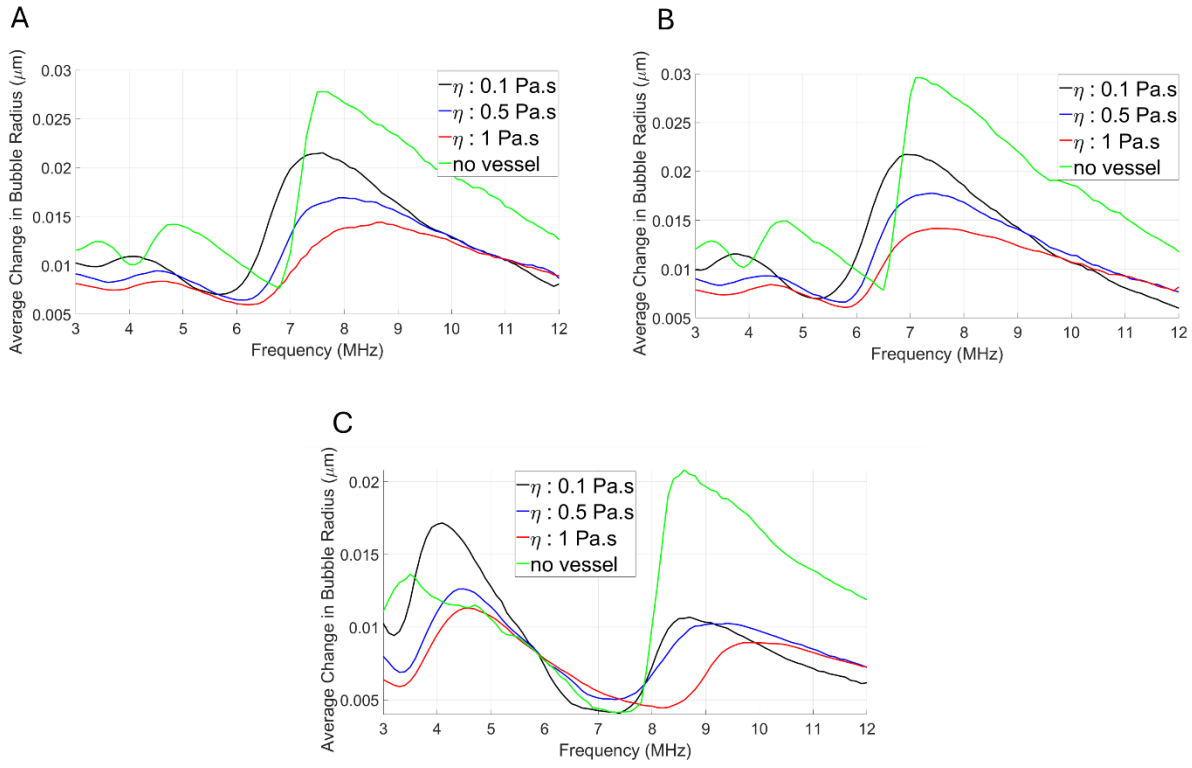

Figure 4.3. Small microbubble exhibits induced resonance and larger vibration magnitude within lightly damped micro-vessel due to the presence of a neighboring, larger bubble. A) For context, the resonance response of an individual 2 µm bubble in isolation and within free space. Note the asymmetrical resonance that is characteristic of a stain-softening material. Due to this, there is a small frequency window in which the bubble response is larger in magnitude when confined (~6-7 MHz). B) When placed near an identical microbubble, there is a slight shift in f_{MR} towards lower frequencies, and an increase in A_{MR}. C) When placed near a larger, 3 µm bubble, there is a large induced resonance effect near 4 MHz, which aligns with the 3 µm bubble

resonance. At this transmit frequency, the bubble vibration amplitude is larger when confined within a lightly damped ($\eta = 0.1$ Pa·s, black trace) micro-vessel as compared to in complete isolation (green trace), and is larger than its main resonance peak (~8.2 MHz).

of the resonance response is observed, however to a lesser extent than that shown in Fig. 4.2A – with A_{MR} decreasing to 77% when placed in a vessel of η=0.1 Pa·s, dropping down to 60% and 55% in the η=0.5 Pa·s and η=1 Pa·s vessels, respectively. It can also be seen that, along with an accompanying increase in f_{MR}, there is a gradual change from an asymmetrical to symmetrical response with increasing vessel viscosity. Due to this, there exists a small frequency window below

main resonance (6.5-7 MHz) at which the confined bubble response will be larger in magnitude than in complete isolation, a behaviour not seen for the larger 3 μm bubble (Fig. 4.2A). When two such identical bubbles are placed close to one another (Fig. 4.3B), there is a slight shift in f_{MR} towards lower frequencies, and an increase in A_{MR}. However, when placed in proximity to a larger neighboring bubble (Fig. 4.3C), it is clear that A_{MR} within the vessels decrease to a much larger extent than in the other two physical systems, decreasing to 50% when placed in a vessel of η=0.1 Pa·s, and 48% and 38% in the η=0.5 Pa·s and η=1 Pa·s vessels, respectively. In addition to this, the presence of a secondary induced resonance response (~4 MHz) is observed, corresponding to the resonance response of the larger, 3 μm bubble – a phenomenon that we have previously reported on[318]. Perhaps in part due to this, the below-resonance frequency window in which the confined bubble vibration was larger than when unconfined is no longer present (6.5-7 MHz). However, the secondary, induced resonance peak observed between 3.5-5.5 MHz illustrates a region of large bubble vibration within the η=0.1 Pa·s vessel, a factor of 1.7-fold that of its main

resonance response. As such, over this particular frequency range, the A_{MR} far exceeds (~1.5-fold) that of the two-bubble system in isolated, free space (green cure in Fig. 4.3C).

4.4.2. Microbubble Harmonic Activity

To further examine the interactions outlined above, we next investigated the harmonic activity of the two microbubble-system in a lightly damped vessel characterized by η=0.1 Pa·s (Fig. 4A & B), where the frequency spectrum is given as a function of transmit frequency for the 3 µm (left) and 2 µm (right) bubbles. Here, we can see clear demonstration of higher-order harmonics from both microbubbles.

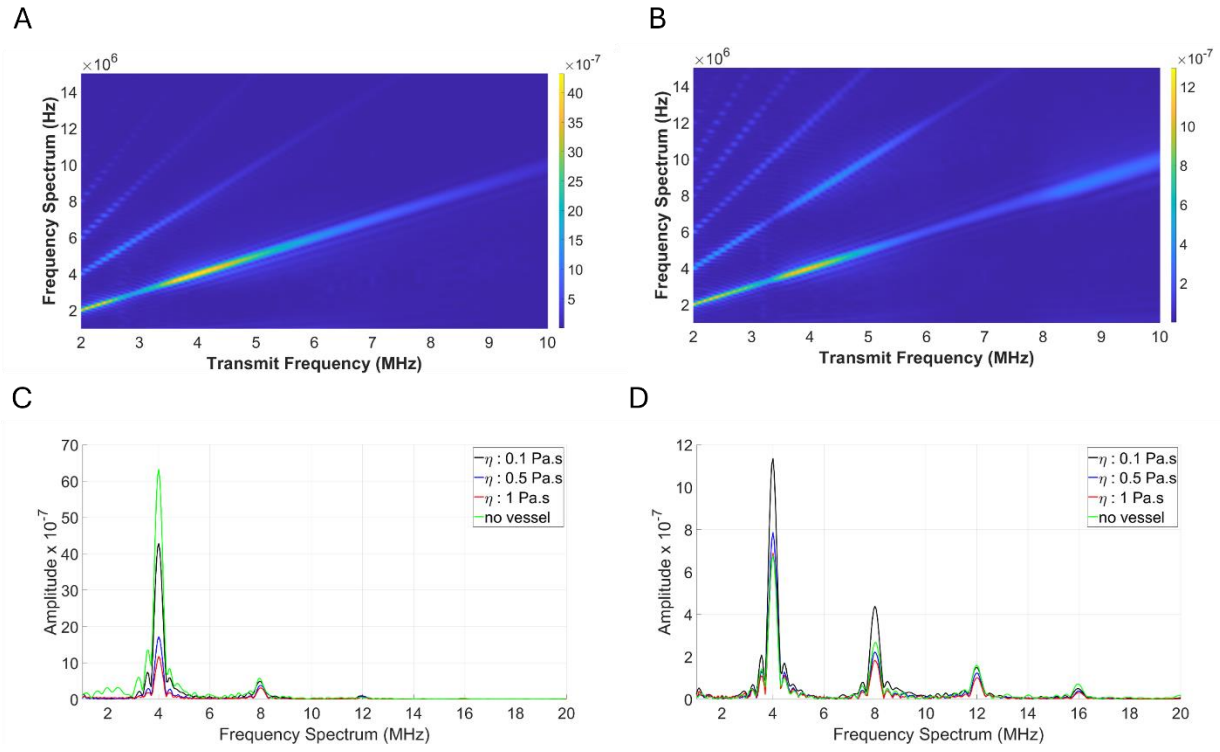

Figure 4.4. The induced resonance response also translates to second-harmonic oscillations. Density plots highlighting the response frequency (y-axis) as a function of transmit frequency for the larger (panel A, 3 µm) and the smaller (panel B, 2 µm) of the two-bubble system within a lightly damped vessel ($\eta = 0.1$ Pa·s). Here, color encodes the magnitude of bubble vibration. We can clearly observe the presence of higher-order harmonics, including the induced resonance response for the 2 µm bubble near a transmit frequency of 4 MHz.

The response frequency spectrum at a transmit of 4 MHz as a function of micro-vessel viscosity is shown for both bubbles in panels C (3 μm) and D (2 μm). While the larger bubble exhibits the expected trend of attenuated signal with increasing confinement viscosity, the smaller microbubble vibrates with larger magnitude at both fundamental and second-harmonic frequencies within the lightly damped vessel ($\eta = 0.1$ Pa·s; black trace) as compared to in complete isolation (green trace). Note that for the smaller bubble, a transmit frequency of 4 MHz is off-resonant.

Consistent with our above results, the larger of the two bubbles possess a resonance response around 4 MHz, accompanied by harmonic structure that attenuates as the vessel viscosity increases (Fig. 4.4C). The smaller microbubble possesses a strong off-resonant dynamic at 4 MHz, corresponding to the frequency at which its larger, companion bubble is resonant. Similar phenomena extend to the harmonic space, whereby the second and third harmonic content at this off-resonant transmit frequency is significant (Fig. 4.4D). Of particular interest is the fact that the response of this 2 μm bubble within the η=0.1 Pa·s vessel (black curve) is larger than in free space (green curve) at this off-resonant transmit frequency (Fig. 4.4D) by a factor of ~50%. This behaviour is also present for its second harmonic response, in which there is an increase in ~30% between these two scenarios.

4.4.3. Micro-vessel Wall Dynamics Strongly Influenced by Larger of The Two Bubbles

As a natural extension, we next investigated the vibration dynamics of the vasculature itself (Figure 4.5), specifically directly adjacent to the larger bubble (Fig. 4.5A) and the smaller bubble (Fig. 4.5B). Broadly speaking, we observe that the vessel wall follows the same behavior as the bubble directly adjacent to it, both in terms of resonance response and harmonic generation. Note that this is consistent with the limited experimental evidence available, albeit for isolated, individual microbubbles within small capillaries[180] and individual endothelial cells[286]. Briefly, in this two-bubble system arrangement, this results in the overall vessel response being more powerful

around 4MHz, showing the dominance of the larger bubble response in the system both in terms of microbubble vibration and that of the vessel wall.

4.4.4. Confinement-Dependent Induced Resonance Persists for Bubbles Smaller Than 2 μm

To gain further insight into the confinement-dependence of the induced resonance response of the smaller bubble within a two-bubble system, we explored how this effect translates when varying the size of the smaller bubble (Figure 4.6). Here, we examine the resonance curve of smaller bubbles ranging from $1.5 \leq 2R_0 \leq 2.25$ μm while holding the size of the larger bubble constant at $2R_0 = 3$ μm. The transmit frequency range is limited here from 3-6 MHz in order to focus on this induced resonance range. Two confinement scenarios are presented: the two bubble system within a lightly damped micro-vessel ($\eta = 0.1$ Pa·s; black trace) and in infinite free-space (green trace). As can be seen from the figure, microbubbles smaller and equal to 2 μm in diameter exert a much larger oscillation magnitude when confined within this vessel – up to ~40% - as compared to free-space. However, for the 2.25 μm bubble, the more expected result of the vessel confinement decreasing the amplitude of resonance activity is observed, in this case by ~10% (Fig. 4.6D). We also observe a shift of this induced frequency peak towards smaller frequencies for this bubble combination, due to the increasing overlap between the main and induced resonance values. Note that, as the companion bubble scales up to 3 μm, there is a ~50% decrease between these two contexts, as shown in Figure 4.2B. Taken together with Fig. 4.2-4.5, this has implications in the context of both imaging and emerging microbubble-assisted focused ultrasound applications. Firstly, given the polydisperse nature of commercial agents and the native microbubble density associated with clinical doses, these types of scenarios (in which multiple bubbles of different sizes will be in close proximity to each other) are common. While there is ongoing research to develop

monodisperse microbubbles, they are still characterized by significant coefficient of variations[308,309], which further justifies this type of system.

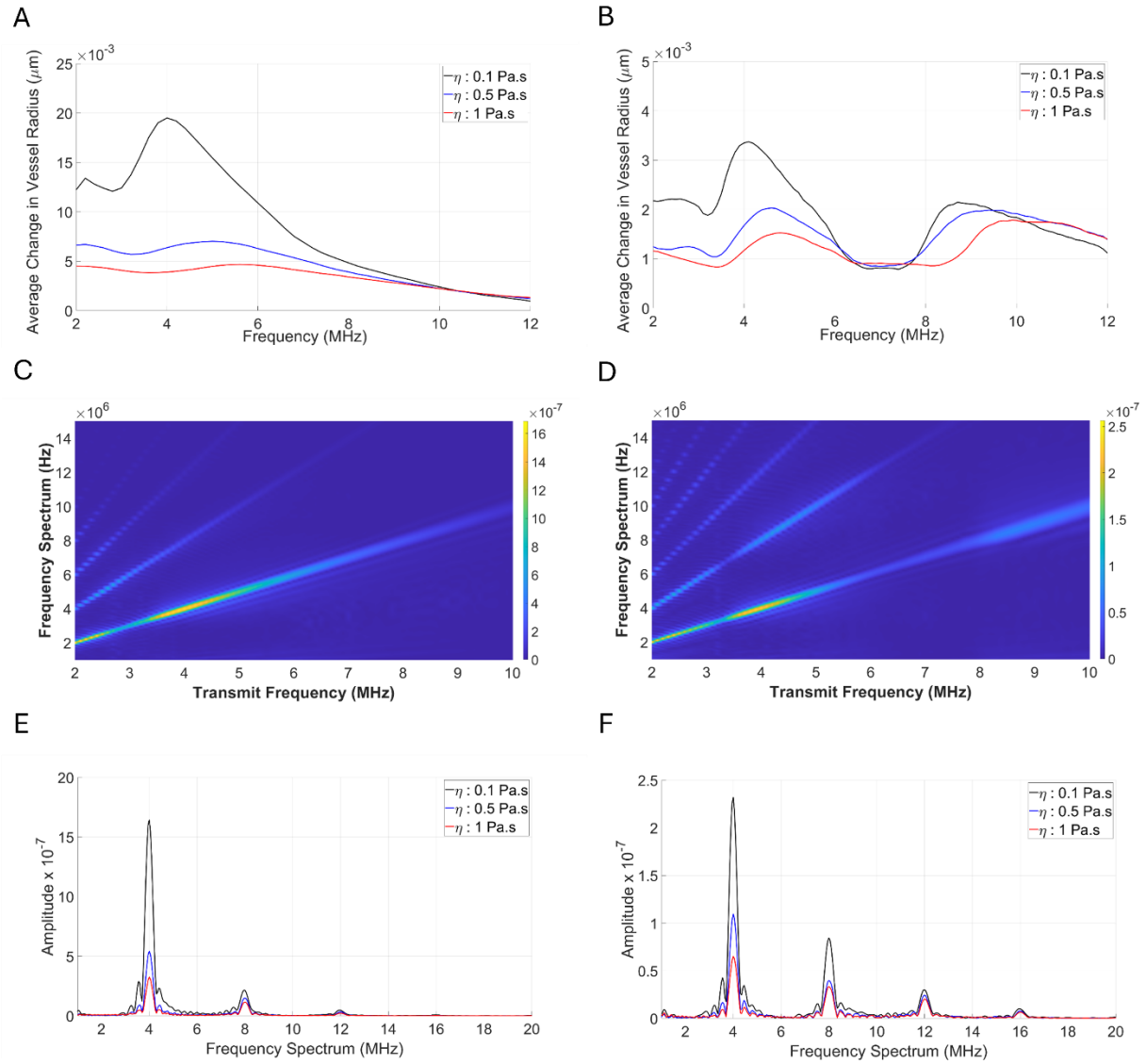

Figure 4.5. Micro-vessel wall dynamics follow the behaviour of the adjacent microbubbles. The vessel wall movement directly adjacent to the 3 µm bubble depicts a similar trend both in terms of A) resonance response and C,E) harmonic vibration content as the vibrating bubble (see Fig. 4.4). Additionally, the induced resonance response also translates to the vessel movement, seen here through the B) resonance curve and D,F) the harmonic content of the vessel portion adjacent to the smaller, 2 µm bubble. This data suggests that, when multiple bubbles are present within a vessel, the vessel contraction and expansion is dominated by the frequency-dependence of the larger microbubble.

Secondly, this dataset implies that when considering contrast imaging parameters, favour should be given to the larger bubbles of the intended bubble distribution, as they seem to dominate the response of smaller adjacent bubbles. In fact, this phenomenon of induced response may also influence the radial dynamics of nanobubbles, a recently introduced research-based ultrasound contrast agent [112]. Third, microvascular wall movement is also strongly linked to the induced resonance response introduced by the bigger bubbles in the population. Indeed, individual microbubble-assisted microvascular vasoactivity has been directly observed with high-speed cameras (e.g. [347]) and increased vascular permeability via populations of bubbles has been directly observed in real-time (e.g. [353]). Perhaps the most advanced application of this bioeffect is within the context of blood-brain-barrier opening in neuro-oncology applications [192], in which pre-clinical studies have confirmed that both microbubble composition [192] and size distribution [354,355] play a role on the resulting vascular permeability and ensuing vascular bioeffects.

4.4.5. Limitations

It is important here to consider some limitations of the current study. Firstly, we acknowledge that the confinement-dependent amplification effect on the induced resonance frequency needs further investigation. While this effect – whereby the radial vibration amplitude was larger when confined as compared to free-space in this induced frequency range – was observed for bubbles smaller than or equal to 2 μm in diameter (when adjacent to a 3 μm bubble), this response might depend on the relative size difference between bigger and smaller bubbles and not the actual size of the two-bubble companions. Secondly, we fixed the diameter and thickness of the vessel wall to create a controlled environment that focused on the effect of vessel viscosity. However, the effect of vessel wall thickness and diameter on the multi-bubble system can be a topic of interest for future studies,

including the investigation of bubble-to-wall distances. Thirdly, we fixed the inter-bubble spacing here to h =10 μm. Indeed, we previously confirmed that this bubble-to-bubble distance results in the coupling of vibration activities [318], but this distance will likely place a role on the magnitude of the effects observed here.

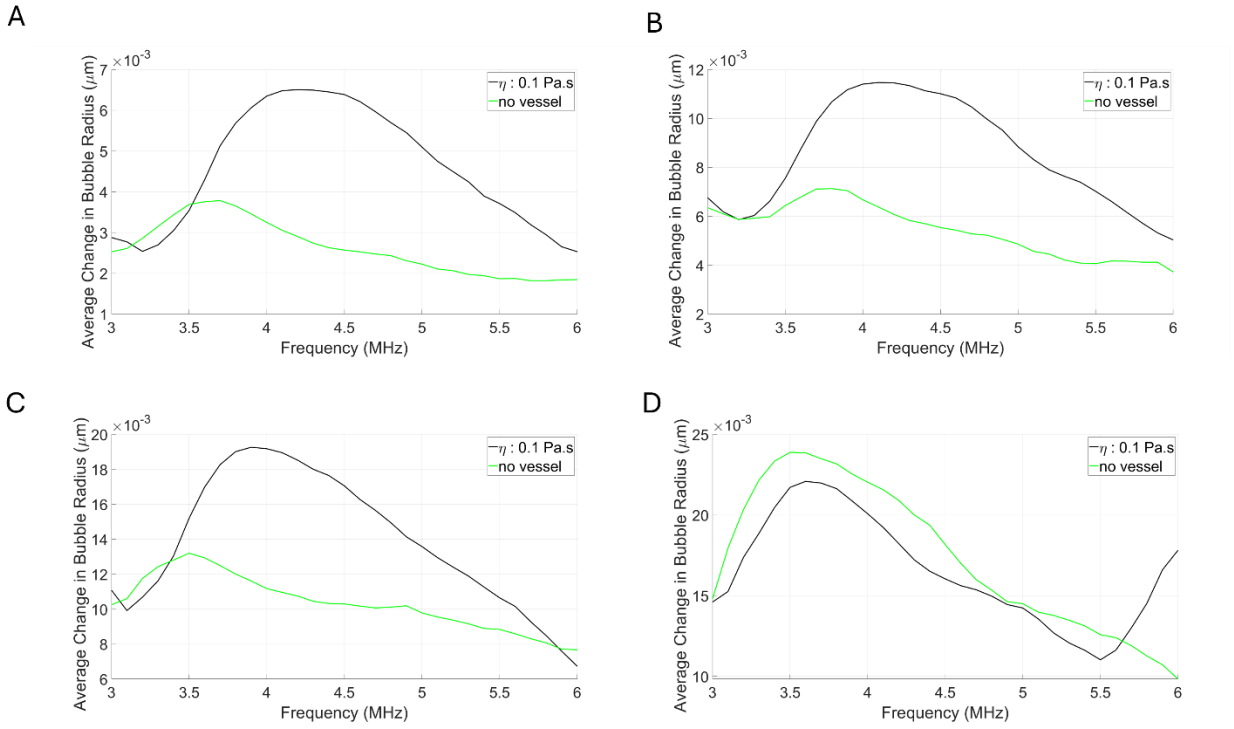

Figure 4.6. The induced resonance phenomenon persists for bubbles smaller than 2 μm. In these panels, a two-microbubble system is simulated in either free space (green trace) or within the lightly damped ($\eta = 0.1$ Pa·s) micro-vessel system (black trace). For all of these, the larger microbubble remains 3 μm, and we have depicted the resonance curve for a smaller companion microbubble of A) 1.5 μm, B) 1.75 μm, C) 2 μm bubble, and D) 2.25 μm. From these curves, it is clear that i) the induced resonance at ~ 4 MHz persists, which is the main resonance peak of the larger microbubble and ii) the response of the smaller bubble within confinement is larger in magnitude than its response in free space for bubbles ≤ 2 μm.

4.5. Conclusions

Here, we investigate the effect of micro-vessel viscosity on the response of a two-bubble system. The resonance response of the larger microbubble was unaffected by the presence of a neighboring,

smaller bubble, and its vibrational amplitude was attenuated over all transmit frequencies when placed inside a micro-vessel with increasing viscosity, as expected. However, the small bubble was highly influenced by its larger companion bubble, resulting in strong off-resonance activity at lower transmit frequencies. This induced resonance response resulted in larger amplitude vibrations when situated in a lightly damped micro-vessel (η=0.1 Pa·s) as compared to free-space. Further, the extent of vessel wall deformations mimicked that of the nearby, adjacent bubble. In light of the induced resonance on the smaller bubble, it becomes clear that both the two-microbubble system and vessel wall dynamics are dominated by the physics of the larger microbubble. These insights have significant implications for the applications of microbubble contrast agents, enhancing their effectiveness in medical applications of ultrasound contrast agents.

CRediT authorship contribution statement

Hossein Yusefi: Methodology, Software, Validation, Formal analysis, Investigation, Visualization.

Brandon Helfield: Conceptualization, Methodology, Validation, Formal analysis, Investigation, Visualization, Supervision, Funding acquisition.

Declaration of Competing Interest

None

Acknowledgments

This work was funded by the Natural Sciences and Engineering Research Council of Canada (NSERC; RGPIN-2019-06969). BH is a Burroughs Wellcome Fund Fellow (1018212.03).

Chapter 5. Conclusion and Future Outlook

The development of ultrasound contrast agents has expanded medical ultrasound applications and added new promising futures. Microbubbles are being approved and applied in various medical ultrasound fields, with many other new applications under development. Even though applications of MBs are expanding quickly and new features are being developed, there is still a need to gain more insight to fully understand all the behaviors that microbubbles exhibit. MBs are powerful tools with many capabilities, and understanding and predicting their behavior is critical to designing new applications, improving the current ones, and making them safer for medical ultrasound.

Within the ultrasound field, the behavior of microbubbles is influenced by a multitude of intrinsic and extrinsic variables. These include bubble size, shell type, gas core, boundaries, and fluid properties. The diverse range of variables, sizes, and the rapid vibration of microbubbles make studying a single bubble in a controlled laboratory setting challenging as it also necessitates the use of sophisticated instruments like ultra-fast imaging systems, making theoretical studies and simulations of microbubbles an attractive avenue. However, it is important to note that, while useful, theoretical studies of bubble physics only provide a partial representation of reality due to their inherent limitations and simplifications.

Many numerical analysis studies have been done on MBs, providing valuable results and insight into many aspects of bubble dynamics; however, most are focused on one characteristic or variable. This project aimed to further advance the numerical studies of bubble dynamics by simulating the bubble in an environment closer to reality using the knowledge of the field and software that gives

us more freedom. We used finite element modeling (FEM) to study bubbles in a realistic environment; we started with a simpler system and built upon it to mimic the real applications of MBs. Finally, in our last chapter and publication, we studied a bubble while vibrating inside a viscoelastic vessel and close to another bubble, considering fluid properties, bubble-bubble effect, bubble-vessel effect, and bubble deformation.

In chapter two, we studied how two bubbles affect each other while vibrating simultaneously. We study the system with different-sized MBs and in a range of frequencies and pressures from the resonance response perspective. We observed that in the system of two bubbles of the same size, we saw a frequency shift in resonance activity and a slight increase in amplitude. In the case of two bubbles of different sizes, we observed that the bigger bubble was almost unaffected by the smaller one. In comparison, the smaller bubble felt a big dampening effect in its original resonance response while showing off-resonance activities corresponding to the resonance response of the bigger bubble. This work shows that two bubbles can affect each other based on their initial size and how, in some situations, this effect is drastic.

In the third chapter, we study the same two bubble systems, focusing on bubbles' subharmonic activities and the effect of initial phospholipid packing, an important feature in manufacturing bubbles. We observed how different initial conditions of bubbles combined with the boundary effect can change the subharmonic response and cause amplitude variations as well as frequency shifts.

Finally, in our most recent work, we combined our previous works and studied a system of two bubbles vibrating inside a viscoelastic vessel, considering all boundary effects. We observed how a viscoelastic vessel dampens the bubble vibration amplitude and resonance response based on

vessel viscosity. We also showed that in a system of two different-sized bubbles, the bigger bubble induces a resonance activity on the smaller one, similar to our first work but affected by the vessel wall. In certain vessel wall viscosity, this induced resonance activity was further intensified.

This project sheds some light on how a MB interacts with its environment and how other bubbles and vessel walls affect it. It also provides some explanation for MBs' off-resonance activities. The results presented in this work on the complex dynamic of MBs' vibration have important implications for applications of MBs in imaging and therapy. This work can help guide the development of optimal contrast agents, can help in contrast image quantification, and can be used in developing specific pulse sequences to detect and diagnose disease.

The simulation environment created for this work can be further used to simulate MBs in even more complicated scenarios. Studying the effect of vessel size, blood flow beyond the vessel wall structure, or the translated fluid pressure over the vessel wall and in the cellular area is possible. Studying the effect of bubble vibration over the vessel wall makes it possible to assess the safety of using MBs in different situations.

References

[1] P.N.T. Wells, Physics and engineering: milestones in medicine, Med Eng Phys 23 (2001) 147–153.

[2] G. Ter Haar, Therapeutic ultrasound, European Journal of Ultrasound 9 (1999) 3–9. https://doi.org/10.1016/S0929-8266(99)00013-0.

[3] R. Gramiak, P.M. Shah, D.H. Kramer, Ultrasound Cardiography: Contrast Studies in Anatomy and Function, Radiology 92 (1969) 939–948. https://doi.org/10.1148/92.5.939.

[4] R. Gramiak, P.M. Shah, Echocardiography of the aortic root, Invest Radiol 3 (1968) 356–366.

[5] COMSOL Multiphysics® v. 5.6. www.comsol.com. COMSOL AB, Stockholm, Sweden., (n.d.).

[6] T.L. Szabo, Diagnostic Ultrasound Imaging: Inside and Out, 1st ed., Elsevier, London, UK, 2004.

[7] R.S.C. Cobbold, Chapter 5: Scattering of Ultrasound, (2013) 1–52.

[8] J.A. Jensen, Estimation of Blood Velocities Using Ultrasound: A Signal Processing Approach, Cambridge University Press, New York, 1996.

[9] F. Mone, F. McAuliffe, S. Ong, Clinical applications of Doppler ultrasound in obstetrics, The Obstetrician & Gynaecologist 11 (2019) 533–539. https://doi.org/10.1111/tog.12152.

[10] E.G. Grant, C.B. Benson, G.L. Moneta, A. V. Alexandrov, J.D. Baker, E.I. Bluth, B.A. Carroll, M. Eliasziw, J. Gocke, B.S. Hertzberg, S. Katanick, L. Needleman, J. Pellerito, J.F. Polak, K.S. Rholl, D.L. Wooster, E. Zierler, Carotid Artery Stenosis: Gray-Scale and Doppler US Diagnosis - Society of Radiologists in Ultrasound Consensus Conference, Radiology 229 (2003) 340–346. https://doi.org/10.1148/radiol.2292030516.

[11] M.A. Quiñones, C.M. Otto, M. Stoddard, A. Waggoner, W.A. Zoghbi, Recommendations for quantification of Doppler echocardiography: a report from the Doppler Quantification Task Force of the Nomenclature and Standards Committee of the American Society of Echocardiography., J Am Soc Echocardiogr 15 (2002) 167–184. https://doi.org/10.1067/mje.2002.120202.

[12] R.S.C. Cobbold, Foundations of Biomedical Ultrasound, Oxford Press, 2006.

[13] H. Becher, P.N. Burns, Left ventricular function and myocardial perfusion, Handbook of Contrast Echocardiography. New York, NY: Springer-Verlag New York (2000).

[14] H. Medwin, Counting bubbles acoustically : a review, Ultrasonics (1977) 7–13.

[15] E.C. Unger, T. Porter, W. Culp, R. Labell, T. Matsunaga, R. Zutshi, Therapeutic applications of lipid-coated microbubbles, Adv Drug Deliv Rev 56 (2004) 1291–1314.

[16] S. Garg, A.A. Thomas, M.A. Borden, The effect of lipid monolayer in-plane rigidity on in vivo microbubble circulation persistence, Biomaterials 34 (2013) 6862–6870. https://doi.org/10.1016/j.biomaterials.2013.05.053.

[17] S.R. Wilson, P.N. Burns, Microbubble-enhanced US in Body Imaging: What Role?, Radiology 257 (2010) 24–39. https://doi.org/10.1148/radiol.10091210.

[18] P.R. Muskula, M.L. Main, Safety with Echocardiographic Contrast Agents, Circ Cardiovasc Imaging 10 (2017) 1–9. https://doi.org/10.1161/CIRCIMAGING.116.005459.

[19] J.R. Laporte, F.J. de Latorre, A. Laszlo, G. Retsagi, D.A. Gadgil, D. V. Chandrasekhar, A. Lars, B.E. Wiholm, C. Martinez, D.W. Kaufman, T. Anderson, J.P. Kelly, S. Shapiro, Risk of anaphylaxis in a hospital population in relation to the use of various drugs: An international study, Pharmacoepidemiol Drug Saf 12 (2003) 195–202. https://doi.org/10.1002/pds.822.

[20] K.R. Beckett, A.K. Moriarity, J.M. Langer, Safe use of contrast media: What the radiologist needs to know, Radiographics 35 (2015) 1738–1750. https://doi.org/10.1148/rg.2015150033.

[21] T.J. Fraum, D.R. Ludwig, M.R. Bashir, K.J. Fowler, Gadolinium-based contrast agents: A comprehensive risk assessment, Journal of Magnetic Resonance Imaging 46 (2017) 338–353. https://doi.org/10.1002/jmri.25625.

[22] J.S. McDonald, C.H. Hunt, A.B. Kolbe, J.J. Schmitz, R.P. Hartman, D.E. Maddox, D.F. Kallmes, R.J. McDonald, Acute adverse events following gadolinium-based contrast agent administration: A single-center retrospective study of 281 945 injections, Radiology 292 (2019) 620–627. https://doi.org/10.1148/radiol.2019182834.

[23] P.N. Burns, Imaging Microbubbles in Children: A Light Foot on the Gas, Journal of Ultrasound in Medicine (2021) 1–2. https://doi.org/10.1002/jum.15656.

[24] T.R. Porter, F. Xie, Myocardial Perfusion Imaging With Contrast Ultrasound, JACC Cardiovasc Imaging 3 (2010) 176–187. https://doi.org/10.1016/j.jcmg.2009.09.024.

[25] R. Williams, J.M. Hudson, B.A. Lloyd, A.R. Sureshkumar, G. Lueck, L. Milot, M. Atri, G.A. Bjarnason, P.N. Burns, Dynamic Microbubble Contrast-enhanced US to Measure Tumor Response to Targeted Therapy: A Proposed Clinical Protocol with Results from Renal Cell Carcinoma Patients Receiving Antiangiogenic Therapy, Radiology 260 (2011) 581–590. https://doi.org/10.1148/radiol.11101893.

[26] J.E. Macioch, C.D. Katsamakis, J. Robin, P.R. Liebson, P.M. Meyer, C. Geohas, J.S. Raichlen, M.H. Davidson, S.B. Feinstein, Effect of contrast enhancement on measurement of carotid artery intimal medial thickness, Vascular Medicine 9 (2004) 7–12. https://doi.org/10.1191/1358863x04vm522oa.

[27] S.B. Feinstein, Contrast ultrasound imaging of the carotid artery vasa vasorum and atherosclerotic plaque neovascularization., J Am Coll Cardiol 48 (2006) 236–43. https://doi.org/10.1016/j.jacc.2006.02.068.

[28] K. Wei, E. Le, J.P. Bin, M. Coggins, J. Thorpe, S. Kaul, Quantification of renal blood flow with contrast-enhanced ultrasound., J Am Coll Cardiol 37 (2001) 1135–40.

[29] P.N. Burns, S.R. Wilson, D.H. Simpson, Pulse inversion imaging of liver blood flow: improved method for characterizing focal masses with microbubble contrast, Invest Radiol 35 (2000) 58.

[30] A. Sridharan, J.R. Eisenbrey, J.K. Dave, F. Forsberg, Quantitative nonlinear contrast-enhanced ultrasound of the breast, American Journal of Roentgenology 207 (2016) 274–281. https://doi.org/10.2214/AJR.16.16315.

[31] D. Robotti, T. Cammarota, P. Debani, A. Sarno, M. Astegiano, Activity of Crohn disease: Value of color-power-Doppler and contrast-enhanced ultrasonography, Abdom Imaging 29 (2004) 648–652. https://doi.org/10.1007/s00261-003-0157-0.

[32] T.J. D'Arcy, V. Jayaram, M. Lynch, W.P. Soutter, D.O. Cosgrove, C.J. Harvey, N. Patel, Ovarian cancer detected non-invasively by contrast-enhanced power Doppler ultrasound, BJOG 111 (2004) 619–622. https://doi.org/10.1111/j.1471-0528.2004.00157.x.

[33] E.J. Halpern, Contrast-enhanced ultrasound imaging of prostate cancer., Rev Urol 8 Suppl 1 (2006) S29-37.

[34] T.V. Bartolotta, M. Midiri, M. Galia, G. Runza, M. Attard, G. Savoia, R. Lagalla, A.E. Cardinale, Qualitative and quantitative evaluation of solitary thyroid nodules with contrast-enhanced ultrasound: Initial results, Eur Radiol 16 (2006) 2234–2241. https://doi.org/10.1007/s00330-006-0229-y.

[35] A.A. Doinikov, A. Bouakaz, Review of shell models for contrast agent microbubbles., IEEE Trans Ultrason Ferroelectr Freq Control 58 (2011) 981–993. https://doi.org/10.1109/TUFFC.2011.1899.

[36] D.E. Goertz, N. de Jong, A.F.W. van der Steen, Attenuation and size distribution measurements of Definity and manipulated Definity populations., Ultrasound Med Biol 33 (2007) 1376–1388. https://doi.org/10.1016/j.ultrasmedbio.2007.03.009.

[37] B.L. Helfield, X. Huo, R. Williams, D.E. Goertz, The effect of preactivation vial temperature on the acoustic properties of Definity™., Ultrasound Med Biol 38 (2012) 1298–305. https://doi.org/10.1016/j.ultrasmedbio.2012.03.005.

[38] J. Hyvelin, E. Gaud, M. Costa, A. Helbert, P. Bussat, T. Bettinger, P. Frinking, Characteristics and echogenicity of clinical ultrasound contrast agents: An in vitro and in vivo comparison study, Journal of Ultrasound in Medicine 36 (2017) 941–953.

[39] H. Shekhar, N.J. Smith, J.L. Raymond, C.K. Holland, Effect of temperature on the size distribution, shell properties, and stability of Definity®, Ultrasound Med Biol 44 (2018) 434–446.

[40] S. Stapleton, H. Goodman, Y.-Q. Zhou, E. Cherin, R.M. Henkelman, P.N. Burns, F.S. Foster, Acoustic and kinetic behaviour of definity in mice exposed to high frequency ultrasound., Ultrasound Med Biol 35 (2009) 296–307. https://doi.org/10.1016/j.ultrasmedbio.2008.08.010.

[41] T. Faez, D. Goertz, N. De Jong, Characterization of Definity™ ultrasound contrast agent at frequency range of 5-15 MHz., Ultrasound Med Biol 37 (2011) 338–42. https://doi.org/10.1016/j.ultrasmedbio.2010.11.014.

[42] M. Schneider, Sono Vue, a new ultrasound contrast agent, Eur Radiol 9 (1999) 347–348. https://doi.org/10.1007/pl00014071.

[43] J.-M. Gorce, M. Arditi, M. Schneider, Influence of bubble size distribution on the echogenicity of ultrasound contrast agents: A study of SonoVue™, Invest Radiol 35 (2000) 661–671.

[44] W.T. Shi, F. Forsberg, Ultrasonic characterization of the nonlinear properties of contrast microbubbles, Ultrasound Med Biol 26 (2000) 93–104.

[45] E. Stride, N. Saffari, Investigating the significance of multiple scattering in ultrasound contrast agent particle populations, IEEE Trans Ultrason Ferroelectr Freq Control 52 (2005) 2332–2345.

[46] P.C. Sontum, Physicochemical characteristics of Sonazoid™, a new contrast agent for ultrasound imaging, Ultrasound Med Biol 34 (2008) 824–833.

[47] K. Sarkar, W.T. Shi, D. Chatterjee, F. Forsberg, Characterization of ultrasound contrast microbubbles using in vitro experiments and viscous and viscoelastic interface models for encapsulation, J Acoust Soc Am 118 (2005) 539–550. https://doi.org/10.1121/1.1923367.

[48] T.G. Leighton, What is ultrasound?, Prog Biophys Mol Biol 93 (2007) 3–83. https://doi.org/10.1016/j.pbiomolbio.2006.07.026.

[49] H.G. Flynn, Cavitation dynamics: II. Free pulsations and models for cavitation bubbles, J Acoust Soc Am 58 (1975) 1160–1170. https://doi.org/10.1121/1.380799.

[50] R.E. Apfel, C.K. Holland, Gauging the likelihood of cavitation from short-pulse, low-duty cycle diagnostic ultrasound, Ultrasound Med Biol 17 (1991) 179–185. https://doi.org/10.1016/0301-5629(91)90125-G.

[51] S.L. Mulvagh, H. Rakowski, M.A. Vannan, S.S. Abdelmoneim, H. Becher, S.M. Bierig, P.N. Burns, R. Castello, P.D. Coon, M.E. Hagen, J.G. Jollis, T.R. Kimball, D.W. Kitzman, I. Kronzon, A.J. Labovitz, R.M. Lang, J. Mathew, W.S. Moir, S.F. Nagueh, A.S. Pearlman, J.E. Perez, T.R. Porter, J. Rosenbloom, G.M. Strachan, S. Thanigaraj, K. Wei, A. Woo, E.H.C. Yu, W.A. Zoghbi, American Society of Echocardiography Consensus Statement on the Clinical Applications of Ultrasonic Contrast Agents in Echocardiography, Journal of the American Society of Echocardiography 21 (2008) 1179–1201. https://doi.org/10.1016/j.echo.2008.09.009.

[52] J.Y. Lee, Y. Minami, B.I. Choi, W.J. Lee, Y.H. Chou, W.K. Jeong, M.S. Park, N. Kudo, M.W. Lee, K. Kamata, H. Iijima, S.Y. Kim, K. Numata, K. Sugimoto, H. Maruyama, Y. Sumino, C. Ogawa, M. Kitano, I. Joo, J. Arita, J. Der Liang, H.M. Lin, C. Nolsoe, O.H. Gilja, M. Kudo, The afsumb consensus statements and recommendations for the clinical practice of contrast-enhanced ultrasound using sonazoid, Ultrasonography 39 (2020) 191–220. https://doi.org/10.14366/usg.20057.

[53] C.F. Dietrich, C.P. Nolsoe, R.G. Barr, A. Berzigotti, P.N. Burns, V. Cantisani, M.C. Chammas, N. Chaubal, B.I. Choi, D.A. Clevert, X. Cui, Y. Dong, M. D'Onofrio, J.B. Fowlkes, O.H. Gilja, P. Huang, A. Ignee, C. Jenssen, Y. Kono, M. Kudo, N. Lassau, W.J. Lee, J.Y. Lee, P. Liang, A. Lim, A. Lyshchik, M.F. Meloni, J.M. Correas, Y. Minami, F.

Moriyasu, C. Nicolau, F. Piscaglia, A. Saftoiu, P.S. Sidhu, I. Sporea, G. Torzilli, X. Xie, R. Zheng, Guidelines and good clinical practice recommendations for contrast enhanced ultrasound (CEUS) in the liver - Update 2020 - WFUMB in cooperation with EFSUMB, AFSUMB, AIUM, and FLAUS, Ultraschall in Der Medizin 41 (2020) 562–585. https://doi.org/10.1055/a-1177-0530.

[54] J.M. Hudson, R. Karshafian, P.N. Burns, Quantification of flow using ultrasound and microbubbles: a disruption replenishment model based on physical principles., Ultrasound Med Biol 35 (2009) 2007–20. https://doi.org/10.1016/j.ultrasmedbio.2009.06.1102.

[55] K. Wei, a R. Jayaweera, S. Firoozan, a Linka, D.M. Skyba, S. Kaul, Quantification of myocardial blood flow with ultrasound-induced destruction of microbubbles administered as a constant venous infusion., Circulation 97 (1998) 473–483. https://doi.org/10.1161/01.CIR.97.5.473.

[56] J.E. Chomas, P. Dayton, D. May, K. Ferrara, Threshold of fragmentation for ultrasonic contrast agents., J Biomed Opt 6 (2001) 141–150. https://doi.org/10.1117/1.1352752.

[57] W.-S. Chen, T.J. Matula, A.A. Brayman, L.A. Crum, A comparison of the fragmentation thresholds and inertial cavitation doses of different ultrasound contrast agents, J Acoust Soc Am 113 (2003) 643–651. https://doi.org/10.1121/1.1529667.

[58] E. Sassaroli, K. Hynynen, Cavitation threshold of microbubbles in gel tunnels by focused ultrasound., Ultrasound Med Biol 33 (2007) 1651–1660. https://doi.org/10.1016/j.ultrasmedbio.2007.04.018.

[59] B. Helfield, J.J. Black, B. Qin, J. Pacella, X. Chen, F.S. Villanueva, Fluid Viscosity Affects the Fragmentation and Inertial Cavitation Threshold of Lipid-Encapsulated Microbubbles, Ultrasound Med Biol 42 (2016) 782–794. https://doi.org/10.1016/j.ultrasmedbio.2015.10.023.

[60] D. a King, M.J. Malloy, A.C. Roberts, A. Haak, C.C. Yoder, W.D. O'Brien, Determination of postexcitation thresholds for single ultrasound contrast agent microbubbles using double

passive cavitation detection., J Acoust Soc Am 127 (2010) 3449–55. https://doi.org/10.1121/1.3373405.

[61] M. Overvelde, V. Garbin, J. Sijl, B. Dollet, N. de Jong, D. Lohse, M. Versluis, Nonlinear shell behavior of phospholipid-coated microbubbles, Ultrasound Med Biol 36 (2010) 2080–2092. https://doi.org/10.1016/j.ultrasmedbio.2010.08.015.

[62] B.L. Helfield, D.E. Goertz, Nonlinear resonance behavior and linear shell estimates for Definity™ and MicroMarker™ assessed with acoustic microbubble spectroscopy., J Acoust Soc Am 133 (2013) 1158–1168. https://doi.org/10.1121/1.4774379.

[63] W. Lauterborn, Numerical investigation of nonlinear oscillations of gas bubbles in liquids, (1974) 283–293.

[64] J. Sijl, M. Overvelde, B. Dollet, V. Garbin, N. de Jong, D. Lohse, M. Versluis, "Compression-only" behavior: a second-order nonlinear response of ultrasound contrast agent microbubbles., J Acoust Soc Am 129 (2011) 1729–1739. https://doi.org/10.1121/1.3505116.

[65] N. de Jong, M. Emmer, C.T. Chin, A. Bouakaz, F. Mastik, D. Lohse, M. Versluis, "Compression-only" behavior of phospholipid-coated contrast bubbles., Ultrasound Med Biol 33 (2007) 653–656. https://doi.org/10.1016/j.ultrasmedbio.2006.09.016.

[66] A.A. Doinikov, J.F. Haac, P.A. Dayton, Resonance frequencies of lipid-shelled microbubbles in the regime of nonlinear oscillations., Ultrasonics 49 (2009) 263–268. https://doi.org/10.1016/j.ultras.2008.09.006.

[67] B.L. Helfield, B.Y.C. Leung, D.E. Goertz, The influence of compliant boundary proximity on the fundamental and subharmonic emissions from individual microbubbles, J Acoust Soc Am 136 (2014) EL40–EL46.

[68] G.A. Brock-Fisher, M.D. Poland, P.G. Rafter, Means for increasing sensitivity in non-linear ultrasound imaging systems, US5577505 A, 1996.

[69] P.J. Phillips, Contrast pulse sequences (CPS): Imaging nonlinear microbubbles, Proceedings of the IEEE Ultrasonics Symposium 2 (2001) 1739–1745. https://doi.org/10.1109/ultsym.2001.992057.

[70] M.A. Averkiou, M.F. Bruce, J.E. Powers, P.S. Sheeran, P.N. Burns, Imaging Methods for Ultrasound Contrast Agents, Ultrasound Med Biol 46 (2020) 498–517. https://doi.org/10.1016/j.ultrasmedbio.2019.11.004.

[71] C. Tremblay-Darveau, P.S. Sheeran, C.K. Vu, R. Williams, Z. Zhang, M. Bruce, P.N. Burns, The role of microbubble echo phase lag in multi-pulse contrast-enhanced ultrasound imaging, IEEE Trans Ultrason Ferroelectr Freq Control 65 (2018) 1389–1401. https://doi.org/10.1109/TUFFC.2018.2841848.

[72] J.R. Lindner, Microbubbles in medical imaging: Current applications and future directions, Nat Rev Drug Discov 3 (2004) 527–532. https://doi.org/10.1038/nrd1417.

[73] S.A.G. Langeveld, B. Meijlink, K. Kooiman, Phospholipid-coated targeted microbubbles for ultrasound molecular imaging and therapy, Curr Opin Chem Biol 63 (2021) 171–179. https://doi.org/10.1016/j.cbpa.2021.04.013.

[74] B. a Kaufmann, J.M. Sanders, C. Davis, A. Xie, P. Aldred, I.J. Sarembock, J.R. Lindner, Molecular imaging of inflammation in atherosclerosis with targeted ultrasound detection of vascular cell adhesion molecule-1., Circulation 116 (2007) 276–84. https://doi.org/10.1161/CIRCULATIONAHA.106.684738.

[75] J.K. Willmann, R.H. Kimura, N. Deshpande, A.M. Lutz, J.R. Cochran, S.S. Gambhir, Targeted contrast-enhanced ultrasound imaging of tumor angiogenesis with contrast microbubbles conjugated to integrin-binding knottin peptides., J Nucl Med 51 (2010) 433–40. https://doi.org/10.2967/jnumed.109.068007.

[76] A.J. Hamilton, S.-L. Huang, D. Warnick, M. Rabbat, B. Kane, A. Nagaraj, M. Klegerman, D.D. McPherson, Intravascular ultrasound molecular imaging of atheroma components in vivo., J Am Coll Cardiol 43 (2004) 453–60. https://doi.org/10.1016/j.jacc.2003.07.048.

[77] G.E.R. Weller, E. Lu, M.M. Csikari, A.L. Klibanov, D. Fischer, W.R. Wagner, F.S. Villanueva, Ultrasound imaging of acute cardiac transplant rejection with microbubbles targeted to intercellular adhesion molecule-1., Circulation 108 (2003) 218–24. https://doi.org/10.1161/01.CIR.0000080287.74762.60.

[78] D.B. Ellegala, H. Leong-Poi, J.E. Carpenter, A.L. Klibanov, S. Kaul, M.E. Shaffrey, J. Sklenar, J.R. Lindner, Imaging tumor angiogenesis with contrast ultrasound and microbubbles targeted to alpha(v)beta3., Circulation 108 (2003) 336–41. https://doi.org/10.1161/01.CIR.0000080326.15367.0C.

[79] T. Bettinger, P. Bussat, I. Tardy, S. Pochon, J.-M. Hyvelin, P. Emmel, S. Henrioud, N. Biolluz, J.K. Willmann, M. Schneider, F. Tranquart, Ultrasound molecular imaging contrast agent binding to both E- and P-selectin in different species., Invest Radiol 47 (2012) 516–23. https://doi.org/10.1097/RLI.0b013e31825cc605.

[80] J.K. Willmann, L. Bonomo, A.C. Testa, P. Rinaldi, G. Rindi, K.S. Valluru, G. Petrone, M. Martini, A.M. Lutz, S.S. Gambhir, Ultrasound molecular imaging with BR55 in patients with breast & ovarian lesions: First-in-human results, Journal of Clinical Oncology 35 (2017) 2133–2140. https://doi.org/10.1200/JCO.2016.70.8594.

[81] M. Smeenge, F. Tranquart, C.K. Mannaerts, T.M. De Reijke, M.J. Van De Vijver, M.P. Laguna, S. Pochon, J.J.M.C.H. De La Rosette, H. Wijkstra, First-in-human ultrasound molecular imaging with a VEGFR2-specific ultrasound molecular contrast agent (BR55) in prostate cancer a safety and feasibility pilot study, Invest Radiol 52 (2017) 419–427. https://doi.org/10.1097/RLI.0000000000000362.

[82] G. Korpanty, J.G. Carbon, P. a Grayburn, J.B. Fleming, R. a Brekken, Monitoring response to anticancer therapy by targeting microbubbles to tumor vasculature., Clin Cancer Res 13 (2007) 323–30. https://doi.org/10.1158/1078-0432.CCR-06-1313.

[83] S. Zhao, D.E. Kruse, K.W. Ferrara, P. a Dayton, Selective imaging of adherent targeted ultrasound contrast agents., Phys Med Biol 52 (2007) 2055–2072. https://doi.org/10.1088/0031-9155/52/8/002.

[84] B.L. Helfield, E. Cherin, F.S. Foster, D.E. Goertz, The effect of binding on the subharmonic emissions from individual lipid-encapsulated microbubbles at transmit frequencies of 11 and 25 MHz, Ultrasound Med Biol 39 (2013) 345–359.

[85] Y. Inaba, J.R. Lindner, Molecular imaging of disease with targeted contrast ultrasound imaging., Transl Res 159 (2012) 140–8. https://doi.org/10.1016/j.trsl.2011.12.001.

[86] A. Needles, O. Couture, F.S. Foster, A method for differentiating targeted microbubbles in real time using subharmonic micro-ultrasound and interframe filtering., Ultrasound Med Biol 35 (2009) 1564–73. https://doi.org/10.1016/j.ultrasmedbio.2009.04.006.

[87] S. Wang, C.Y. Wang, S. Unnikrishnan, A.L. Klibanov, J.A. Hossack, F.W. Mauldin, Optical Verification of Microbubble Response to Acoustic Radiation Force in Large Vessels With In Vivo Results, Invest Radiol 50 (2015) 772–784. https://doi.org/10.1097/RLI.0000000000000185.

[88] P.A. Dayton, K.E. Morgan, A.L. Klibanov, G. Brandenburger, K.R. Nightingale, K.W. Ferrara, A preliminary evaluation of the effects of primary and secondary radiation forces on acoustic contrast agents, IEEE Trans Ultrason Ferroelectr Freq Control 44 (1997) 1264–1277. https://doi.org/10.1109/58.656630.

[89] P. Dayton, A. Klibanov, G. Brandenburger, K. Ferrara, Acoustic radiation force in vivo: A mechanism to assist targeting of microbubbles, Ultrasound Med Biol 25 (1999) 1195–1201. https://doi.org/10.1016/S0301-5629(99)00062-9.

[90] S. Zhao, M. Borden, S.H. Bloch, D. Kruse, K.W. Ferrara, P.A. Dayton, Radiation-force assisted targeting facilitates ultrasonic molecular imaging, Mol Imaging 3 (2004) 135–148. https://doi.org/10.1162/1535350042380317.

[91] B.L. Helfield, A Review of Phospholipid-Coated Ultrasound Contrast Agent Microbubble Physics, Ultrasound Med Biol 45 (2019) 282–300.

[92] T. Hasegawa, K. Yosioka, Acoustic-Radiation Force on a Solid Elastic Sphere, Journal of the Acoustical Society of America 46 (1969) 1139–1145.

[93] L.A. Crum, Bjerknes forces on bubbles in a stationary sound field, Journal of the Acoustical Society of America 57 (1975) 1363–1370.

[94] J.J. Rychak, A.L. Klibanov, K.F. Ley, J. a Hossack, Enhanced targeting of ultrasound contrast agents using acoustic radiation force., Ultrasound Med Biol 33 (2007) 1132–9. https://doi.org/10.1016/j.ultrasmedbio.2007.01.005.

[95] P.J. a Frinking, I. Tardy, M. Théraulaz, M. Arditi, J. Powers, S. Pochon, F. Tranquart, Effects of acoustic radiation force on the binding efficiency of BR55, a VEGFR2-specific ultrasound contrast agent., Ultrasound Med Biol 38 (2012) 1460–9. https://doi.org/10.1016/j.ultrasmedbio.2012.03.018.

[96] S. Wang, F.W. Mauldin, A.L. Klibanov, J.A. Hossack, Ultrasound-Based Measurement of Molecular Marker Concentration in Large Blood Vessels: A Feasibility Study, Ultrasound Med Biol 41 (2015) 222–234. https://doi.org/10.1016/j.ultrasmedbio.2014.07.001.

[97] L. Abou-Elkacem, S. V. Bachawal, J.K. Willmann, Ultrasound molecular imaging: Moving toward clinical translation, Eur J Radiol 84 (2015) 1685–1693. https://doi.org/10.1016/j.ejrad.2015.03.016.

[98] Y. Matsumura, H. Maeda, A New Concept for Macromolecular Therapeutics in Cancer Chemotherapy: Mechanism of Tumoritropic Accumulation of Proteins and the Antitumor Agent Smancs, Cancer Res 46 (1986) 6387–6392.

[99] P.S. Sheeran, P.A. Dayton, Phase-change contrast agents for imaging and therapy, Curr Pharm Des 18 (2012) 2152–65. https://doi.org/10.2174/138161212800099883.

[100] B. Helfield, Y. Zou, N. Matsuura, Acoustically-Stimulated Nanobubbles : Opportunities in Medical Ultrasound Imaging and Therapy, Front Phys 9 (2021) 1–14. https://doi.org/10.3389/fphy.2021.654374.

[101] M.G. Shapiro, P.W. Goodwill, A. Neogy, M. Yin, F.S. Foster, D. V Schaffer, S.M. Conolly, Biogenic gas nanostructures as ultrasonic molecular reporters, Nat Nanotechnol 9 (2014) 311–316.

[102] J.A. Kopechek, K.J. Haworth, J.L. Raymond, T. Douglas Mast, S.R. Perrin, M.E. Klegerman, S. Huang, T.M. Porter, D.D. McPherson, C.K. Holland, Acoustic characterization of echogenic liposomes: Frequency-dependent attenuation and backscatter, J Acoust Soc Am 130 (2011) 3472–3481. https://doi.org/10.1121/1.3626124.

[103] J.J. Kwan, R. Myers, C.M. Coviello, S.M. Graham, A.R. Shah, E. Stride, R.C. Carlisle, C.C. Coussios, Ultrasound-Propelled Nanocups for Drug Delivery, Small 11 (2015) 5305–5314. https://doi.org/10.1002/smll.201501322.

[104] P.S. Sheeran, V.P. Wong, S. Luois, R.J. McFarland, W.D. Ross, S. Feingold, T.O. Matsunaga, P.A. Dayton, Decafluorobutane as a phase-change contrast agent for low-energy extravascular ultrasonic imaging, Ultrasound Med Biol 37 (2011) 1518–1530.

[105] P.S. Sheeran, K. Yoo, R. Williams, M. Yin, F.S. Foster, P.N. Burns, More Than Bubbles: Creating Phase-Shift Droplets from Commercially Available Ultrasound Contrast Agents, Ultrasound Med Biol 43 (2017) 531–540. https://doi.org/10.1016/j.ultrasmedbio.2016.09.003.

[106] S.A. Choudhury, F. Xie, S. Kutty, J. Lof, E. Stolze, T.R. Porter, Selective infarct zone imaging with intravenous acoustically activated droplets, PLoS One 13 (2018) 1–15. https://doi.org/10.1371/journal.pone.0207486.

[107] K.C. Schad, K. Hynynen, In vitro characterization of perfluorocarbon droplets for focused ultrasound therapy, Phys Med Biol 55 (2010) 4933–4947.

[108] O.D. Kripfgans, J.B. Fowlkes, D.L. Miller, O.P. Eldevik, P.L. Carson, Acoustic droplet vaporization for therapeutic and diagnostic applications, Ultrasound Med Biol 26 (2000) 1177–1189. https://doi.org/10.1016/S0301-5629(00)00262-3.

[109] B.L. Helfield, K. Yoo, J. Liu, R. Williams, P.S. Sheeran, D.E. Goertz, P.N. Burns, Investigating the Accumulation of Submicron Phase-Change Droplets in Tumors, Ultrasound Med Biol 46 (2020) 2861–2870. https://doi.org/10.1016/j.ultrasmedbio.2020.06.021.

[110] O. Shpak, M. Verweij, H.J. Vos, N. de Jong, D. Lohse, M. Versluis, Acoustic droplet vaporization is initiated by superharmonic focusing, Proceedings of the National Academy of Sciences 111 (2014) 1697–1702. https://doi.org/10.1073/pnas.1312171111.

[111] R. Williams, C. Wright, E. Cherin, N. Reznik, M. Lee, I. Gorelikov, F.S. Foster, N. Matsuura, P.N. Burns, Characterization of Submicron Phase-Change Perfluorocarbon Droplets for Extravascular Ultrasound Imaging of Cancer, Ultrasound Med Biol 39 (2013) 475–489.

[112] A.A. Exner, M.C. Kolios, Bursting microbubbles: How nanobubble contrast agents can enable the future of medical ultrasound molecular imaging and image-guided therapy, Curr Opin Colloid Interface Sci 54 (2021) 101463. https://doi.org/10.1016/j.cocis.2021.101463.

[113] C. Pellow, C. Acconcia, G. Zheng, D.E. Goertz, Threshold-dependent nonlinear scattering from porphyrin nanobubbles for vascular and extravascular applications, Phys Med Biol 63 (2018). https://doi.org/10.1088/1361-6560/aae571.

[114] R.H. Perera, H. Wu, P. Peiris, C. Hernandez, A. Burke, H. Zhang, A.A. Exner, Improving performance of nanoscale ultrasound contrast agents using N, N-diethylacrylamide stabilization, Nanomedicine 13 (2017) 59–67.

[115] C. Pellow, J. Tan, E. Chérin, C.E.M. Demore, G. Zheng, D.E. Goertz, High frequency ultrasound nonlinear scattering from porphyrin nanobubbles, Ultrasonics 110 (2021) 106245. https://doi.org/10.1016/j.ultras.2020.106245.

[116] C. Pellow, E.C. Abenojar, A.A. Exner, G. Zheng, D.E. Goertz, Concurrent visual and acoustic tracking of passive and active delivery of nanobubbles to tumors, Theranostics 10 (2020) 11690–11706. https://doi.org/10.7150/thno.51316.

[117] C. Pellow, M.A. O'Reilly, K. Hynynen, G. Zheng, D.E. Goertz, Simultaneous Intravital Optical and Acoustic Monitoring of Ultrasound-Triggered Nanobubble Generation and Extravasation, Nano Lett 20 (2020) 4512–4519. https://doi.org/10.1021/acs.nanolett.0c01310.

[118] A.E. Walsby, Gas vesicles, Microbiol Rev 58 (1994) 94–144. https://doi.org/10.1128/mmbr.58.1.94-144.1994.

[119] D. Maresca, A. Lakshmanan, M. Abedi, A. Bar-Zion, A. Farhadi, G.J. Lu, J.O. Szablowski, D. Wu, S. Yoo, M.G. Shapiro, Biomolecular ultrasound and sonogenetics, Annu Rev Chem Biomol Eng 9 (2018) 229–252. https://doi.org/10.1146/annurev-chembioeng-060817-084034.

[120] E. Cherin, J.M. Melis, R.W. Bourdeau, M. Yin, D.M. Kochmann, F.S. Foster, M.G. Shapiro, Acoustic Behavior of Halobacterium salinarum Gas Vesicles in the High-Frequency Range: Experiments and Modeling, Ultrasound Med Biol 43 (2017) 1016–1030. https://doi.org/10.1016/j.ultrasmedbio.2016.12.020.

[121] D. Maresca, A. Lakshmanan, A. Lee-Gosselin, J.M. Melis, Y.L. Ni, R.W. Bourdeau, D.M. Kochmann, M.G. Shapiro, Nonlinear ultrasound imaging of nanoscale acoustic biomolecules, Appl Phys Lett 110 (2017) 1–5. https://doi.org/10.1063/1.4976105.

[122] A. Lakshmanan, A. Farhadi, S.P. Nety, A. Lee-Gosselin, R.W. Bourdeau, D. Maresca, M.G. Shapiro, Molecular Engineering of Acoustic Protein Nanostructures, ACS Nano 10 (2016) 7314–7322. https://doi.org/10.1021/acsnano.6b03364.

[123] A. Lakshmanan, Z. Jin, S.P. Nety, D.P. Sawyer, A. Lee-Gosselin, D. Malounda, M.B. Swift, D. Maresca, M.G. Shapiro, Acoustic biosensors for ultrasound imaging of enzyme activity, Nat Chem Biol 16 (2020) 988–996. https://doi.org/10.1038/s41589-020-0591-0.

[124] A. Farhadi, G.H. Ho, D.P. Sawyer, R.W. Bourdeau, M.G. Shapiro, Ultrasound imaging of gene expression in mammalian cells, Science (1979) 365 (2019) 1469–1475. https://doi.org/10.1126/science.aax4804.

[125] A. Bouakaz, S. Frigstad, F.J. Ten Cate, N. de Jong, Super harmonic imaging: A new imaging technique for improved contrast detection, Ultrasound Med Biol 28 (2002) 59–68. https://doi.org/10.1016/S0301-5629(01)00460-4.

[126] P.L.M.J. van Neer, G. Matte, M.G. Danilouchkine, N. de Jong, C. Prins, F. van den Adel, Super-Harmonic Imaging: Development of an Interleaved Phased-Array Transducer, IEEE

Trans Ultrason Ferroelectr Freq Control 57 (2010) 455–468. https://doi.org/10.1109/TUFFC.2010.1426.

[127] D.E. Kruse, K.W. Ferrara, A new imaging strategy using wideband transient response of ultrasound contrast agents., IEEE Trans Ultrason Ferroelectr Freq Control 52 (2005) 1320–9.

[128] A. Guiroy, A. Novell, E. Ringgaard, R. Lou-Moeller, J.M. Grégoire, A.P. Abellard, T. Zawada, A. Bouakaz, F. Levassort, Dual-frequency transducer for nonlinear contrast agent imaging, IEEE Trans Ultrason Ferroelectr Freq Control 60 (2013) 2634–2644. https://doi.org/10.1109/TUFFC.2013.2862.

[129] R. Gessner, M. Lukacs, M. Lee, E. Cherin, F.S. Foster, P.A. Dayton, High-resolution, high-contrast ultrasound imaging using a prototype dual-frequency transducer: In vitro and in vivo studies, IEEE Trans Ultrason Ferroelectr Freq Control 57 (2010) 1772–1781. https://doi.org/10.1109/TUFFC.2010.1615.

[130] B. Lindsey, J. Rojas, K. Martin, S. Shelton, P. Dayton, Acoustic characterization of contrast-to-tissue ratio and axial resolution for dual-frequency contrast-specific acoustic angiography imaging, IEEE Trans Ultrason Ferroelectr Freq Control 61 (2014) 1668–1687. https://doi.org/10.1109/TUFFC.2014.006466.

[131] I.G. Newsome, P.A. Dayton, Visualization of Microvascular Angiogenesis Using Dual-Frequency Contrast-Enhanced Acoustic Angiography: A Review, Ultrasound Med Biol 46 (2020) 2625–2635. https://doi.org/10.1016/j.ultrasmedbio.2020.06.009.

[132] F. Lin, S.E. Shelton, D. Espíndola, J.D. Rojas, G. Pinton, P.A. Dayton, 3-D ultrasound localization microscopy for identifying microvascular morphology features of tumor angiogenesis at a resolution beyond the diffraction limit of conventional ultrasound, Theranostics 7 (2017) 196–204. https://doi.org/10.7150/thno.16899.

[133] S.E. Shelton, Y.Z. Lee, M. Lee, E. Cherin, F.S. Foster, S.R. Aylward, P.A. Dayton, Quantification of microvascular tortuosity during tumor evolution using acoustic

angiography, Ultrasound Med Biol 41 (2015) 1896–1904. https://doi.org/10.1016/j.ultrasmedbio.2015.02.012.

[134] J. Yang, E. Cherin, J. Yin, I.G. Newsome, T.M. Kierski, G. Pang, C.A. Carnevale, P.A. Dayton, F.S. Foster, C.E.M. Demore, Characterization of an Array-Based Dual-Frequency Transducer for Superharmonic Contrast Imaging, IEEE Trans Ultrason Ferroelectr Freq Control 68 (2021) 2419–2431. https://doi.org/10.1109/TUFFC.2021.3065952.

[135] I.G. Newsome, T.M. Kierski, G. Pang, J. Yin, J. Yang, E. Cherin, F.S. Foster, C.A. Carnevale, C.E.M. Demore, P.A. Dayton, Implementation of a Novel 288-Element Dual-Frequency Array for Acoustic Angiography: In Vitro and in Vivo Characterization, IEEE Trans Ultrason Ferroelectr Freq Control 68 (2021) 2657–2666. https://doi.org/10.1109/TUFFC.2021.3074025.

[136] J. Bosch, R.J. Groszmann, V.H. Shah, Evolution in the understanding of the pathophysiological basis of portal hypertension: How changes in paradigm are leading to successful new treatments, J Hepatol 62 (2015) S121–S130. https://doi.org/10.1016/j.jhep.2015.01.003.

[137] W.M. Fairbank, M.O. Scully, A New Noninvasive Technique for Cardiac Pressure Measurement: Resonant Scattering of Ultrasound from Bubbles, IEEE Trans Biomed Eng BME-24 (1977) 107–110. https://doi.org/10.1109/TBME.1977.326112.

[138] J.K. Dave, S. V. Kulkarni, P.P. Pangaonkar, M. Stanczak, M.E. McDonald, I.S. Cohen, P. Mehrotra, M.P. Savage, P. Walinsky, N.J. Ruggiero, D.L. Fischman, D. Ogilby, C. VanWhy, M. Lombardi, F. Forsberg, Non-Invasive Intra-cardiac Pressure Measurements Using Subharmonic-Aided Pressure Estimation: Proof of Concept in Humans, Ultrasound Med Biol 43 (2017) 2718–2724. https://doi.org/10.1016/j.ultrasmedbio.2017.07.009.

[139] C. Tremblay-Darveau, R. Williams, P.N. Burns, Measuring absolute blood pressure using microbubbles, Ultrasound Med Biol 40 (2014) 775–787. https://doi.org/10.1016/j.ultrasmedbio.2013.10.017.

[140] P.M. Shankar, P.D. Krishna, V.L. Newhouse, Subharmonic backscattering from ultrasound contrast agents., J Acoust Soc Am 106 (1999) 2104–10.

[141] F. Forsberg, J. Liu, W.T. Shi, J. Furuse, M. Shimizu, B.B. Goldberg, In vivo pressure estimation using subharmonic contrast microbubble signals: proof of concept, IEEE Trans Ultrason Ferroelectr Freq Control 52 (2005) 581–583.

[142] J.K. Dave, V.G. Halldorsdottir, J.R. Eisenbrey, D.A. Merton, J. Bin Liu, J.H. Zhou, H.K. Wang, S. Park, S. Dianis, C.L. Chalek, F. Lin, K.E. Thomenius, D.B. Brown, F. Forsberg, Investigating the Efficacy of Subharmonic Aided Pressure Estimation for Portal Vein Pressures and Portal Hypertension Monitoring, Ultrasound Med Biol 38 (2012) 1784–1798. https://doi.org/10.1016/j.ultrasmedbio.2012.06.013.

[143] V.G. Halldorsdottir, J.K. Dave, J.R. Eisenbrey, P. Machado, H. Zhao, J.B. Liu, D.A. Merton, F. Forsberg, Subharmonic aided pressure estimation for monitoring interstitial fluid pressure in tumours - In vitro and in vivo proof of concept, Ultrasonics 54 (2014) 1938–1944. https://doi.org/10.1016/j.ultras.2014.04.022.

[144] J.R. Eisenbrey, J.K. Dave, V.G. Halldorsdottir, D.A. Merton, C. Miller, J.M. Gonzalez, P. Machado, S. Park, S. Dianis, C.L. Chalek, C.E. Kim, J.P. Baliff, K.E. Thomenius, D.B. Brown, V. Navarro, F. Forsberg, Chronic Liver Disease: Noninvasive Subharmonic Aided Pressure Estimation of Hepatic Venous Pressure Gradient, Radiology 268 (2013) 581–588. https://doi.org/10.1148/radiol.13121769.

[145] L. Sandrin, S. Catheline, M. Tanter, X. Hennequin, M. Fink, Time-resolved pulsed elastography with ultrafast ultrasonic imaging, Ultrason Imaging 21 (1999) 259–272. https://doi.org/10.1177/016173469902100402.

[146] D. Maresca, M. Correia, O. Villemain, A. Bizé, L. Sambin, M. Tanter, B. Ghaleh, M. Pernot, Noninvasive Imaging of the Coronary Vasculature Using Ultrafast Ultrasound, JACC Cardiovasc Imaging 11 (2018) 798–808. https://doi.org/10.1016/j.jcmg.2017.05.021.

[147] C. Tremblay-Darveau, R. Williams, L. Milot, M. Bruce, P.N. Burns, Combined perfusion and doppler imaging using plane-wave nonlinear detection and microbubble contrast

agents, IEEE Trans Ultrason Ferroelectr Freq Control 61 (2014) 1988–2000. https://doi.org/10.1109/TUFFC.2014.006573.

[148] O. Couture, B. Besson, G. Montaldo, M. Fink, M. Tanter, Microbubble ultrasound super-localization imaging (MUSLI), IEEE International Ultrasonics Symposium, IUS (2011) 1285–1287. https://doi.org/10.1109/ULTSYM.2011.6293576.

[149] C. Errico, J. Pierre, S. Pezet, Y. Desailly, Z. Lenkei, O. Couture, M. Tanter, Ultrafast ultrasound localization microscopy for deep super-resolution vascular imaging, Nature 527 (2015) 499–502. https://doi.org/10.1038/nature16066.

[150] M.R. Lowerison, C. Huang, F. Lucien, S. Chen, P. Song, Ultrasound localization microscopy of renal tumor xenografts in chicken embryo is correlated to hypoxia, Sci Rep 10 (2020) 1–13. https://doi.org/10.1038/s41598-020-59338-z.

[151] M.A. O'Reilly, K. Hynynen, A super-resolution ultrasound method for brain vascular mapping, Med Phys 40 (2013) 1–7. https://doi.org/10.1118/1.4823762.

[152] K. Christensen-Jeffries, O. Couture, P.A. Dayton, Y.C. Eldar, K. Hynynen, F. Kiessling, M. O'Reilly, G.F. Pinton, G. Schmitz, M.X. Tang, M. Tanter, R.J.G. van Sloun, Super-resolution Ultrasound Imaging, Ultrasound Med Biol 46 (2020) 865–891. https://doi.org/10.1016/j.ultrasmedbio.2019.11.013.

[153] O. Couture, V. Hingot, B. Heiles, P. Muleki-Seya, M. Tanter, Ultrasound localization microscopy and super-resolution: A state of the art, IEEE Trans Ultrason Ferroelectr Freq Control 65 (2018) 1304–1320. https://doi.org/10.1109/TUFFC.2018.2850811.

[154] E. Betzig, G.H. Patterson, R. Sougrat, O.W. Lindwasser, S. Olenych, J.S. Bonifacino, M.W. Davidson, J. Lippincott-Schwartz, H.F. Hess, Imaging intracellular fluorescent proteins at nanometer resolution, Science (1979) 313 (2006) 1642–1645. https://doi.org/10.1126/science.1127344.

[155] M.J. Rust, M. Bates, X. Zhuang, Sub-diffraction-limit imaging by stochastic optical reconstruction microscopy (STORM), Nat Methods 3 (2006) 793–795. https://doi.org/10.1038/nmeth929.

[156] S.T. Hess, T.P.K. Girirajan, M.D. Mason, Ultra-high resolution imaging by fluorescence photoactivation localization microscopy, Biophys J 91 (2006) 4258–4272. https://doi.org/10.1529/biophysj.106.091116.

[157] O.M. Viessmann, R.J. Eckersley, K. Christensen-Jeffries, M.X. Tang, C. Dunsby, Acoustic super-resolution with ultrasound and microbubbles, Phys Med Biol 58 (2013) 6447–6458. https://doi.org/10.1088/0031-9155/58/18/6447.

[158] M. Siepmann, G. Schmitz, J. Bzyl, M. Palmowski, F. Kiessling, Imaging tumor vascularity by tracing single microbubbles, IEEE International Ultrasonics Symposium, IUS (2011) 1906–1908. https://doi.org/10.1109/ULTSYM.2011.0476.

[159] V. Hingot, C. Errico, M. Tanter, O. Couture, Subwavelength motion-correction for ultrafast ultrasound localization microscopy, Ultrasonics 77 (2017) 17–21. https://doi.org/10.1016/j.ultras.2017.01.008.

[160] J. Foiret, H. Zhang, T. Ilovitsh, L. Mahakian, S. Tam, K.W. Ferrara, Ultrasound localization microscopy to image and assess microvasculature in a rat kidney, Sci Rep 7 (2017) 1–12. https://doi.org/10.1038/s41598-017-13676-7.

[161] P. Song, J.D. Trzasko, A. Manduca, R. Huang, R. Kadirvel, D.F. Kallmes, S. Chen, Improved super-resolution ultrasound microvessel imaging with spatiotemporal nonlocal means filtering and bipartite graph-based microbubble tracking, IEEE International Ultrasonics Symposium, IUS 65 (2018) 149–167. https://doi.org/10.1109/ULTSYM.2017.8092824.

[162] B. Heiles, M. Correia, V. Hingot, M. Pernot, J. Provost, M. Tanter, O. Couture, Ultrafast 3D Ultrasound Localization Microscopy Using a 32 × 32 Matrix Array, IEEE Trans Med Imaging 38 (2019) 2005–2015. https://doi.org/10.1109/TMI.2018.2890358.

[163] Y. Desailly, A.M. Tissier, J.M. Correas, F. Wintzenrieth, M. Tanter, O. Couture, Contrast enhanced ultrasound by real-time spatiotemporal filtering of ultrafast images, Phys Med Biol 62 (2017) 31–42. https://doi.org/10.1088/1361-6560/62/1/31.

[164] K. Christensen-Jeffries, J. Brown, P. Aljabar, M. Tang, C. Dunsby, R.J. Eckersley, 3-D in Vitro Acoustic Super-Resolution and Super-Resolved Velocity Mapping Using Microbubbles, IEEE Trans Ultrason Ferroelectr Freq Control 64 (2017) 1478–1486. https://doi.org/10.1109/TUFFC.2017.2731664.

[165] K. Christensen-Jeffries, S. Harput, J. Brown, C. Dunsby, P. Aljabar, M.X. Tang, R. Eckersley, Microbubble axial localization errors in ultrasonic super-resolution imaging, IEEE International Ultrasonics Symposium, IUS 64 (2017) 1644–1654. https://doi.org/10.1109/ULTSYM.2017.8091846.

[166] C. Huang, M.R. Lowerison, J.D. Trzasko, A. Manduca, Y. Bresler, S. Tang, P. Gong, U.W. Lok, P. Song, S. Chen, Short Acquisition Time Super-Resolution Ultrasound Microvessel Imaging via Microbubble Separation, Sci Rep 10 (2020) 1–13. https://doi.org/10.1038/s41598-020-62898-9.

[167] U. Soylu, Y. Bresler, Circumventing the resolution-time tradeoff in Ultrasound Localization Microscopy by Velocity Filtering, (2021) 1–17.

[168] R.J.G. Van Sloun, O. Solomon, M. Bruce, Z.Z. Khaing, H. Wijkstra, Y.C. Eldar, M. Mischi, Super-Resolution Ultrasound Localization Microscopy through Deep Learning, IEEE Trans Med Imaging 40 (2021) 829–839. https://doi.org/10.1109/TMI.2020.3037790.

[169] D. Ackermann, G. Schmitz, Detection and tracking of multiple microbubbles in ultrasound B-mode images, IEEE Trans Ultrason Ferroelectr Freq Control 63 (2016) 72–82. https://doi.org/10.1109/TUFFC.2015.2500266.

[170] V. Hingot, C. Errico, B. Heiles, L. Rahal, M. Tanter, O. Couture, Microvascular flow dictates the compromise between spatial resolution and acquisition time in Ultrasound Localization Microscopy, Sci Rep 9 (2019) 1–10. https://doi.org/10.1038/s41598-018-38349-x.

[171] T. Opacic, S. Dencks, B. Theek, M. Piepenbrock, D. Ackermann, A. Rix, T. Lammers, E. Stickeler, S. Delorme, G. Schmitz, F. Kiessling, Motion model ultrasound localization

microscopy for preclinical and clinical multiparametric tumor characterization, Nat Commun 9 (2018) 1–13. https://doi.org/10.1038/s41467-018-03973-8.

[172] S. Harput, K. Christensen-Jeffries, J. Brown, Y. Li, K.J. Williams, A.H. Davies, R.J. Eckersley, C. Dunsby, M.X. Tang, Two-Stage Motion Correction for Super-Resolution Ultrasound Imaging in Human Lower Limb, IEEE Trans Ultrason Ferroelectr Freq Control 65 (2018) 803–814. https://doi.org/10.1109/TUFFC.2018.2824846.

[173] C. Huang, W. Zhang, P. Gong, U.W. Lok, S. Tang, T. Yin, X. Zhang, L. Zhu, M. Sang, P. Song, R. Zheng, S. Chen, Super-resolution ultrasound localization microscopy based on a high frame-rate clinical ultrasound scanner: An in-human feasibility study, Phys Med Biol 66 (2021). https://doi.org/10.1088/1361-6560/abef45.

[174] R.W. Wood, A.L. Loomis, The physical and biological effects of high-frequency sound-waves of great intensity, The London, Edinburgh, and Dublin Philosophical Magazine and Journal of Science 4 (1927) 417–436.

[175] B. Fowlkes, C.C. Abramowicz, Jacques S. Church, C.K. Holland, D.L. Miller, W.D. O'Brien, N.T. Sanghvi, M.E. Stratmeyer, J.F. Zachary, C.X. Deng, G.R. Harris, B.A. Herman, K. Hynynen, C. Merritt, K.E. Thomenius, M.R. Bailey, P.L. Carson, E.L. Carstensen, L.A. Frizzell, W.L. Nyborg, S.B. Barnett, F. Duck, P.D. Edmonds, M.C. Ziskin, J.G. Abbott, D. Dalecki, F. Dunn, J.F. Greenleaf, K.A. Salvesen, T.A. Siddiqi, M.A. Averkiou, A.A. Brayman, E.C. Everbach, J.H. Wible, J. Wu, D.G. Simpson, American institute of ultrasound in medicine consensus report on potential bioeffects of diagnostic ultrasound, American Institute of Ultrasound in Medicine 27 (2008) 503–515.

[176] G. ter Haar, C. Coussios, High intensity focused ultrasound: Physical principles and devices, International Journal of Hyperthermia 23 (2007) 89–104. https://doi.org/10.1080/02656730601186138.

[177] D.M. Skyba, R.J. Price, a Z. Linka, T.C. Skalak, S. Kaul, Direct in vivo visualization of intravascular destruction of microbubbles by ultrasound and its local effects on tissue., Circulation 98 (1998) 290–293. https://doi.org/10.1161/01.CIR.98.4.290.

[178] J. Blackmore, S. Shrivastava, J. Sallet, C.R. Butler, R.O. Cleveland, Ultrasound Neuromodulation: A Review of Results, Mechanisms and Safety, Ultrasound Med Biol 45 (2019) 1509–1536. https://doi.org/10.1016/j.ultrasmedbio.2018.12.015.

[179] K. Hynynen, V. Colucci, A. Chung, F. Jolesz, Noninvasive arterial occlusion using MRI-guided focused ultrasound, Ultrasound Med Biol 22 (1996) 1071–77.

[180] H. Chen, W. Kreider, A.A. Brayman, M.R. Bailey, T.J. Matula, Blood Vessel Deformations on Microsecond Time Scales by Ultrasonic Cavitation, Phys Rev Lett 106 (2011) 34301. https://doi.org/10.1103/PhysRevLett.106.034301.

[181] B. Helfield, X. Chen, S.C. Watkins, F.S. Villanueva, Biophysical insight into mechanisms of sonoporation, Proc Natl Acad Sci U S A 113 (2016) 9983–9988. https://doi.org/10.1073/pnas.1606915113.

[182] D.E. Goertz, M. Todorova, O. Mortazavi, V. Agache, B. Chen, R. Karshafian, K. Hynynen, Antitumor Effects of Combining Docetaxel (Taxotere) with the Antivascular Action of Ultrasound Stimulated Microbubbles, PLoS One 7 (2012). https://doi.org/10.1371/journal.pone.0052307.

[183] K. Hynynen, N. Mcdannold, N. Vykhodtseva, F.A. Jolesz, Noninvasive MR imaging–guided focal opening of the blood-brain barrier in rabbits, Radiology 220 (2001) 640–646.

[184] K. Hynynen, N. McDannold, N.A. Sheikov, F.A. Jolesz, N. Vykhodtseva, Local and reversible blood-brain barrier disruption by noninvasive focused ultrasound at frequencies suitable for trans-skull sonications., Neuroimage 24 (2005) 12–20. https://doi.org/10.1016/j.neuroimage.2004.06.046.

[185] D. Weber-Adrian, E. Thévenot, M.A. O'Reilly, W. Oakden, M.K. Akens, N. Ellens, K. Markham-Coultes, A. Burgess, J. Finkelstein, A.J.M. Yee, C.M. Whyne, K.D. Foust, B.K. Kaspar, G.J. Stanisz, R. Chopra, K. Hynynen, I. Aubert, Gene delivery to the spinal cord using MRI-guided focused ultrasound, Gene Ther 22 (2015) 568–577. https://doi.org/10.1038/gt.2015.25.

[186] M.A. O'Reilly, T. Chinnery, M.L. Yee, S.K. Wu, K. Hynynen, R.S. Kerbel, G.J. Czarnota, K.I. Pritchard, A. Sahgal, Preliminary Investigation of Focused Ultrasound-Facilitated Drug Delivery for the Treatment of Leptomeningeal Metastases, Sci Rep 8 (2018) 1–8. https://doi.org/10.1038/s41598-018-27335-y.

[187] A. Carpentier, M. Canney, A. Vignot, V. Reina, K. Beccaria, C. Horodyckid, C. Karachi, D. Leclercq, C. Lafon, J.-Y. Chapelon, L. Capelle, P. Cornu, M. Sanson, K. Hoang-Xuan, J.-Y. Delattre, A. Idbaih, Clinical trial of blood-brain barrier disruption by pulsed ultrasound, Sci Transl Med 8 (2016) 1–7. https://doi.org/10.1126/scitranslmed.aaf6086.

[188] S.H. Park, M.J. Kim, H.H. Jung, W.S. Chang, H.S. Choi, I. Rachmilevitch, E. Zadicario, J.W. Chang, Safety and feasibility of multiple blood-brain barrier disruptions for the treatment of glioblastoma in patients undergoing standard adjuvant chemotherapy, J Neurosurg 134 (2021) 475–483. https://doi.org/10.3171/2019.10.JNS192206.

[189] T. Mainprize, N. Lipsman, Y. Huang, Y. Meng, A. Bethune, S. Ironside, C. Heyn, R. Alkins, M. Trudeau, A. Sahgal, J. Perry, K. Hynynen, Blood-Brain Barrier Opening in Primary Brain Tumors with Non-invasive MR-Guided Focused Ultrasound: A Clinical Safety and Feasibility Study, Sci Rep 9 (2019) 1–7. https://doi.org/10.1038/s41598-018-36340-0.

[190] N. Lipsman, Y. Meng, A.J. Bethune, Y. Huang, B. Lam, M. Masellis, N. Herrmann, C. Heyn, I. Aubert, A. Boutet, G.S. Smith, K. Hynynen, S.E. Black, Blood–brain barrier opening in Alzheimer's disease using MR-guided focused ultrasound, Nat Commun 9 (2018) 2336. https://doi.org/10.1038/s41467-018-04529-6.

[191] A. Abrahao, Y. Meng, M. Llinas, Y. Huang, C. Hamani, T. Mainprize, I. Aubert, C. Heyn, S.E. Black, K. Hynynen, N. Lipsman, L. Zinman, First-in-human trial of blood-brain barrier opening in amyotrophic lateral sclerosis using MR-guided focused ultrasound, Nat Commun 10 (2019) 1–9. https://doi.org/10.1038/s41467-019-12426-9.

[192] R.M. Jones, D. McMahon, K. Hynynen, Ultrafast three-dimensional microbubble imaging in vivo predicts tissue damage volume distributions during nonthermal brain ablation, Theranostics 10 (2020) 7211–7230. https://doi.org/10.7150/thno.47281.

[193] J. Sijl, H.J. Vos, T. Rozendal, N. de Jong, D. Lohse, M. Versluis, Combined optical and acoustical detection of single microbubble dynamics., J Acoust Soc Am 130 (2011) 3271–3281. https://doi.org/10.1121/1.3626155.

[194] R. V. Shohet, S. Chen, Y.-T. Zhou, Z. Wang, R.S. Meidell, R.H. Unger, P. a. Grayburn, Echocardiographic Destruction of Albumin Microbubbles Directs Gene Delivery to the Myocardium, Circulation 101 (2000) 2554–2556. https://doi.org/10.1161/01.CIR.101.22.2554.

[195] H. Leong-Poi, M. a. Kuliszewski, M. Lekas, M. Sibbald, K. Teichert-Kuliszewska, A.L. Klibanov, D.J. Stewart, J.R. Lindner, Therapeutic arteriogenesis by ultrasound-mediated VEGF165 plasmid gene delivery to chronically ischemic skeletal muscle, Circ Res 101 (2007) 295–303. https://doi.org/10.1161/CIRCRESAHA.107.148676.

[196] W. Mathias, J.M. Tsutsui, B.G. Tavares, F. Xie, M.O.D. Aguiar, D.R. Garcia, M.T. Oliveira, A. Soeiro, J.C. Nicolau, P.A. Lemos, C.E. Rochitte, R. Kalil, T.R. Porter, Diagnostic Ultrasound Impulses Improve Microvascular Flow in Patients With STEMI Receiving Intravenous Microbubbles, J Am Coll Cardiol 67 (2016) 2506–2515. https://doi.org/10.1016/j.jacc.2016.03.542.

[197] N. McDannold, N. Vykhodtseva, K. Hynynen, Targeted disruption of the blood-brain barrier with focused ultrasound: association with cavitation activity., Phys Med Biol 51 (2006) 793–807. https://doi.org/10.1088/0031-9155/51/4/003.

[198] Y.S. Tung, F. Vlachos, J.J. Choi, T. Deffieux, K. Selert, E.E. Konofagou, In vivo transcranial cavitation threshold detection during ultrasound-induced blood-brain barrier opening in mice, Phys Med Biol 55 (2010) 6141–6155. https://doi.org/10.1088/0031-9155/55/20/007.

[199] J.A. Kopechek, A.R. Carson, C.F. McTiernan, X. Chen, E.C. Klein, F.S. Villanueva, Cardiac gene expression knockdown using small inhibitory RNA-loaded microbubbles and ultrasound, PLoS One 11 (2016) 1–12. https://doi.org/10.1371/journal.pone.0159751.

[200] J.J. Choi, R.C. Carlisle, C. Coviello, L. Seymour, C.C. Coussios, Non-invasive and real-time passive acoustic mapping of ultrasound-mediated drug delivery, Phys Med Biol 59 (2014) 4861–4877. https://doi.org/10.1088/0031-9155/59/17/4861.

[201] M.A. O'Reilly, K. Hynynen, Real-time feedback-controlled focused ultrasound disruption by using an acoustic emissions – based controller, Radiology 263 (2012) 96–106.

[202] C. Bing, Y. Hong, C. Hernandez, M. Rich, B. Cheng, I. Munaweera, D. Szczepanski, Y. Xi, M. Bolding, A. Exner, R. Chopra, Characterization of different bubble formulations for blood-brain barrier opening using a focused ultrasound system with acoustic feedback control, Sci Rep 8 (2018) 1–12. https://doi.org/10.1038/s41598-018-26330-7.

[203] C.D. Arvanitis, M.S. Livingstone, N. Vykhodtseva, N. McDannold, Controlled Ultrasound-Induced Blood-Brain Barrier Disruption Using Passive Acoustic Emissions Monitoring, PLoS One 7 (2012). https://doi.org/10.1371/journal.pone.0045783.

[204] T. Sun, Y. Zhang, C. Power, P.M. Alexander, J.T. Sutton, M. Aryal, N. Vykhodtseva, E.L. Miller, N.J. McDannold, Closed-loop control of targeted ultrasound drug delivery across the blood–brain/tumor barriers in a rat glioma model, Proceedings of the National Academy of Sciences 114 (2017) E10281–E10290. https://doi.org/10.1073/pnas.1713328114.

[205] H.A.S. Kamimura, J. Flament, J. Valette, A. Cafarelli, R. Aron Badin, P. Hantraye, B. Larrat, Feedback control of microbubble cavitation for ultrasound-mediated blood–brain barrier disruption in non-human primates under magnetic resonance guidance, Journal of Cerebral Blood Flow and Metabolism 39 (2019) 1191–1203. https://doi.org/10.1177/0271678X17753514.

[206] C. Peng, J.Q. Trojanowski, V.M.-Y. Lee, Protein transmission in neurodegenerative disease, Nat Rev Neurol 16 (2020) 199–212. https://doi.org/10.1038/s41582-020-0333-7.

[207] M.S. Forman, J.Q. Trojanowski, V.M.Y. Lee, Neurodegenerative diseases: a decade of discoveries paves the way for therapeutic breakthroughs, Nat Med 10 (2004) 1055–1063.

[208] A.C. Correia, A.R. Monteiro, R. Silva, J.N. Moreira, J.M. Sousa Lobo, A.C. Silva, Lipid nanoparticles strategies to modify pharmacokinetics of central nervous system targeting

drugs: Crossing or circumventing the blood–brain barrier (BBB) to manage neurological disorders, Adv Drug Deliv Rev 189 (2022) 114485. https://doi.org/https://doi.org/10.1016/j.addr.2022.114485.

[209] C.M. Gorick, V.R. Breza, K.M. Nowak, V.W.T. Cheng, D.G. Fisher, A.C. Debski, M.R. Hoch, Z.E.F. Demir, N.M. Tran, M.R. Schwartz, N.D. Sheybani, R.J. Price, Applications of focused ultrasound-mediated blood-brain barrier opening, Adv Drug Deliv Rev 191 (2022) 114583. https://doi.org/https://doi.org/10.1016/j.addr.2022.114583.

[210] W.M. Pardridge, Why is the global CNS pharmaceutical market so under-penetrated?, Drug Discov Today 7 (2002) 5–7. https://doi.org/https://doi.org/10.1016/S1359-6446(01)02082-7.

[211] K.F. Timbie, B.P. Mead, R.J. Price, Drug and gene delivery across the blood–brain barrier with focused ultrasound, Journal of Controlled Release 219 (2015) 61–75. https://doi.org/https://doi.org/10.1016/j.jconrel.2015.08.059.

[212] D.R. Groothuis, The blood-brain and blood-tumor barriers: a review of strategies for increasing drug delivery, Neuro Oncol 2 (2000) 45–59.

[213] R.H. Bobo, D.W. Laske, A. Akbasak, P.F. Morrison, R.L. Dedrick, E.H. Oldfield, Convection-enhanced delivery of macromolecules in the brain., Proceedings of the National Academy of Sciences 91 (1994) 2076–2080. https://doi.org/10.1073/pnas.91.6.2076.

[214] E.S. Smith, J.E. Porterfield, R.M. Kannan, Leveraging the interplay of nanotechnology and neuroscience: Designing new avenues for treating central nervous system disorders, Adv Drug Deliv Rev 148 (2019) 181–203. https://doi.org/https://doi.org/10.1016/j.addr.2019.02.009.

[215] Y. Chen, L. Liu, Modern methods for delivery of drugs across the blood–brain barrier, Adv Drug Deliv Rev 64 (2012) 640–665. https://doi.org/https://doi.org/10.1016/j.addr.2011.11.010.

[216] P. Zhao, T. Wu, Y. Tian, J. You, X. Cui, Recent advances of focused ultrasound induced blood-brain barrier opening for clinical applications of neurodegenerative diseases, Adv Drug Deliv Rev 209 (2024) 115323. https://doi.org/10.1016/j.addr.2024.115323.

[217] K. Hynynen, N. McDannold, N. Vykhodtseva, F.A. Jolesz, Noninvasive MR imaging-guided focal opening of the blood-brain barrier in rabbits, Radiology 220 (2001) 640–646.

[218] M. Aryal, C.D. Arvanitis, P.M. Alexander, N. McDannold, Ultrasound-mediated blood–brain barrier disruption for targeted drug delivery in the central nervous system, Adv Drug Deliv Rev 72 (2014) 94–109. https://doi.org/https://doi.org/10.1016/j.addr.2014.01.008.

[219] C. Brighi, E. Salimova, M. de Veer, S. Puttick, G. Egan, Translation of focused ultrasound for blood-brain barrier opening in glioma, Journal of Controlled Release 345 (2022) 443–463. https://doi.org/https://doi.org/10.1016/j.jconrel.2022.03.035.

[220] A. Dasgupta, M. Liu, T. Ojha, G. Storm, F. Kiessling, T. Lammers, Ultrasound-mediated drug delivery to the brain: principles, progress and prospects, Drug Discov Today Technol 20 (2016) 41–48. https://doi.org/https://doi.org/10.1016/j.ddtec.2016.07.007.

[221] S.R. Sirsi, M.A. Borden, State-of-the-art materials for ultrasound-triggered drug delivery, Adv Drug Deliv Rev 72 (2014) 3–14. https://doi.org/https://doi.org/10.1016/j.addr.2013.12.010.

[222] C.X. Deng, F. Sieling, H. Pan, J. Cui, Ultrasound-induced cell membrane porosity, Ultrasound Med Biol 30 (2004) 519–526. https://doi.org/https://doi.org/10.1016/j.ultrasmedbio.2004.01.005.

[223] C.C. Coussios, R.A. Roy, Applications of acoustics and cavitation to noninvasive therapy and drug delivery, Annu. Rev. Fluid Mech. 40 (2008) 395–420.

[224] S. Son, J.H. Kim, X. Wang, C. Zhang, S.A. Yoon, J. Shin, A. Sharma, M.H. Lee, L. Cheng, J. Wu, Multifunctional sonosensitizers in sonodynamic cancer therapy, Chem Soc Rev 49 (2020) 3244–3261.

[225] A. Association, 2018 Alzheimer's disease facts and figures, Alzheimer's and Dementia 14 (2018) 367–429. https://doi.org/10.1016/j.jalz.2018.02.001.

[226] C. Li, J. Götz, Tau-based therapies in neurodegeneration: opportunities and challenges, Nat Rev Drug Discov 16 (2017) 863–883.

[227] S. Dubey, S. Heinen, S. Krantic, J. McLaurin, D.R. Branch, K. Hynynen, I. Aubert, Clinically approved IVIg delivered to the hippocampus with focused ultrasound promotes neurogenesis in a model of Alzheimer's disease, Proceedings of the National Academy of Sciences 117 (2020) 32691–32700.

[228] G. Leinenga, W.K. Koh, J. Götz, A comparative study of the effects of Aducanumab and scanning ultrasound on amyloid plaques and behavior in the APP23 mouse model of Alzheimer disease, Alzheimers Res Ther 13 (2021) 1–14.

[229] P.W. Janowicz, G. Leinenga, J. Götz, R.M. Nisbet, Ultrasound-mediated blood-brain barrier opening enhances delivery of therapeutically relevant formats of a tau-specific antibody, Sci Rep 9 (2019) 9255.

[230] Y. Meng, K. Hynynen, N. Lipsman, Applications of focused ultrasound in the brain: from thermoablation to drug delivery, Nat Rev Neurol 17 (2021) 7–22.

[231] W. Poewe, K. Seppi, C.M. Tanner, G.M. Halliday, P. Brundin, J. Volkmann, A.-E. Schrag, A.E. Lang, Parkinson disease, Nat Rev Dis Primers 3 (2017) 1–21.

[232] C.-H. Fan, C.-Y. Lin, H.-L. Liu, C.-K. Yeh, Ultrasound targeted CNS gene delivery for Parkinson's disease treatment, Journal of Controlled Release 261 (2017) 246–262. https://doi.org/https://doi.org/10.1016/j.jconrel.2017.07.004.

[233] M.D. Yahr, R.C. Duvoisin, M.J. Schear, R.E. Barrett, M.M. Hoehn, Treatment of parkinsonism with levodopa, Arch Neurol 21 (1969) 343–354.

[234] S.S. Gill, N.K. Patel, G.R. Hotton, K. O'Sullivan, R. McCarter, M. Bunnage, D.J. Brooks, C.N. Svendsen, P. Heywood, Direct brain infusion of glial cell line–derived neurotrophic factor in Parkinson disease, Nat Med 9 (2003) 589–595.

[235] C.-Y. Lin, H.-Y. Hsieh, C.-M. Chen, S.-R. Wu, C.-H. Tsai, C.-Y. Huang, M.-Y. Hua, K.-C. Wei, C.-K. Yeh, H.-L. Liu, Non-invasive, neuron-specific gene therapy by focused ultrasound-induced blood-brain barrier opening in Parkinson's disease mouse model, Journal of Controlled Release 235 (2016) 72–81.

[236] R. Stupp, W.P. Mason, M.J. Van Den Bent, M. Weller, B. Fisher, M.J.B. Taphoorn, K. Belanger, A.A. Brandes, C. Marosi, U. Bogdahn, Radiotherapy plus concomitant and adjuvant temozolomide for glioblastoma, New England Journal of Medicine 352 (2005) 987–996.

[237] M. Aryal, N. Vykhodtseva, Y.-Z. Zhang, N. McDannold, Multiple sessions of liposomal doxorubicin delivery via focused ultrasound mediated blood–brain barrier disruption: a safety study, Journal of Controlled Release 204 (2015) 60–69.

[238] M. Kinoshita, N. McDannold, F.A. Jolesz, K. Hynynen, Noninvasive localized delivery of Herceptin to the mouse brain by MRI-guided focused ultrasound-induced blood–brain barrier disruption, Proceedings of the National Academy of Sciences 103 (2006) 11719–11723.

[239] G. Shakya, M. Cattaneo, G. Guerriero, A. Prasanna, S. Fiorini, O. Supponen, Ultrasound-responsive microbubbles and nanodroplets: A pathway to targeted drug delivery, Adv Drug Deliv Rev 206 (2024) 115178. https://doi.org/10.1016/j.addr.2023.115178.

[240] H. Mulvana, R.J. Browning, Y. Luan, N. de Jong, M.-X. Tang, R.J. Eckersley, E. Stride, Characterization of Contrast Agent Microbubbles for Ultrasound Imaging and Therapy Research, IEEE Trans Ultrason Ferroelectr Freq Control 64 (2017) 232–251. https://doi.org/10.1109/TUFFC.2016.2613991.

[241] S. V Morse, A. Mishra, T.G. Chan, R. T. M. de Rosales, J.J. Choi, Liposome delivery to the brain with rapid short-pulses of focused ultrasound and microbubbles, Journal of Controlled Release 341 (2022) 605–615. https://doi.org/https://doi.org/10.1016/j.jconrel.2021.12.005.

[242] S.R. Sirsi, C. Fung, S. Garg, M.Y. Tianning, P.A. Mountford, M.A. Borden, Lung Surfactant Microbubbles Increase Lipophilic Drug Payload for Ultrasound-Targeted Delivery, Theranostics 3 (2013) 409–419. https://doi.org/10.7150/thno.5616.

[243] M. Bezagu, J. Clarhaut, B. Renoux, F. Monti, M. Tanter, P. Tabeling, J. Cossy, O. Couture, S. Papot, S. Arseniyadis, In situ targeted activation of an anticancer agent using ultrasound-triggered release of composite droplets, Eur J Med Chem 142 (2017) 2–7. https://doi.org/https://doi.org/10.1016/j.ejmech.2017.03.057.

[244] Z. Tie, S. Zhang, Y. Qu, M. Wang, R. Liu, D. Sun, Z. Dai, Advances in microbubble-assisted ultrasound-guided gene therapy: Mechanisms and applications, Sci China Mater (2024) 1–18. https://doi.org/10.1007/s40843-024-2993-4.

[245] I. De Cock, G. Lajoinie, M. Versluis, S.C. De Smedt, I. Lentacker, Sonoprinting and the importance of microbubble loading for the ultrasound mediated cellular delivery of nanoparticles, Biomaterials 83 (2016) 294–307. https://doi.org/https://doi.org/10.1016/j.biomaterials.2016.01.022.

[246] B. Tayier, Z. Deng, Y. Wang, W. Wang, Y. Mu, F. Yan, Biosynthetic nanobubbles for targeted gene delivery by focused ultrasound, Nanoscale 11 (2019) 14757–14768. https://doi.org/10.1039/C9NR03402A.

[247] W. Rui, W. Lufang, C. Yihan, X. Yuji, H. Mengrong, Z. Ye, X. Lingling, H. Zhengyang, C. Dandan, J. Qiaofeng, Z. Li, X. Mingxing, Biogenic Gas Vesicles for Ultrasound Imaging and Targeted Therapeutics, Curr Med Chem 29 (2022) 1316–1330. https://doi.org/http://dx.doi.org/10.2174/0929867328666210705145642.

[248] L. Xie, J. Wang, L. Song, T. Jiang, F. Yan, Cell-cycle dependent nuclear gene delivery enhances the effects of E-cadherin against tumor invasion and metastasis, Signal Transduct Target Ther 8 (2023) 182. https://doi.org/10.1038/s41392-023-01398-4.

[249] S. He, D. Singh, H. Yusefi, B. Helfield, Stable Cavitation-Mediated Delivery of miR-126 to Endothelial Cells, Pharmaceutics 14 (2022). https://doi.org/10.3390/pharmaceutics14122656.

[250] R. Rupaimoole, F.J. Slack, MicroRNA therapeutics: towards a new era for the management of cancer and other diseases, Nat Rev Drug Discov 16 (2017) 203–222. https://doi.org/10.1038/nrd.2016.246.

[251] M. Rawat, K. Kadian, Y. Gupta, A. Kumar, P.S.G. Chain, O. Kovbasnjuk, S. Kumar, G. Parasher, MicroRNA in Pancreatic Cancer: From Biology to Therapeutic Potential, Genes (Basel) 10 (2019). https://doi.org/10.3390/genes10100752.

[252] S. Imani, R.-C. Wu, J. Fu, MicroRNA-34 family in breast cancer: from research to therapeutic potential, J Cancer 9 (2018) 3765.

[253] V. Balatti, C.M. Croce, MicroRNA dysregulation and multi-targeted therapy for cancer treatment, Adv Biol Regul 75 (2020) 100669. https://doi.org/https://doi.org/10.1016/j.jbior.2019.100669.

[254] S. Snipstad, S. Berg, Ý. Mørch, A. Bjørkøy, E. Sulheim, R. Hansen, I. Grimstad, A. van Wamel, A.F. Maaland, S.H. Torp, Ultrasound improves the delivery and therapeutic effect of nanoparticle-stabilized microbubbles in breast cancer xenografts, Ultrasound Med Biol 43 (2017) 2651–2669.

[255] F. Yan, L. Li, Z. Deng, Q. Jin, J. Chen, W. Yang, C.-K. Yeh, J. Wu, R. Shandas, X. Liu, H. Zheng, Paclitaxel-liposome–microbubble complexes as ultrasound-triggered therapeutic drug delivery carriers, Journal of Controlled Release 166 (2013) 246–255. https://doi.org/https://doi.org/10.1016/j.jconrel.2012.12.025.

[256] T.-Y. Wang, J.W. Choe, K. Pu, R. Devulapally, S. Bachawal, S. Machtaler, S.M. Chowdhury, R. Luong, L. Tian, B. Khuri-Yakub, J. Rao, R. Paulmurugan, J.K. Willmann, Ultrasound-guided delivery of microRNA loaded nanoparticles into cancer, Journal of Controlled Release 203 (2015) 99–108. https://doi.org/https://doi.org/10.1016/j.jconrel.2015.02.018.

[257] C.-Y. Lin, J.-R. Li, H.-C. Tseng, M.-F. Wu, W.-L. Lin, Enhancement of focused ultrasound with microbubbles on the treatments of anticancer nanodrug in mouse tumors,

Nanomedicine 8 (2012) 900–907. https://doi.org/https://doi.org/10.1016/j.nano.2011.10.005.

[258] Lord Rayleigh, VIII. On the pressure developed in a liquid during the collapse of a spherical cavity , The London, Edinburgh, and Dublin Philosophical Magazine and Journal of Science 34 (1917) 94–98. https://doi.org/10.1080/14786440808635681.

[259] M.S. Plesset, The Dynamics of Cavitation Bubbles, J Appl Mech 16 (2021) 277–282. https://doi.org/10.1115/1.4009975.

[260] L.D. Landau, E.M. Lifshitz, Course of theoretical physics, Elsevier, 2013.

[261] T.G. Leighton, The acoustic bubble, Academic Press, London, 1994.

[262] B. Helfield, A Review of Phospholipid Encapsulated Ultrasound Contrast Agent Microbubble Physics, Ultrasound Med Biol 45 (2019) 282–300. https://doi.org/10.1016/j.ultrasmedbio.2018.09.020.

[263] P. Marmottant, S. van der Meer, M. Emmer, M. Versluis, N. de Jong, S. Hilgenfeldt, D. Lohse, A model for large amplitude oscillations of coated bubbles accounting for buckling and rupture, J Acoust Soc Am 118 (2005) 3499–3505. https://doi.org/10.1121/1.2109427.

[264] N. de Jong, L. Hoff, T. Skotland, N. Bom, Absorption and scatter of encapsulated gas filled microspheres: Theoretical considerations and some measurements, Ultrasonics 30 (1992) 95–103. https://doi.org/10.1016/0041-624X(92)90041-J.

[265] C. Church, pulsations of gas bubbles rS ’ rr • R • R 1 (pG (Rl , t)_ poo (t), 97 (1995) 1510–1521.

[266] L. Sabat, C.K. Kundu, History of finite element method: a review, Recent Developments in Sustainable Infrastructure: Select Proceedings of ICRDSI 2019 (2020) 395–404.

[267] H. Yusefi, B. Helfield, Ultrasound Contrast Imaging: Fundamentals and Emerging Technology, Front Phys 10 (2022) 1–16. https://doi.org/10.3389/fphy.2022.791145.

[268] S.R. Wilson, P.N. Burns, Microbubble-enhanced US in Body Imaging : What Role?, Radiology 257 (2010).

[269] D.E. Goertz, An overview of the influence of therapeutic ultrasound exposures on the vasculature: High intensity ultrasound and microbubble-mediated bioeffects, International Journal of Hyperthermia 31 (2015) 134–144. https://doi.org/10.3109/02656736.2015.1009179.

[270] K. Kooiman, S. Roovers, S.A.G. Langeveld, R.T. Kleven, H. Dewitte, M.A. O'Reilly, J.M. Escoffre, A. Bouakaz, M.D. Verweij, K. Hynynen, I. Lentacker, E. Stride, C.K. Holland, Ultrasound-Responsive Cavitation Nuclei for Therapy and Drug Delivery, Ultrasound Med Biol 46 (2020) 1296–1325. https://doi.org/10.1016/j.ultrasmedbio.2020.01.002.

[271] A.R. Carson, C.F. McTiernan, L. Lavery, M. Grata, X. Leng, J. Wang, X. Chen, F.S. Villanueva, Ultrasound-targeted microbubble destruction to deliver siRNA cancer therapy, Cancer Res 72 (2012) 6191–6199. https://doi.org/10.1158/0008-5472.CAN-11-4079.

[272] H. Fujii, P. Matkar, C. Liao, D. Rudenko, P.J.H. Lee, M.A. Kuliszewski, G.J. Prud'homme, H. Leong-Poi, Optimization of ultrasound-mediated anti-angiogenic cancer gene therapy, Mol Ther Nucleic Acids 2 (2013) e94. https://doi.org/10.1038/mtna.2013.20.

[273] F. Istvanic, G.Z. Yu, F.T.H. Yu, J. Powers, X. Chen, J.J. Pacella, Sonoreperfusion therapy for microvascular obstruction: A step toward clinical translation, Ultrasound Med Biol 46 (2020) 712–720. https://doi.org/10.1016/j.ultrasmedbio.2019.11.011.

[274] K. Ferrara, R. Pollard, M. Borden, Ultrasound microbubble contrast agents: Fundamentals and application to gene and drug delivery, in: Annu Rev Biomed Eng, 2007: pp. 415–447.

[275] J. Sijl, B. Dollet, M. Overvelde, V. Garbin, T. Rozendal, N. de Jong, D. Lohse, M. Versluis, Subharmonic behavior of phospholipid-coated ultrasound contrast agent microbubbles, J Acoust Soc Am 128 (2010) 3239–3252. https://doi.org/10.1121/1.3493443.

[276] B. Helfield, X. Chen, B. Qin, F.S. Villanueva, Individual lipid encapsulated microbubble radial oscillations : Effects of fluid viscosity, J Acoust Soc Am 139 (2016) 204–214. https://doi.org/10.1121/1.4939123.

[277] N. Hosseinkhah, H. Chen, T.J. Matula, P.N. Burns, K. Hynynen, Mechanisms of microbubble–vessel interactions and induced stresses: A numerical study, J Acoust Soc Am 134 (2013) 1875–1885. https://doi.org/10.1121/1.4817843.

[278] H. Mulvana, E. Stride, J. V. Hajnal, R.J. Eckersley, Temperature dependent behavior of ultrasound contrast agents, Ultrasound Med Biol 36 (2010) 925–934. https://doi.org/10.1016/j.ultrasmedbio.2010.03.003.

[279] V. Garbin, D. Cojoc, E. Ferrari, E. Di Fabrizio, M.L.J. Overvelde, S.M. Van Der Meer, N. De Jong, D. Lohse, M. Versluis, Changes in microbubble dynamics near a boundary revealed by combined optical micromanipulation and high-speed imaging, Appl Phys Lett 90 (2007). https://doi.org/10.1063/1.2713164.

[280] T. Van Rooij, I. Beekers, K.R. Lattwein, A.F.W. Van Der Steen, N. De Jong, K. Kooiman, Vibrational Responses of Bound and Nonbound Targeted Lipid-Coated Single Microbubbles, IEEE Trans Ultrason Ferroelectr Freq Control 64 (2017) 785–797. https://doi.org/10.1109/TUFFC.2017.2679160.

[281] N.R. Shirazi, A.J. Sojahrood, H. Haghi, G. Fishbein, A. De Leon, A. Exner, M.C. Kolios, Nonlinear acoustic characterization of the shell and size engineered microbubbles and nanobubbles, IEEE International Ultrasonics Symposium, IUS 2019-Octob (2019) 1357–1360. https://doi.org/10.1109/ULTSYM.2019.8926277.

[282] M. Emmer, A. van Wamel, D.E. Goertz, N. de Jong, The onset of microbubble vibration., Ultrasound Med Biol 33 (2007) 941–949. https://doi.org/10.1016/j.ultrasmedbio.2006.11.004.

[283] D.H. Thomas, M. Butler, T. Anderson, M. Emmer, H. Vos, M. Borden, E. Stride, N. de Jong, V. Sboros, The “quasi-stable” lipid shelled microbubble in response to consecutive ultrasound pulses, Appl Phys Lett 101 (2012) 071601. https://doi.org/10.1063/1.4746258.

[284] K. Kooiman, M. Foppen-Harteveld, A.F.W. van der Steen, N. de Jong, Sonoporation of endothelial cells by vibrating targeted microbubbles, J Control Release 154 (2011) 35–41. https://doi.org/10.1016/j.jconrel.2011.04.008.

[285] Y. Hu, J.M.F. Wan, A.C.H. Yu, Membrane perforation and recovery dynamics in microbubble-mediated sonoporation, Ultrasound Med Biol 39 (2013) 2393–2405. https://doi.org/10.1016/j.ultrasmedbio.2013.08.003.

[286] A. Van Wamel, A. Bouakaz, M. Versluis, N. de Jong, Micromanipulation of endothelial cells: ultrasound-microbubble-cell interaction, Ultrasound Med Biol 30 (2004) 1255–1258.

[287] M. Postema, P. Marmottant, C.T. Lancée, S. Hilgenfeldt, N. de Jong, Ultrasound-induced microbubble coalescence., Ultrasound Med Biol 30 (2004) 1337–1344. https://doi.org/10.1016/j.ultrasmedbio.2004.08.008.

[288] C. Wang, B. Rallabandi, S. Hilgenfeldt, Frequency dependence and frequency control of microbubble streaming flows, Physics of Fluids 25 (2013). https://doi.org/10.1063/1.4790803.

[289] A. De Leon, R. Perera, C. Hernandez, M. Cooley, O. Jung, S. Jeganathan, E. Abenojar, G. Fishbein, A.J. Sojahrood, C.C. Emerson, P.L. Stewart, M.C. Kolios, A.A. Exner, Contrast enhanced ultrasound imaging by nature-inspired ultrastable echogenic nanobubbles, Nanoscale 11 (2019) 15647–15658. https://doi.org/10.1039/c9nr04828f.

[290] A. Prosperetti, A generalization of the Rayleigh–Plesset equation of bubble dynamics, Physics of Fluids 25 (1982) 409. https://doi.org/10.1063/1.863775.

[291] M. Morioka, Theory of natural frequencies of two pulsating bubbles in infinite liquid, J Nucl Sci Technol 11 (1974) 554–560. https://doi.org/10.1080/18811248.1974.9730710.

[292] H. Haghi, M.C. Kolios, The role of primary and secondary delays in the effective resonance frequency of acoustically interacting microbubbles, Ultrason Sonochem 86 (2022) 106033. https://doi.org/10.1016/j.ultsonch.2022.106033.

[293] M. Versluis, E. Stride, G. Lajoinie, B. Dollet, T. Segers, Ultrasound Contrast Agent Modeling: A Review, Ultrasound Med Biol 46 (2020) 2117–2144. https://doi.org/10.1016/j.ultrasmedbio.2020.04.014.

[294] M. Lipp, K. Lee, D. Takamoto, J. Zasadzinski, A.J. Waring, Coexistence of Buckled and Flat Monolayers, Phys Rev Lett 81 (1998) 1650–1653. https://doi.org/10.1103/PhysRevLett.81.1650.

[295] S. Paul, A. Katiyar, K. Sarkar, D. Chatterjee, W.T. Shi, F. Forsberg, Material characterization of the encapsulation of an ultrasound contrast microbubble and its subharmonic response: strain-softening interfacial elasticity model., J Acoust Soc Am 127 (2010) 3846–3857. https://doi.org/10.1121/1.3418685.

[296] P. Frinking, E. Gaud, M. Arditi, Compression-only behavior and subharmonic scattering of phospholipid-shell microbubbles, IEEE International Ultrasonics Symposium Proceedings 978 (2009) 263–266. https://doi.org/10.1109/ULTSYM.2009.5441977.

[297] N. Hosseinkhah, K. Hynynen, A three-dimensional model of an ultrasound contrast agent gas bubble and its mechanical effects on microvessels, Phys Med Biol 57 (2012) 785–808. https://doi.org/10.1088/0031-9155/57/3/785.

[298] D.B. Khismatullin, Resonance frequency of microbubbles: Effect of viscosity, J Acoust Soc Am 116 (2004) 1463. https://doi.org/10.1121/1.1778835.

[299] T. Faez, M. Emmer, M. Docter, J. Sijl, M. Versluis, N. de Jong, Characterizing the subharmonic response of phospholipid-coated microbubbles for carotid imaging., Ultrasound Med Biol 37 (2011) 958–970. https://doi.org/10.1016/j.ultrasmedbio.2011.02.017.

[300] W. Lauterborn, Resonance curves of gas bubbles in liquids, Acta Acustica United with Acustica 23 (1970) 73–81.

[301] S.M. van der Meer, B. Dollet, M.M. Voormolen, C.T. Chin, A. Bouakaz, N. de Jong, M. Versluis, D. Lohse, Microbubble spectroscopy of ultrasound contrast agents, J Acoust Soc Am 121 (2007) 648–656. https://doi.org/10.1121/1.2390673.

[302] M. Overvelde, Ultrasound Contrast Agents: Dynamics of Coated Bubbles, University of Twente, 2010. https://doi.org/10.3990/1.9789036530064.

[303] M.S. Plesset, A. Prosperetti, Bubble Dynamics and Cavitation, Annu Rev Fluid Mech 9 (1977) 145–185.

[304] H. Yusefi, B. Helfield, Ultrasound Contrast Imaging : Fundamentals and Emerging Technology, Front Phys 10 (2022) 1–16. https://doi.org/10.3389/fphy.2022.791145.

[305] A.A. Doinikov, S. Zhao, P. a Dayton, Modeling of the acoustic response from contrast agent microbubbles near a rigid wall., Ultrasonics 49 (2009) 195–201. https://doi.org/10.1016/j.ultras.2008.07.017.

[306] F. Dzaharudin, A. Ooi, R. Manasseh, Effects of boundary proximity on monodispersed microbubbles in ultrasonic fields, J Sound Vib 410 (2017) 330–343. https://doi.org/10.1016/j.jsv.2017.08.047.

[307] B.L. Helfield, B.Y.C. Leung, D.E. Goertz, The effect of boundary proximity on the response of individual ultrasound contrast agent microbubbles, Phys Med Biol 59 (2014) 1721–1745. https://doi.org/10.1088/0031-9155/59/7/1721.

[308] R. Song, C. Peng, X. Xu, J. Wang, M. Yu, Y. Hou, R. Zou, S. Yao, Controllable Formation of Monodisperse Polymer Microbubbles as Ultrasound Contrast Agents, ACS Appl Mater Interfaces 10 (2018) 14312–14320. https://doi.org/10.1021/acsami.7b17258.

[309] U. Soysal, P.N. Azevedo, F. Bureau, A. Aubry, M.S. Carvalho, A.C.S.N. Pessoa, L.G.D. La Torre, O. Couture, A. Tourin, M. Fink, P. Tabeling, Freeze-Dried Microfluidic Monodisperse Microbubbles as a New Generation of Ultrasound Contrast Agents, Ultrasound Med Biol 48 (2022) 1484–1495. https://doi.org/10.1016/j.ultrasmedbio.2022.03.011.

[310] E.C. Gelderblom, H.J. Vos, F. Mastik, T. Faez, Y. Luan, T.J. a Kokhuis, A.F.W. van der Steen, D. Lohse, N. de Jong, M. Versluis, Brandaris 128 ultra-high-speed imaging facility: 10 years of operation, updates, and enhanced features., Rev Sci Instrum 83 (2012) 103706. https://doi.org/10.1063/1.4758783.

[311] V. Garbin, M. Overvelde, B. Dollet, N. de Jong, D. Lohse, M. Versluis, Unbinding of targeted ultrasound contrast agent microbubbles by secondary acoustic forces., Phys Med Biol 56 (2011) 6161–77. https://doi.org/10.1088/0031-9155/56/19/002.

[312] M. a Ainslie, T.G. Leighton, Review of scattering and extinction cross-sections, damping factors, and resonance frequencies of a spherical gas bubble., J Acoust Soc Am 130 (2011) 3184–208. https://doi.org/10.1121/1.3628321.

[313] P. Frinking, T. Segers, Y. Luan, F. Tranquart, Three Decades of Ultrasound Contrast Agents: A Review of the Past, Present and Future Improvements, Ultrasound Med Biol 46 (2020) 892–908. https://doi.org/10.1016/j.ultrasmedbio.2019.12.008.

[314] I. Gupta, J.R. Eisenbrey, P. Machado, M. Stanczak, C.E. Wessner, C.M. Shaw, S. Gummadi, J.M. Fenkel, A. Tan, C. Miller, J. Parent, S. Schultz, M.C. Soulen, C.M. Sehgal, K. Wallace, F. Forsberg, Diagnosing portal hypertension with noninvasive subharmonic pressure estimates from a US contrast agent, Radiology 298 (2021) 104–111. https://doi.org/10.1148/RADIOL.2020202677.

[315] J.K. Dave, V.G. Halldorsdottir, J.R. Eisenbrey, J.S. Raichlen, J. Bin Liu, M.E. McDonald, K. Dickie, S. Wang, C. Leung, F. Forsberg, Noninvasive LV pressure estimation using subharmonic emissions from microbubbles, JACC Cardiovasc Imaging 5 (2012) 87–92. https://doi.org/10.1016/j.jcmg.2011.08.017.

[316] L. Hoff, P.C. Sontum, J.M. Hovem, Oscillations of polymeric microbubbles: Effect of the encapsulating shell, J Acoust Soc Am 107 (2000) 2272. https://doi.org/10.1121/1.428557.

[317] M. Versluis, D.E. Goertz, P. Palanchon, I.L. Heitman, S.M. van der Meer, B. Dollet, N. de Jong, D. Lohse, Microbubble shape oscillations excited through ultrasonic parametric driving, Phys Rev E 82 (2010) 026321. https://doi.org/10.1103/PhysRevE.82.026321.

[318] H. Yusefi, B. Helfield, The influence of inter-bubble spacing on the resonance response of ultrasound contrast agent microbubbles, Ultrason Sonochem 90 (2022) 106191. https://doi.org/10.1016/j.ultsonch.2022.106191.

[319] T. Segers, E. Gaud, M. Versluis, P. Frinking, High-precision acoustic measurements of the nonlinear dilatational elasticity of phospholipid coated monodisperse microbubbles, Soft Matter 14 (2018) 9550–9561. https://doi.org/10.1039/c8sm00918j.

[320] K. Kooiman, T. Van Rooij, B. Qin, F. Mastik, H.J. Vos, M. Versluis, A.L. Klibanov, N. De Jong, F.S. Villanueva, X. Chen, Focal areas of increased lipid concentration on the coating of microbubbles during short tone-burst ultrasound insonification, PLoS One 12 (2017) 1–21. https://doi.org/10.1371/journal.pone.0180747.

[321] V. Daeichin, T. Faez, G. Renaud, J.G. Bosch, a F.W. van der Steen, N. de Jong, Effect of self-demodulation on the subharmonic response of contrast agent microbubbles, Phys Med Biol 57 (2012) 3675–3691. https://doi.org/10.1088/0031-9155/57/12/3675.

[322] P.J. Frinking, J. Brochot, M. Arditi, Subharmonic scattering of phospholipid-shell microbubbles at low acoustic pressure amplitudes., IEEE Trans Ultrason Ferroelectr Freq Control 57 (2010) 1762–1771.

[323] A. Prosperetti, A general derivation of the subharmonic threshold for non-linear bubble oscillations., J Acoust Soc Am 133 (2013) 3719–3726. https://doi.org/10.1121/1.4802742.

[324] B.L. Helfield, E. Cherin, F.S. Foster, D.E. Goertz, Investigating the subharmonic response of individual phospholipid encapsulated microbubbles at high frequencies: a comparative study of five agents., Ultrasound Med Biol 38 (2012) 846–863. https://doi.org/10.1016/j.ultrasmedbio.2012.01.011.

[325] A. Prosperetti, Nonlinear oscillations of gas bubbles in liquids: steady-state solutions, 56 (1974) 878–885.

[326] A. Eller, Generation of Subharmonics of Order One-Half by Bubbles in a Sound Field, J Acoust Soc Am 46 (1969) 722. https://doi.org/10.1121/1.1911753.

[327] A. Katiyar, K. Sarkar, Excitation threshold for subharmonic generation from contrast microbubbles., J Acoust Soc Am 130 (2011) 3137–3147. https://doi.org/10.1121/1.3641455.

[328] G. Renaud, J.G. Bosch, A.F.W. Van Der Steen, N. De Jong, Low-amplitude non-linear volume vibrations of single microbubbles measured with an “acoustical camera,” Ultrasound Med Biol 40 (2014) 1282–1295. https://doi.org/10.1016/j.ultrasmedbio.2013.12.018.

[329] Y. Gong, M. Cabodi, T.M. Porter, Acoustic investigation of pressure-dependent resonance and shell elasticity of lipid-coated monodisperse microbubbles, Appl Phys Lett 104 (2014) 074103. https://doi.org/10.1063/1.4865805.

[330] A. Katiyar, K. Sarkar, F. Forsberg, Modeling subharmonic response from contrast microbubbles as a function of ambient static pressure., J Acoust Soc Am 129 (2011) 2325–35. https://doi.org/10.1121/1.3552884.

[331] T. Faez, I. Skachkov, M. Versluis, K. Kooiman, N. de Jong, In vivo characterization of ultrasound contrast agents: microbubble spectroscopy in a chicken embryo., Ultrasound Med Biol 38 (2012) 1608–1617. https://doi.org/10.1016/j.ultrasmedbio.2012.05.014.

[332] T. Faez, G. Renaud, M. Defontaine, S. Calle, N. de Jong, Dynamic manipulation of the subharmonic scattering of phospholipid-coated microbubbles., Phys Med Biol 56 (2011) 6459–6473. https://doi.org/10.1088/0031-9155/56/19/018.

[333] D. Singh, E. Memari, S. He, H. Yusefi, B. Helfield, Cardiac gene delivery using ultrasound: State of the field, Mol Ther Methods Clin Dev 32 (2024). https://doi.org/10.1016/j.omtm.2024.101277.

[334] B. Helfield, X. Chen, B. Qin, F.S. Villanueva, Individual lipid encapsulated microbubble radial oscillations: Effects of fluid viscosity, J Acoust Soc Am 139 (2016) 204–214. https://doi.org/10.1121/1.4939123.

[335] E. Memari, F. Hui, H. Yusefi, B. Helfield, Fluid flow influences ultrasound-assisted endothelial membrane permeabilization and calcium flux, Journal of Controlled Release 358 (2023) 333–344. https://doi.org/10.1016/j.jconrel.2023.05.004.

[336] A. Prosperetti, Measurement of the Damping of Oscillating Gas Bubbles, Journal of the Acoustical Society of America 61 (1977) 11–16. https://doi.org/10.1121/1.381273.

[337] H.J. Vos, B. Dollet, M. Versluis, N. de Jong, Nonspherical shape oscillations of coated microbubbles in contact with a wall., Ultrasound Med Biol 37 (2011) 935–948. https://doi.org/10.1016/j.ultrasmedbio.2011.02.013.

[338] B. Dollet, S.M. van der Meer, V. Garbin, N. de Jong, D. Lohse, M. Versluis, Nonspherical oscillations of ultrasound contrast agent microbubbles., Ultrasound Med Biol 34 (2008) 1465–1473. https://doi.org/10.1016/j.ultrasmedbio.2008.01.020.

[339] H. Yusefi, B. Helfield, Subharmonic resonance of phospholipid coated ultrasound contrast agent microbubbles, Ultrason Sonochem 102 (2024). https://doi.org/10.1016/j.ultsonch.2024.106753.

[340] The Structural Mechanics Module User's Guide. COMSOL Multiphysics® v. 5.6. COMSOL AB, Stockholm, Sweden. 2023, (n.d.).

[341] N. Hosseinkhah, D.E. Goertz, K. Hynynen, Microbubbles and Blood–Brain Barrier Opening: A Numerical Study on Acoustic Emissions and Wall Stress Predictions, IEEE Trans Biomed Eng 62 (2015) 1293–1304. https://doi.org/10.1109/TBME.2014.2385651.

[342] B.L. Helfield, B.Y.C. Leung, X. Huo, D.E. Goertz, Scaling of the viscoelastic shell properties of phospholipid encapsulated microbubbles with ultrasound frequency., Ultrasonics 54 (2014) 1419–1424. https://doi.org/10.1016/j.ultras.2014.03.014.

[343] J.L. Raymond, K.J. Haworth, K.B. Bader, K. Radhakrishnan, J.K. Griffin, S.-L. Huang, D.D. McPherson, C.K. Holland, Broadband attenuation measurements of phospholipid-shelled ultrasound contrast agents., Ultrasound Med Biol 40 (2014) 410–421. https://doi.org/10.1016/j.ultrasmedbio.2013.09.018.

[344] Q. Li, T.J. Matula, J. Tu, X. Guo, D. Zhang, Modeling complicated rheological behaviors in encapsulating shells of lipid-coated microbubbles accounting for nonlinear changes of both shell viscosity and elasticity., Phys Med Biol 58 (2013) 985–998. https://doi.org/10.1088/0031-9155/58/4/985.

[345] E.L. Madsen, H.J. Sathoff, J.A. Zagzebski, Ultrasonic shear wave properties of soft tissues and tissuelike materials, J Acoust Soc Am 74 (1983) 1346–1355. https://doi.org/10.1121/1.390158.

[346] L.A. Frizzell, E.L. Carstensen, J.F. Dyro, Shear properties of mammalian tissues at low megahertz frequencies, J Acoust Soc Am 60 (1976) 1409–1411. https://doi.org/10.1121/1.381236.

[347] H. Chen, A.A. Brayman, T.J. Matula, Characteristic microvessel relaxation timescales associated with ultrasound-activated microbubbles, Appl Phys Lett 101 (2012). https://doi.org/10.1063/1.4761937.

[348] D.H. Bergel, The static elastic properties of the arterial wall, J Physiol 156 (1961) 445–457. https://doi.org/10.1113/jphysiol.1961.sp006686.

[349] J.L. Cracowski, M. Roustit, Human skin microcirculation, Compr Physiol 10 (2020) 1105–1154. https://doi.org/10.1002/cphy.c190008.

[350] A.C. Shore, D.D. Sandeman, J.E. Tooke, Capillary pressure, pulse pressure amplitude, and pressure waveform in healthy volunteers, American Journal of Physiology-Heart and Circulatory Physiology 268 (1995) H147–H154. https://doi.org/10.1152/ajpheart.1995.268.1.H147.

[351] V. Garbin, B. Dollet, M. Overvelde, D. Cojoc, E. Di Fabrizio, L. van Wijngaarden, A. Prosperetti, N. de Jong, D. Lohse, M. Versluis, History force on coated microbubbles propelled by ultrasound, Physics of Fluids 21 (2009) 092003. https://doi.org/10.1063/1.3227903.

[352] C. Chen, Y. Gu, J. Tu, X. Guo, D. Zhang, Microbubble oscillating in a microvessel filled with viscous fluid: A finite element modeling study, Ultrasonics 66 (2016) 54–64. https://doi.org/10.1016/j.ultras.2015.11.010.

[353] E.E. Cho, J. Drazic, M. Ganguly, B. Stefanovic, K. Hynynen, Two-photon fluorescence microscopy study of cerebrovascular dynamics in ultrasound-induced blood – brain barrier

opening, Journal of Cerebral Blood Flow Metabolism 31 (2011) 1852–1862. https://doi.org/10.1038/jcbfm.2011.59.

[354] J.J. Choi, J.A. Feshitan, B. Baseri, S. Wang, Y.S. Tung, M.A. Borden, E.E. Konofagou, Microbubble-size dependence of focused ultrasound-induced bloodBrain barrier opening in mice in vivo, IEEE Trans Biomed Eng 57 (2010) 145–154. https://doi.org/10.1109/TBME.2009.2034533.

[355] S. Wang, G. Samiotaki, O. Olumolade, J.A. Feshitan, E.E. Konofagou, Microbubble type and distribution dependence of focused ultrasound-induced blood-brain barrier opening, Ultrasound Med Biol 40 (2014) 130–137. https://doi.org/10.1016/j.ultrasmedbio.2013.09.015.